

NANOCATALYSIS

HAICHAO LIU

Beijing National Laboratory for Molecular Sciences, College of Chemistry and Molecular Engineering, Peking University, Beijing, China

JING GUAN, XINDONG MU, GUOQIANG XU, XICHENG WANG AND
XIUFANG CHEN

CAS Key Laboratory of Bio-based Materials, Qingdao Institute of Bioenergy and Bioprocess Technology, Chinese Academy of Sciences, Qingdao, China

1 INTRODUCTION

Catalysis plays a pivotal role in energy production, chemical industry, and environmental remediation. More than 60% of chemical products and 90% of chemical processes in the world are either based or substantially dependent on catalysis. These proportions will steadily increase to satisfy our ever-growing demands for sustainable processes with superior atom-economic impacts and inferior environmental impacts.

Catalysis is significant due to the unique capabilities of catalysts in accelerating chemical reactions by reducing the energy barrier (i.e., activation energy) of their transition states and in controlling reaction pathways toward selective synthesis of target products. Catalysts can be homogeneous or heterogeneous, depending on whether they exist in the same phase as the substrates or not. Because homogeneous catalysts are readily soluble and accessible to the substrates in reaction media, they possess high catalytic activity and selectivity under mild conditions. Moreover, their structures are well defined at the molecular level. These features render these molecular catalysts capable of rationally tuning their catalytic properties by modification of their ligands and metals and tuning the reaction pathways. However, homogeneous catalysts are employed in <20% of industrial processes due to the tedious and expensive separation of catalysts from the final products. Conversely, heterogeneous catalysts are extensively employed in industry due to their easy separation and recovery, as well as their high stability even exposed to harsh reaction conditions. However, heterogeneous

catalysts usually exhibit lower activity than their homogeneous counterparts mainly due to diffusion limits and the reduced number of active sites that are accessible to reactants.

To overcome these limitations, which are associated with homogeneous and heterogeneous catalysts, new catalytic systems need to combine their advantages with respect to high efficiency, selectivity, stability, and separability. Nanocatalysts are examples of this new catalytic system, which links homogeneous catalysis and heterogeneous catalysis. They are composed of nanosized particles (nanometals or nanometal oxides that are self-supported or dispersed on other surfaces) with a large exposed surface area of active components, which enhances the accessibility of the active sites to reactants and mimics homogeneous catalysts. Their insolubility in reaction solvents and reactants renders them easily separable from reaction mixtures, which enables their resemblance of heterogeneous catalysts. The activity and selectivity of nanocatalysts can be rationally tuned by changing their chemical and physical properties, such as size, shape, composition, and morphology. Therefore, nanocatalysts and nanocatalysis have received intensive attention over the past two decades, especially since the discovery of the unique activity of nanosized Au catalysts in low-temperature CO oxidation. Consequently, nanocatalyst-involved reactions have experienced exponential growth in chemical manufacturing, energy harvesting, conversion and storage, and environmental protection.

In this chapter, the properties and functions of nanocatalysts are first discussed to provide insights into the fundamental relationships among the activity, selectivity, and/or recyclability of the nanocatalysts and their structures and compositions. Then, the methods of the state-of-the-art for syntheses of metal nanoparticles (MNPs) and supported MNPs with controllable sizes, shapes, and surface structures are summarized. Finally, the recent advances of nanocatalysis in different organic transformations, new energy conversion, and environmental remediation are also presented.

2 NANOCATALYST: SIZE, SHAPE, AND SURFACE CHEMISTRY

2.1 What is Nanocatalyst

Since the end of the 1990s and with the development of nanoscience, nanocatalysis has emerged as a domain at the interface between homogeneous catalysis and heterogeneous catalysis. The main focus is the synthesis, characterization, exploration, and exploitation of well-defined nanostructured catalysts, which include nanoparticles (NPs) and nanomaterials. NPs, which are considered to be the building blocks for nanotechnology, refer to particles with at least one dimension that is <100 nm. Metallic NPs are formed by atom clusters at the nanometer scale with intermediate properties between molecules and bulk metals. This characteristic defines new chemical and physical properties that are advantageous for various applications, particularly for catalysis. The term nanomaterial refers to any solid that has a nanometer dimension. A specific definition of “nanomaterials” was created by the European Commission (EC) in 2011: “nanomaterial means a natural, incidental or manufactured material containing particles, in an unbound state or as an aggregate or as an agglomerate and where, for 50% or more of the particles in the number size distribution, one or more external dimensions is in the size range 1–100 nm.” Despite these differences in nomenclature, NPs are always implicated and “nanocatalysts” or “nanocatalysis” adequately summarizes these cases.

Because nanocatalysts are composed of small particles of a catalytically active material, typically with a diameter range of 1–100 nm, they have attracted intense interest during

recent decades. They can be applied in different areas, such as catalysis, electrocatalysis, sensors, filters, nanoscale electronics, fuel cells, cosmetics, energy, environment, engines, water purification, and optoelectronics. The first scientific goal and challenge is associated with the synthesis of these particles with maximum control over size and shape to tailor their physical and chemical properties and to optimize their performance in a specific reaction. The second challenge is to understand how the composition and atomic-scale structures of NPs produce optimal catalytic reaction performance. Recent developments in nanotechnology and material science will aid research in the characterization, rational design, and engineering of new types of multifunctional nanocatalysts for the achievement of green and sustainable chemical processes. This research provides new opportunities to understand the nature of the active sites, the metal-support interaction mechanism, and the origin of the structure–reactivity relationship by careful design and synthesis of specific size and shape catalyst particles at the nanoscale.

2.2 General Properties of Nanocatalyst

The unique physical and chemical properties of NPs that were introduced with the development of nanoscience render them very promising candidates for various applications, including catalysis. Valence electrons in bulk metals form continuous bands. When a bulk material is reduced in a certain direction to the nanometer scale, the motion of electrons in this direction is subjected to confinement. Compared with bulk metals, NPs exhibit substantially larger total exposed surface areas and various combinations of surface structures, and effects of electronic confinement within NPs may cause major changes in an electronic structure. This effect raises the possibility of tuning the catalytic process. Nanotechnology can provide an effective means for effectively and quantitatively controlling the surface structure and electronic properties of nanocatalysts without changing their composition. Adsorption and catalytic reactions can be optimized by continuously adjusting the size of catalysts at the nanometer scale.

2.2.1 Electronic Structure The description of bulk materials applies the laws of classical physics. A metal particle will present properties that are different from the properties of bulk metals due to the reduction in size (quantum effect). In very small crystals of nanometer dimensions, which are referred to as nanocrystals, assumptions about translational symmetry and infinite sizes of crystals are not valid; thus, these systems cannot be described with the same model that is employed for a bulk solid. We can imagine that the electronic structure of a nanocrystal should be intermediate between the discrete levels of an atomic system and the band structure of a bulk solid [1], as evidenced in Figure 1. The energy levels of a nanocrystal are discrete, and the density and spacing of the energy levels of a nanocrystal are significantly larger and smaller, respectively, than the corresponding levels of one atom or a small atomic cluster. Due to their discrete energy levels, these structures are also referred to as quantum dots. The concept of energy bands and band gap remains appropriate. The highest occupied atomic levels of the atomic (or ionic) species interact with each other to form the valence band (VB) of a nanocrystal. Similarly, the lowest unoccupied levels combine to form the conduction band of a nanocrystal. The energy gap between the VB and the conduction band produces a band gap of the nanocrystal. As an example, for a metallic quantum dot, its level spacing at the Fermi level is approximately proportional to $\sim E_F/N$, where N is the number of electrons in the quantum dot. Given that E_F represents a few electronvolts and N is close to 1 per atom, the band gap of a metallic quantum

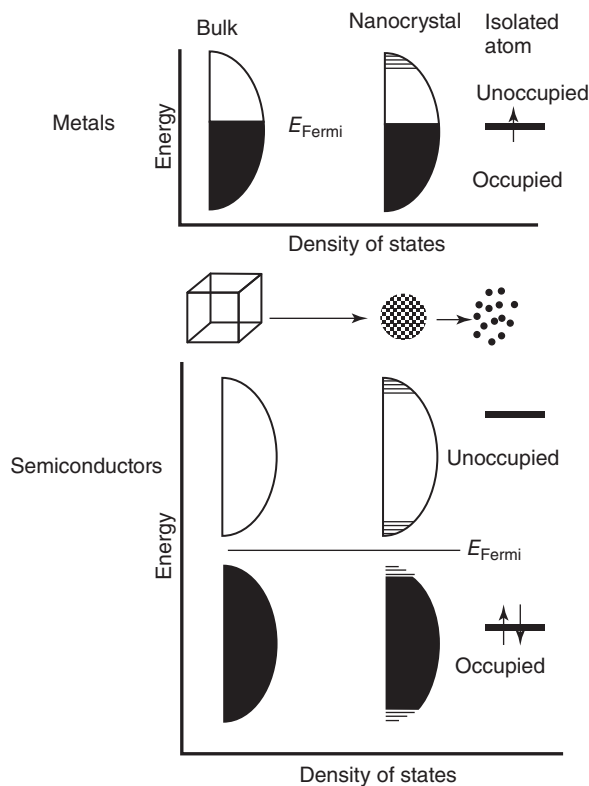


Figure 1 Density of states for metal and semiconductor nanocrystals. In each case, the density of states is discrete at the band edges. The Fermi level is in the center of a band in a metal; thus, kT may exceed the electronic energy level spacing even at room temperatures and for small sizes. Conversely, the Fermi level in semiconductors is located between two bands; thus, the relevant level spacing remains large even for small sizes. The HOMO/LUMO gap increases in semiconductor nanocrystals of smaller sizes. (Reprinted with permission from Ref. [1]. © 2002 Wiley.)

dot becomes observable only at very low temperatures. Conversely, the band gap of semiconductor quantum dots is large and its effect can be observed at room temperature. The size-tunable fluorescence emission of CdSe quantum dots in the visible region of the spectrum is, for instance, an explanatory illustration of the presence of a size-dependent band gap [2].

2.2.2 Geometric Structure The first and foremost issue of nanoclusters to be determined is their structure. In most cases, the structures of NPs cannot be described by the bulk crystallography of a material. When considering atom clusters of nanometric dimensions, they are usually densely packed; thus, they are expected to display high symmetry and consist of shells of atoms that are specific to the corresponding symmetry [3]. Considering a cluster that contains a small number of atoms, the bonding (i.e., highest compactness) should be maximized and the surface energy should be minimized (i.e., to be close to a sphere). Small clusters that contain up to tens of atoms of diverse forms (tetrahedron, hexahedron, octahedron, decahedron, dodecahedron, trigonal, trigonal prism, and hexagonal antiprism, with and without a central site) have been investigated [4]. In a cluster of a few hundred atoms,

clusters can adopt a new atomic arrangement, which may be forbidden in a bulk material. As an example, the icosahedral structure with axes of fivefold symmetry is expected to be the most stable structure for a series of magic number of atoms – 13, 55, 147, 309 – in closed-shell structures.

Experiments only provide indirect information about the geometric structure of nanoclusters. Conversely, the computational tools for analyzing a cluster enable the direct analysis of a large number of atoms. To determine the stability of the structures from an energetic point of view, the embedded atom method (EAM) was employed to determine the structures for the transition metals Cu, Pd, Ag, and Ni [5]. For sizes smaller than 2000 atoms, the icosahedron is the most stable structure, whereas for larger sizes, the cubooctahedron is the most stable structure. In a latter study that is based on the same metals, small clusters of fewer than 100 atoms with regular polyhedron geometries were employed. Tetrahedral clusters exhibited the highest stability for sizes of fewer than 18 atoms, whereas icosahedrons exhibited the highest stability for larger sizes. For gold, the EAM calculations predicted that the icosahedron transforms to a decahedron at approximately 30 atoms.

2.2.3 Melting Temperature In an extensive variety of materials that range from metals to semiconductors to insulators, a decrease in solid-to-liquid transition temperature has been observed with a reduction in nanocrystal size [6–8]. An understanding of this depression can be obtained by considering the factor that contributes to the total energy of a nanocrystal. A large surface energy is associated with a system that only contains a few hundred atoms because surface atoms tend to be coordinatively unsaturated. The key to understand this depression of melting point is the fact that the surface energy in liquid phase is always lower than the surface energy in solid phase. In dynamic fluid phase, surface atoms move to minimize surface area and unfavorable surface interactions. In the solid phase, rigid bonding geometries cause stepped surfaces with high-energy edge and corner atoms. By melting, the total surface energy is reduced. The liquid phase is stabilized over the solid phase. The smaller is the nanocrystal, the larger is the contribution to the total energy of the system by surface energy and the more significant is the depression of melting temperature. The relationship between the particle size and melting point of CdS NPs distinctly reflects the notion that the melting point decreases as the size of the particles decreases. As an example, minimum melting point depressions of 50% was observed for sufficiently small-sized nanocrystals [9].

2.2.4 Surface Energy Due to the dangling or unsatisfied bonds that are exposed to the surface, surface atoms or molecules are subjected to an inwardly directed force, and the bond distance between the surface atoms is smaller than the bond distance between interior atoms. For very small solid particles, this decrease in bond length between the surface atoms and the interior atoms becomes significant and the lattice constants of the entire solid particles show an appreciable reduction. The extra energy possessed by the surface atoms is described as surface energy, surface free energy (SFE), or surface tension. Surface energy γ is defined as the energy that is required to create a unit area of “new” surface as shown in Equation 1.

$$\gamma = \left(\frac{\partial G}{\partial A} \right)_{n,i,T,P} \quad (1)$$

where A is the surface area. The SFE of solid materials is a fundamentally important thermodynamic quantity for characterizing the surface effect by which a large number of basic

phenomena, such as crystal growth, surface faceting, and growth and stability of thin films, can be well understood. The SFE is the key to understand these properties at the nanoscale.

For NPs, the values of surface energy have been reported to exceed the values of surface energy of a bulk material [10–12]. For example, the surface energy of palladium nanoparticles (Pd NPs) in a polymer matrix is $6.0 \pm 0.9 \text{ J m}^{-2}$ [12], whereas the surface energy of Pd NPs in a bulk material is 1.808 J m^{-2} . Lu developed a model that considers the size effect of SFE for nanomaterials and discovered that SFE decreases with particle size [13]. Conversely, Medasani calculated the SFE of Ag NPs and discovered that it increases with decreasing particle size according to density functional theory (DFT) for small sizes ($r < 1 \text{ nm}$) and the empirical embedded-atom method for larger sizes ($1 \text{ nm} < r < 50 \text{ nm}$) [14]. In contrast to the results obtained by Lu and Medasani, Nanda obtained a SFE of 7.2 J m^{-2} for Ag NPs by studying the size-dependent evaporation temperature, which is related to the Kelvin effect, where the value was significantly higher than the value of the corresponding bulk material and independent of particle size [15].

A significant challenge in the fabrication and processing of nanomaterials is to overcome the immense surface energy and to prevent an increase in the sizes of nanostructures or nanomaterials, which is thermodynamically driven by a reduction in total surface energy. For a given surface with a fixed surface area, the surface energy can be reduced via the following four methods: (i) surface relaxation, the surface atoms or ions inwardly shift, which occurs more readily in liquid phase than in solid surface due to the rigid structures of solids, (ii) surface restructuring by combining surface dangling bonds into strained new chemical bonds, (iii) surface adsorption by chemical or physical adsorption of terminal chemical species onto the surface by forming chemical bonds or weak attraction forces, such as electrostatic or van der Waals forces, and (iv) composition segregation or impurity enrichment on the surface via solid-state diffusion.

2.3 Structure–Reactivity Relationship

Nanomaterials that preferentially expose the reactive crystallographic facets via size and shape control provide the possibility of finely tuning catalytically active sites. The structure–reactivity relationship for metal catalysts has been conventionally and qualitatively interpreted in terms of electronic and geometric properties, which are caused by the size effect, morphology effect, chemical composition and high surface-to-volume ratio.

2.3.1 Size Effect Nanocatalysts are characterized by their unique nanoscale properties, which originate from the highly reduced dimensions of their catalytically active domains. The effect of particle size in the context of nanocatalyst has been well understood. The lowly coordinated atoms that are located in defects in solid catalyst particles, such as terraces, edges, kinks, and vacancies, have been considered to be active sites. By reducing the domain size of catalyst particle as far as possible, the number of active sites can be maximized. The effect of particle size is frequently employed to describe the relationship between the reaction and the particle size of catalyst, especially in the size ranging from 1 to 10 nm.

The relationship between the size of NP and turnover frequency (TOF) for a given combination of reaction and NP catalysts is frequently broken into three primary groups, as proposed by Somorjai's group: positive size-sensitivity reactions, negative size-sensitivity reactions, and size-insensitive reactions. A fourth category is composed of reactions for which a local minima or maxima in activity exists at a particular NP size, as shown in Figure 2 [16, 17]. The TOF for positive size-sensitivity reactions exponentially increases

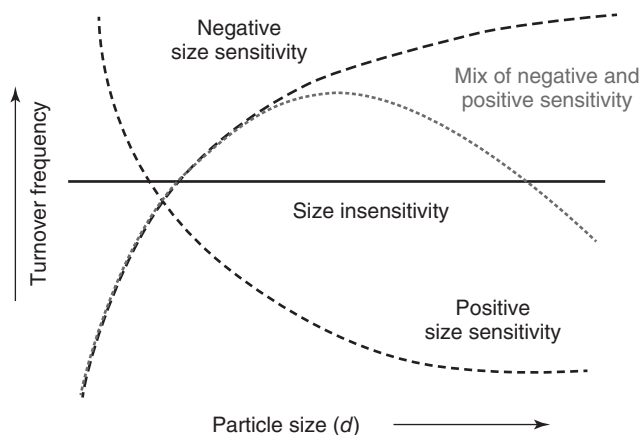


Figure 2 Major classes of size sensitivity, which describe the relationships between nanoparticle size and turnover frequency for a given combination of reaction and nanoparticle catalyst. (Reprinted with permission from Ref. [16]. © 2013 Wiley.)

as the particle size decreases. The prototypical reaction demonstrating positive size sensitivity is the activation of methane. Dissociative bond cleavage via activation of σ -bond as the rate-limiting step is a common feature in reactions with positive size sensitivity. The TOF for negative size-sensitivity reactions decreases with decreasing particle size. In this case, the formation or dissociation of a π -bond is often the rate-limiting step. The prototypical reactions for this group include the dissociation of CO and N₂ molecules, which require step-edge sites and contact with multiple atoms. These sites do not always exist on very small NPs, in which step-edges approximate at atom sites. These reactions sometimes fall into the fourth category of reactions with a local maximum in TOF versus particle size because certain particle sizes geometrically favor the formation of these types of sites. The third type of reaction is the size-insensitive reaction, for which no significant dependence of TOF on NP diameter exists. The prototypical size-insensitive reaction is hydrocarbon (HC) hydrogenation on transition metal catalysts, for which the rate-limiting step is complementary associative σ -bond formation.

For both supported and unsupported particles, considerable efforts have been dedicated to the elucidation of the influence of metal particle size on catalytic reactivity [17–19]. Gold nanoparticles (Au NPs) are a classic example of this topic. Although bulk gold has been considered to be catalytically inert, 2–5 nm particles that are dispersed on reducible oxides are highly active toward CO oxidation at low temperatures [20, 21]. This prominent size-dependent effect has been interpreted based on the variations in the geometric and/or electronic properties of active gold atoms at smaller particle sizes. The Somorjai Group demonstrated an exponential increase in TOF in CO oxidation on Rh NPs as the size of NP decreased from 7 to 2 nm [22]. Another prime example for the effect of particle size is displayed in the Fischer–Tropsch (FT) reaction, which is catalyzed by supported cobalt. Studies by Iglesia and coworkers showed that the surface-specific activity (TOF) is independent of the size of cobalt particle in the size range of 9 to 200 nm [23]. For smaller (<10 nm) Co particles, however, a decrease in FT reaction performance has been reported. Barbier *et al.* determined that Co particles that are smaller than 6 nm were less active in TOF per accessible site compared with large particles [24].

2.3.2 Morphology Effect Because heterogeneous catalysis intrinsically involves the cleavage and formation of chemical bonds between the reactant and product at the surface of catalyst, these elementary steps can be reasonably assumed to be intimately associated with the coordination environment of surface or active atoms. This dependence can be attributed to the exposed crystal facets that are predominantly determined by the shape of catalyst particle. Control of the morphology of catalyst particle enables a selective exposure of a larger fraction of the reactive facets on which the active sites can be enriched or tuned. This desirable surface coordination of catalytically active atoms or domains substantially enhances catalytic activity, selectivity, and stability. The adsorption/activation of the reaction molecules and desorption of the products are strongly dependent on the surface atomic arrangement. This phenomenon is termed morphology-dependent nanocatalysis: a catalyst particle with an anisotropic shape can significantly mediate the reaction performance if specific crystal facets are selectively exposed. Therefore, morphology-controllable synthesis of catalyst particles at the nanometer level, especially <10 nm, offers an efficient approach to modifying the proportion of crystallographic planes and the number of atoms on the corners and edges and consequently adjusts the catalytic behavior. Surface science studies of single crystals or model catalysts have demonstrated that the catalytic activity or selectivity is substantially dependent on the crystal facet or the coordination of the surface atoms. To some extent, the conceptual morphology-dependent nanocatalysts bridge the materials gap between the real catalysts for practical applications and the model catalysts that are employed in surface science.

Currently, the concept of morphology-dependent nanocatalysis has been primarily explored for metal nanostructures. A well-known example involves iron crystals that are industrially applied for ammonia synthesis. The formation rate of ammonia on Fe crystal follows the order $(111) \gg (100) > (110)$ [17], which suggests that the production rate of ammonia can be highly promoted if the iron catalyst particle can expose more reactive (111) facets. The impact of morphology on the catalytic properties was also demonstrated for Pt NPs [25, 26]. Tetrahedral Pt particles with their (111) facets exposed were more active for the electron-transfer reaction between hexacyanoferrate and thiosulfate than cubic Pt particles with their (100) facets exposed, even when the diameters of both materials ranged from 4 to 5 nm. Enhanced chemical activity of surfaces for stepped Au (211) [27] and Au (332) [28] has been observed compared with smooth Au (111) surfaces. The roughness of the surface, that is, the presence of highly undercoordinated atoms, is important for the dissociation of O_2 . Morphology-dependent nanocatalysts on metal oxide NPs have also been observed. A few recent examples convincingly demonstrate the morphology-dependent behaviors of oxide particles with definite shapes. Rod-shaped Co_3O_4 with a higher exposure of the reactive (110) planes, for which catalytically active Co^{3+} species are abundant, showed particularly high activity toward low-temperature CO oxidation [29].

2.3.3 Composition Effect The need for promoters or multimetallic catalytic systems has emerged due to several factors, including a reduction in the price of active catalysts and an increase in their activity, selectivity, and long-term stability. As an example, bimetallic NPs with core–shells, heterostructures, or intermetallic and alloyed structures are emerging as a new class of nanocatalysts. They are expected to display not only a combination of properties that are associated with two distinct metals but also new properties due to a synergy between the two metals. Bimetallic nanocrystals usually have a composition-dependent surface structure, atomic segregation behavior, and more interesting potential applications.

In recent years, many research groups have made substantial efforts in the preparation of bimetallic nanocrystals with controllable structures. For example, Pt is the most common and generally accepted as the best electrode catalyst used in polymer electrolyte membrane fuel cells. Over previous years, numerous efforts to develop alternative catalysts to Pt have primarily focused on Pt-based bimetallic alloys, in which Pt is partially replaced by less expensive metals, such as Fe, Ru, Co, and Ni. The oxygen reduction reaction (ORR) on Pt and Pt-based alloys has been extensively investigated by experimental and computational methods [30–33]. The formation of a Pt-skin layer is accompanied by a lower Pt-depleted layer in many Pt-3d alloys. Several studies of O adsorption on Pt-skin surfaces have revealed that the binding strength on Pt-skin surfaces is weaker than the binding strength on a pure Pt(111) surface, which may facilitate the removal of adsorbed O and increase the ORR rate. Recently, Hyman *et al.* examined the Pt₃Ni(111) surface and determined that the first layer only consists of Pt and the second layer is strongly Pt depleted (48% of Pt compared with 75% of Pt in a bulk material) [34]. Stamenkovic *et al.* proposed a thermodynamic procedure for estimating the potential shift of surface alloys using periodic DFT [35]. They suggested a positive potential shift for Pt-skin surfaces of Pt₃Fe, Pt₃Co, and Pt₃Ni, indicating that the skin structure is electrochemically more stable than pure Pt surfaces. This information indicates that the adsorption and electrochemical stability properties can be significantly modified with changes in the compositions of surface structures. Among other distinct benefits, such as a decrease in the cost of a catalytically active element, the use of alloys in NP catalysis can cause the following effects: (i) decreased poisoning effects, (ii) the opening of new reaction pathways, which cause distinct selectivity, (iii) the enhancement of catalytic activity due to synergistic effects and changes in the electronic properties of nanocatalysts, and (iv) an improved thermal stability of catalytically active elements.

2.3.4 Surface-To-Volume Ratio Two key factors that control the properties of nanomaterials are their size and surface characteristics. Nanocrystals of finer sizes provide an increase in surface-to-volume ratios (A/V), which cause higher catalytic activity compared with large crystals of the same mass on surface and higher chemical reactivity. If N_t denotes the total number of atoms in a particle and N_s represents the number of atoms that reside on its surface, the higher N_s/N_t ratio is an important factor for catalytic performance of particle due to its higher A/V ratio.

Full-shell clusters are constructed by hexagonal close-packed (hcp) or cubic close-packed (ccp) atoms. This notion assumes that the particles are constructed on a center atom by adding one, two, or three dense-packed shells. The number of surface atoms per shell is $N_s = 10n^2 + 2$, where n is the number of shell. The total number N_t of atoms of the n th shell is $N_t = (10n^3 + 15n^2 + 11n + 3)/3$. When the smallest full-shell cluster consists of 13 atoms, the surface atom ratio is $12/13 = 92.3\%$. The calculated surface/volume ratio for a thickness per shell of 6 Å is shown in Figure 3 [36]. By decreasing the particle size, the number of atoms on the surface or the N_s/N_t ratio is increased, that is, in the regime of fewer than 10 layers, which corresponds to ~ 3 nm.

Certain properties of materials that are composed of nanometer-sized particles are substantially dependent on the surface area. The surface atoms are chemically more active compared with bulk atoms because they usually have fewer adjacent coordination atoms and more unsaturated sites or more dangling bonds. With the reduction in the size of materials, the surface-to-volume ratio increases and the surface effect becomes more apparent. In addition, the surface states near the gap can substantially mix with the intrinsic states; these

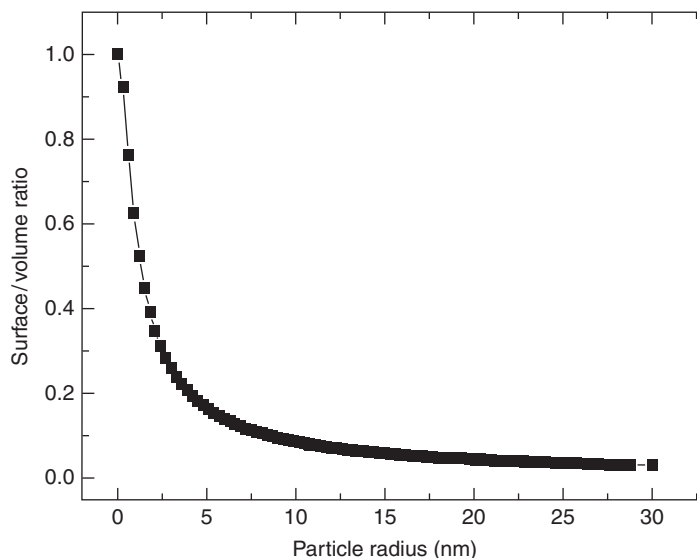


Figure 3 Variation in the calculated N_s/N_t ratio as a function of particle size. (Reprinted with permission from Ref. [36]. © 2005 American Chemical Society.)

effects may also influence the spacing of the energy levels of NPs [2, 9, 37, 38]. The chemical reactivity of a heterogeneous catalyst is proportional to the total specific surface area per unit volume; thus, the high surface areas of NPs provide the possibility of functioning as efficient catalysts.

2.4 Case Study: Gold Nanocatalysts

Nanoscale effects, which have been pervasive in heterogeneous catalysis, can be well illustrated by the remarkable catalytic activity of Au NPs. Gold was previously regarded as catalytically inert. Since the discovery of its surprisingly high catalytic activity for low-temperature CO oxidation, Au NPs have been proven to be extraordinarily effective for many reactions, ranging from the partial oxidation of HCs to water–gas shift reactions and the reduction of nitrogen oxide. We focus on recent advances in the understanding of structural sensitivity (e.g., Au particle size and shape and metal oxidation state) of Au nanocatalysts for CO oxidation and the applications of Au nanocatalysts in selective oxidation and hydrogenation reactions.

2.4.1 CO Oxidation on Oxide-Supported Au Catalysts

Structure Sensitivity of Low-Temperature CO Oxidation With the exception of H₂ oxidation and HC hydrogenation, most reactions are structure sensitive over supported Au catalysts, among which CO oxidation is the simplest and most intensively analyzed type of oxidation [39]. Au particles with a minimum diameter of approximately 5 nm exhibit unique catalytic properties, which have stimulated explorations for understanding this unexpected activity and chemical reactions that are catalyzed by Au [39]. Several explanations for the catalytic activity of these particles have been proposed [40–46], including factors

that are related to gold particles and factors related to the underlying oxide support. The size, thickness, or shape of gold particles falls in the first category. In the second category, the oxide support is considered to contribute to the catalytic activity of Au via several mechanisms: (i) charge transfer to/from the oxide support to/from the gold particle, (ii) supply of adsorption sites for reactants, in particular, oxidants, which may migrate to the Au particle surface, and (iii) formation of a reactive gold–oxide interface and the particle perimeter. Several of these effects simultaneously occur.

Studies of CO oxidation on supported Au NPs reveal that smaller particles are more active on a variety of oxide supports. The CO oxidation rate at 273 K for small gold particles (2–4 nm in diameter) was more than two orders of magnitude larger than gold particles with diameters in the range of 20–40 nm irrespective of a reducible or refractory oxide support [47]. These results strongly indicate that the size of Au particles has a major effect on their activity for CO oxidation. Although the particle size is an important factor for determining reactivity, the shape of the particles, that is, the available coordination sites, is also important. The shapes of the particles are dependent on the metal oxide support. For example, a recent study of gold particles with almost identical size distributions (~ 3 nm) was performed on different oxide supports using the colloidal deposition method [43]. The differences in the measured rates of CO oxidation for different supports were attributed to the differences in shapes of the Au particles on various oxide supports. Specifically, gold particles that were supported on Al_2O_3 , which was reported to be inactive [39, 48], are more active than the gold particles supported on the reducible oxides [48].

The thickness of gold particles is another critical structural parameter that affects its catalytic properties. As suggested by scanning tunneling microscopy (STM) and scanning tunneling spectroscopy (STS) measurements, the band gaps of one-atom-thick gold particles were significantly larger than the gap measured for two-atom-thick gold particles, which had band gaps in the range 0.2–0.6 V. Larger particles with a minimum thickness of three atoms were metallic in STS. The onset of catalytic activity of small gold particles supported on $\text{TiO}_2(110)$ correlated with a metal-to-nonmetal transition [49]. The proposal that the thickness of the gold is important was reinforced by the same group based on studies of well-ordered monolayer and bilayer films of Au on a Ti_2O_3 thin film grown on $\text{Mo}(112)$ [39]. The highest reactivity for CO oxidation at 5 Torr has been observed for a bilayer gold film by analyzing the rate of CO_2 formation obtained from different Au structures. Hutchings has employed aberration-corrected scanning transmission electron microscopy (STEM) to analyze several iron oxide-supported catalyst samples [50], including active and inactive Au species that present within supported Au/FeO_x and $\text{Au/Fe}_2\text{O}_3$ catalysts. High catalytic activity for CO oxidation is correlated with the presence of bilayer clusters with diameters of ~ 0.5 nm that only contain ~ 10 gold atoms. The activity of these bilayer clusters is consistent with the activity that was previously demonstrated with the use of model catalyst systems.

An alternative explanation of the origin of the catalytic activity of small gold particles is the presence of undercoordinated Au atoms, possibly as sites for binding or dissociation of O_2 [39, 51–53]. On the smallest nanometer-sized NPs, these atoms are located at the edges and at the corners of the particles. Evidence of the scaling of the catalytic activity of Au NPs with the number of corner atoms has been provided by Overbury *et al.* [54]. They correlated the CO oxidation activity of an Au/TiO_2 catalyst with Au particle size by combining an extended X-ray absorption fine structure (EXAFS) with *in situ* activity measurements. The results indicate that the corners and the edge sites contribute to the active site. Theoretical calculations of the structures of small Au particles supported on

TiO₂ predict a significant number of undercoordinated gold atoms [55]. As anticipated, the fraction of atoms in a particle with seven or fewer neighbors continuously increases as the particle size decreases. The theoretical calculations indicate that gold particles that serve as bilayers maximize undercoordinated gold sites for a given particle size, which support the hypothesis that the previously proposed thickness is a proxy for the presence of a large fraction of undercoordinated sites in small gold particles.

Role of Oxide Supports for CO Oxidation

ANCHORING SITES FOR GOLD PARTICLES Although metallic Au is active for CO oxidation, the oxide support serves an important role. The oxide support provides sites for anchoring gold particles to maximize surface area (and therefore, the fraction of uncoordinated Au atoms). The support may also affect the dispersion and shape of the Au particles. The presence of defects on oxide surfaces is known to provide sites for the nucleation and growth of metal particles [56–61]. As an example, the role of oxygen vacancies on TiO₂(110) in the nucleation and growth of gold particles was clearly demonstrated by STM studies [56]. Theoretical results also support this experimental observation by demonstrating that the adsorption energy of a single gold atom on an oxygen vacancy site is more stable by 0.45 eV compared with the stoichiometric surface. The nucleation and growth features of gold particles on TiO₂(110) vary depending on the density of oxygen vacancies on the terrace, which are usually influenced by sample preparation conditions. In some cases in which the density of oxygen vacancies on terraces is low, gold particles preferentially nucleate and grow on the extended defects, such as step edges of the oxide surfaces [60].

INTERFACE EFFECTS The interface sites between gold particles and the oxide support have been regarded as adsorption and reaction sites for CO oxidation. This effect was proposed by Haruta *et al.* using high-surface-area gold catalysts, based on their infrared (IR) absorption data, where two distinct CO vibrational features were observed [62]. They assigned the CO vibration peak at a higher frequency to a linearly bonded carbonyl on gold particles, whereas the vibration peak of lower frequency was assigned to CO adsorbed on the interface perimeter. The dissociation of molecular oxygen at the interface was also suggested in a study of Au supported on Fe₂O₃ [48]. On the basis of the CO–O₂ titration experiments, a significant amount of molecular oxygen can be adsorbed on the Fe₂O₃ support; this oxygen readily migrates to the interface followed by a subsequent reaction with CO. Atomic oxygen formation in these reaction conditions was detected by diffuse reflectance infrared Fourier transform spectroscopy (DRIFTS), which indicates that the dissociation of molecular oxygen occurs at the interface [63]. Liu *et al.* investigated the active oxygen species and mechanism for catalytic CO oxidation with O₂ on a highly active TiO₂-supported Au catalyst (denoted as Au/Ti(OH)^{*}₄), which was prepared by supporting an Au–phosphine complex on as-precipitated wet titanium hydroxide followed by calcination at 673 K. From the systematic oxygen isotope-exchange experiments and O₂-TPD, electron spin resonance (ESR), and Fourier transform-infrared (FT-IR), it is most likely that CO adsorbed on Au metallic particles and O[–]₂ adsorbed on oxygen vacancies at the oxide surface adjacent to the Au particles contribute to low-temperature catalytic CO oxidation [64].

Several theoretical studies have shown that O₂ can be adsorbed at the interface between the gold particle and oxide support and that the reaction barrier for CO oxidation is very low at the interface [65–69]. For example, the adsorption energy and reaction barrier were calculated for CO oxidation on Au/TiO₂(110) and nonsupported Au using DFT [69]. Three

important points were derived from these studies: (i) CO adsorption on Au is very strong (1.7 eV), irrespective of the presence of oxide for models that contain two layers of Au, (ii) O₂ can be dissociated with a low barrier (0.52 eV) at the Au/TiO₂ interface (however, O₂ dissociation is not favorable on unsupported Au ($E_a > 2$ eV)), and (iii) CO oxidation via a CO–O₂ complex has a relatively low barrier (0.1 eV) at the Au/TiO₂ interface but a higher barrier for the unsupported Au.

Positively/Negatively Charged Gold Particles The degree and direction of charge transfer to/from Au particles supported on metal oxides are controversial. Apparently, both negatively (Au^{δ−}) and positively charged gold particles (Au^{δ+}) can serve a role in CO oxidation; however, their specific roles are not clearly defined [70–75].

In addition to the stabilization of particle size and agglomeration minimization, the synergism between Au NPs and the TiO₂(110) surface seems to be an essential factor in Au-NP catalyzed CO activation. One of the main reasons for this synergism is the generation of positive Au ions on the surface of NPs. To address this issue, an MgO-supported Au(III) complex in which the oxidation states can be varied using different reducing conditions was employed, and the reaction rate was measured as a function of the surface concentration of positively charged gold (Au⁺) or metallic gold (Au⁰) [76, 77]. Each oxidation state of the catalyst was subsequently characterized by EXAFS and X-ray absorption near-edge structure (XANES). Higher concentrations of positively charged gold (that correspond to a lower partial pressure of CO in the reaction mixture) generate higher catalytic activity, which suggests that the simultaneous presence of metallic gold atoms adjacent to cationic gold is crucial in the catalytic activity of gold. These support-stabilized cationic species may serve as soft Lewis acids or participate in reactions that involve gold redox catalysis and have been proposed to be responsible for the catalytic activity of Au NPs.

In addition to the role of the oxide support for anchoring gold particles, many studies have noted that defect sites (e.g., oxygen vacancies) may play an important role in the transfer of charge to gold particles, which facilitates the formation of negatively charged gold particles and enhances the catalytic activity for CO oxidation [78–81]. This assertion contradicts proposals that positively charged Au is most active. These differences may be attributed to differences in the model versus realistic catalysts, which are prepared very differently. The study of low-temperature CO oxidation using gold octamers (Au₈) supported on MgO(001) indicated that gold octamers bound to a MgO surface that is abundant in oxygen vacancies (F centers) can catalyze CO oxidation, whereas gold particles deposited on MgO surfaces that are nearly free of oxygen vacancies are catalytically inactive [78]. This phenomenon was attributed to partial electron transfer from the F center to the gold particles, which promotes activation of adsorbed reactant molecules according to both experimental investigations and theoretical investigations.

In brief, in addition to the primary role of oxide supports for providing anchor sites for gold particles, the oxide supports – particularly their surface defects and interface sites – serve a crucial role in the enhancement of catalytic activity of gold in CO oxidation via their transfer of charge to gold particles. This role may be related to the direct activation of molecular oxygen by gold because electron-rich gold is expected to cause either increased binding of molecular oxygen to the gold surface or facile activation of molecular oxygen (i.e., O–O bond breaking or formation of peroxo or superoxo species) because more charge can be transferred to the antibonding $2\pi^*$ orbital of O₂.

2.4.2 Nanogold Catalysis in Selective Oxidative Reactions Following the mild aerobic CO oxidation methodology, Au NPs have been applied as powerful catalysts for various oxidative transformations, such as the oxidation of alcohols, aldehydes, amines, HCs, and the epoxidation of alkenes that utilizes oxygen or air as oxidants. The development of green oxidation systems is an important goal in catalysis. Due to the specific activity in selective oxidation reactions, nanogold catalysts may offer a suitable choice for constructing clean and economic-selective oxidation methods.

Benzylic and Allylic C–H Bonds Oxidation Selective oxidation of benzylic and allylic C–H bonds was initially performed by Hutchings *et al.* with Au/C or Bi–Au/C [82]. Dapurkar *et al.* tested the Au/TiO₂-catalyzed selective oxidation of primary C–H bond in benzylic compounds at 1 atm O₂ [83]. For selective oxidation reactions of different benzylic compounds, 85–100% selectivities to the corresponding ketones were obtained with 12–65% conversions. Recently, the solvent-free oxidation of primary C–H bonds in toluene and its derivatives was realized using Au–Pd alloy NPs that were immobilized on carbon or TiO₂ [84]. The major product was benzyl benzoate with >80% selectivity.

Epoxidation Reactions The selective epoxidation of olefins with air, oxygen, or H₂/O₂ using nanogold catalysts is one of the most prominent achievements in gold catalysis. Haruta *al.* presented the titania-immobilized nanogold catalyst in selective oxidation of propylene to propylene oxide with a mixture of H₂ and O₂. After optimization, a 90% selectivity of propylene oxide was attained at 1–2% propylene conversion with carbon dioxide as the major by-product [85]. With TEM characterization, it was shown that the size of Au NPs on titania is the crucial factor that affects the catalytic activity.

Alcohol Oxidation Recently, supported Au NPs have been demonstrated as extremely active catalysts for aerobic oxidation of alcohols. Employment of nanoceria-supported nanogold in selective oxidation of allylic alcohol to the corresponding α,β -unsaturated carbonyl compounds was explored [86]. This nanogold catalyst exhibited better performance than the performance of Pd–apatite, Au–Pd/TiO₂, and Au–Pd–CeO₂ catalysts. Normally, >90% conversion and selectivity were obtained with Au/CeO₂ but the selectivities with other catalysts were <60%. Au/TiO₂ was an acceptable catalyst for the synthesis of acetic acid via ethanol oxidation with high efficiency [87]. The nanogold particle has a very narrow size distribution, and the yield to acetic acid was higher than 80%. The higher ethanol concentration rendered ethyl acetate as the major product.

2.4.3 Nanogold Catalysis in Selective Hydrogenation Reactions Catalytic hydrogenation is an important reaction that is extensively employed in industry. When the particle size of gold metal was minimized to nanoscale and immobilized onto different supports with proper methodology, it serves as a very promising catalyst, especially in selective hydrogenation reactions.

An unexpected catalytic property of Au/TiO₂ was uncovered in the clean and highly regioselective isomerization of tri- and tetrasubstituted epoxides into allylic alcohols [88]. The isomerization of an epoxide into an allylic alcohol requires the synergism of a bifunctional acid/base catalyst, such as amphoteric aluminum alkoxides or amides. For the Au/TiO₂-catalyzed isomerization, the soft Lewis acidic sites are provided by ionic gold species on the surface of the catalyst, whereas the basic sites could possibly be the oxygen atoms of the support.

The alkylation of aromatics by alcohols is a typical Friedel–Crafts-type reaction catalyzed by Lewis or Bronsted acids, and homogeneous Au(III). Hardacre and coworkers [89] employed heterogenized Au NPs supported on silica (0.5–1.5% mol) to achieve good to excellent selectivity in the benzylation of substituted benzenes with benzyl alcohol.

Historically, the first known catalytic property of gold is its involvement in the hydrogenation of π -systems (alkenes, dienes, alkynes, and aromatics). This topic was reviewed by Hashmi and Hutchings in 2006 [90]. Compared with the extensively employed Pd catalysts that typically operate at ambient conditions, gold-catalyzed hydrogenations require higher temperatures (100–250 °C), which give this catalytic property low synthetic importance. In the most efficient example from previous studies, Au/SiO₂ (0.01 wt%) and less-efficient Au/Al₂O₃ or Au/boehmite catalyze the hydrogenation of pentene, 1,3-butadiene, and 2-butyne at 100 °C [91]. A significant improvement in the efficiency of 1,3-butadiene hydrogenation was reported by the group of Xu [92], who employed Au NPs supported on ZrO₂ (<0.1% Au) as a catalyst and proposed that isolated Au(III) ions on the support are the active catalytic sites.

The reduction of nitro compounds into amines, which is an important process for chemical industry, is generally achieved by hydrogenation over supported Pt and Pd catalysts, or more traditionally, by Fe or Sn/HCl. These procedures have several drawbacks, such as the requirement of stoichiometric reagents, whereas the selectivity of metal-catalyzed catalytic protocols is low if other reducible functionalities are present (e.g., halides, C–C, and C–O double bonds). In 2006, Corma and Serna reported that supported Au catalysts (Au/TiO₂ or Fe₂O₃) promote the reduction of functionalized nitro arenes into anilines in yields near 100% [93]. A significant observation is the selective reduction of nitro functionality in the presence of other reducible functionalities (C–C double bond, carbonyl, nitrile, or amide), in sharp contrast to supported Pd and Pt catalysts or homogeneous Au(I or III) and Pd(II) complexes, which provide either unselective reduction or different chemoselectivities.

2.4.4 Conclusions Au NPs can be well prepared and manipulated with controllable size, shape, and even structure in ambient conditions; they have exhibited unique catalytic properties in an extensive range of reactions. Therefore, applications of Au catalysts with superior efficiency in organic synthesis and energy conversions will increase as they become commercially available and their properties are closely uncovered.

3 SYNTHESIS OF NANOPARTICLES

MNPs exhibit unique physical and chemical properties when their dimensions are reduced to the nanoscale. MNPs, especially noble MNPs, have a characteristic high surface-to-volume ratio, and consequently, a large fraction of surface atoms that are exposed to reactant molecules, renders them a promising catalyst in chemical synthesis. Controlling the size, shape, and structure of MNPs is technologically important due to the strong correlation between these parameters and optical, electrical, and catalytic properties. Promising synthetic methods that provide suitable NPs that are responsible for target catalytic reactions are extremely important.

3.1 Wet Chemical Reduction

Various methods to synthesize MNPs are reported in the literature. These methods can be generally classified into gas-phase and liquid-phase-based methods. In the gas-phase method, bulk material is evaporated to obtain a supersaturated gas phase, which subsequently produces nuclei and becomes MNPs. In the liquid-phase method, which is also known as the wet method, precursors react to form a supersaturated solution of zero-valent metal atoms, which nucleate and further grow to MNPs.

The preparation of MNPs can generally be prepared via “bottom-up” and “top-down” synthetic routes. In “top-down” methods, bulk metals are mechanically ground to nano-size and stabilized using a suitable stabilizer [94, 95]. The problem with this method is the difficulty in achieving the narrow size distribution and control over the shape of the particles. Bimetallic NPs with core-shell structures cannot be obtained by this method. For a “bottom-up” approach, the corresponding metal precursors are reduced to atoms with reducing reagents, such as hydrides, citrate, hydrazine, and hydrogen or by electrochemical reduction or irradiation with high energetic radiation. Metal salts are usually reduced in the presence of suitable capping agents, such as thiols, amines, surfactants, or polymers, which stabilize the NPs from agglomeration. The chemical reduction of transition metal salts in the presence of stabilizing agents to generate zero-valent metal colloids in aqueous or organic media was published by Michael Faraday in 1857 [96]. The first reproducible synthesis was performed by Turkevich and coworkers, who prepared 20-nm Au particles by citrate reduction of $[\text{AuCl}_4]^-$ [97–100]. They also proposed a mechanism for the stepwise formation of NPs based on nucleation, growth, and agglomeration, as shown in Figure 4.

Stabilization of the metal particles is governed by two main factors: electrostatic repulsion among particles and steric hindrance from stabilizer molecules. Note that the majority of the methods are usually performed in solution phase (wet chemical reduction). With these methods, the core size and the surface properties of metal nanoclusters can be effectively controlled by adjusting the experimental parameters, such as the metal-to-ligand ratio, chemical structure of the protecting ligands, the nature of the reducing agent, reaction temperature and time, and pH of the solution.

The pioneering study by Brust *et al.* in 1994 [101] provides an easy and effective method to synthesize monolayer-protected metal clusters. Since 1994, the Brust–Schiffrin method has been extensively applied to various areas of nanoscience and nanotechnology. In the past decade, different types of modified Brust–Schiffrin methods have been developed to prepare metal and semiconductor nanoclusters. Generally, the following two variants have been extensively employed: the original two-phase system in water and an organic solvent

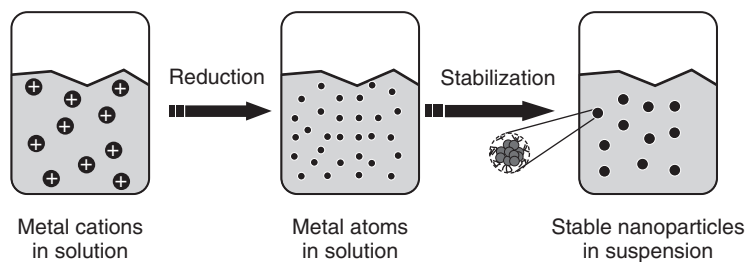


Figure 4 Formation of MNPs via reduction of metal salt precursors. (Reprinted with permission from Ref. [96]. © 2008 Wiley.)

(primarily toluene) and a modified one-phase system. In the two-phase Brust–Schiffrin synthesis method, the metal precursors are dissolved in an aqueous solution and transferred to an organic solvent by phase-transferring reagents, such as tetraoctylammonium bromide. Subsequently, organic protecting ligands and reducing reagents are added to the solution to generate metal nanoclusters. In early reports on the synthesis of Au nanoclusters, the accepted assumption was that Au(III) is reduced to Au(I) and forms $[\text{Au(I)SR}]_n$ -like polymers after the addition of alkanethiols [102]. However, Goulet and Lennox recently proposed a revised view for two-phase reactions of Brust–Schiffrin synthesis [103]. They proposed that metal precursor is shown to be a metal(I)–tetraoctylammonium halide complex ($[\text{TOA}][\text{MX}_2]$, $\text{M}=\text{Au, Ag, Cu}$) instead of the $[\text{M(I)SR}]_n$ -like polymers prior to the addition of reductant NaBH_4 .

In addition to the two-phase reaction, a one-phase synthetic method has also been extensively applied to the synthesis of various subnanometer-sized metal clusters. Au nanoclusters with different core sizes [104–106] and other metal clusters, such as Pt [107], Ag [108], and Cu [109], have been successfully synthesized with different protecting ligands and reducing reagents. For example, Lu *et al.* reported a wet chemical method for synthesizing monodispersed Ag_7 nanoclusters ($\text{Ag}_7(\text{DMSA})_4$) that were stabilized by meso-2,3-dimercaptosuccinic acid (DMSA) ligands in high yield [110]. In their designed one-phase synthetic route, silver salt (AgNO_3) that was dissolved in ethanol was cooled to $\sim 0^\circ\text{C}$ in an ice bath. With a low stirring speed (~ 60 rpm), DMSA was added to the cold Ag(I) solution. After the complete formation of $\text{Ag}_x(\text{DMSA})_y$ aggregates, NaBH_4 was slowly added to the solution with vigorous stirring. The DMSA-protected Ag_7 nanoclusters were obtained after a ~ 12 -h reaction.

Nienhaus and coworkers recently reported the synthesis of Au nanoclusters using tetrakis(hydroxymethyl)phosphonium chloride (THPC) as a mild reducing reagent instead of the strong reductant NaBH_4 [111]. Negishi *et al.* synthesized palladium nanoclusters with core sizes approximately 1.0 nm via a simple one-pot method [112]. In their experiment, palladium chloride was added to the toluene solution of *n*-alkanethiols (RSH : $\text{R}=\text{n-C}_{18}\text{H}_{37}$) with the concentration ratios $[\text{RSH}]/[\text{Pd}]$ of 2.0. Note that no additional reducing reagent is needed, and alkanethiols act as both the reducing agent and protecting ligands of the resultant Pd nanoclusters.

3.2 Stabilization of Metal Nanoparticles (MNPs)

Because “naked” NPs are kinetically unstable in solution, all preparation methods must use stabilizing agents, which adsorb at the particle surface. Three types of NP stabilization exist, that is, electrostatic stabilization, steric stabilization, and electrosteric stabilization. In *electrostatic stabilization*, anions and cations from the initial materials remain in solution and associate with the NPs. The particles are surrounded by an electrical double layer, which produces a Coulombic repulsion that prevents agglomeration. In *steric stabilization*, aggregation is prevented by the adsorption of large molecules (e.g., polymers or surfactants). The *electrosteric stabilization* combines both the steric effect and the electrostatic effect. Alternatively, the NPs can be anchored on a solid support. This approach, which is popular as a method for catalyst preparation and heterogenization, is discussed in the following section.

3.2.1 Polymer-Stabilized MNPs MNPs can be stabilized by polymers due to steric effect of polymer framework and the binding to the surfaces of MNPs by the heteroatom

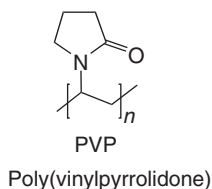


Figure 5 Major polymer families employed as metal NP supports for catalysis.

(assume the role of ligands). Polyvinyl pyrrolidone (PVP) is the most common polymer for MNP stabilization (Figure 5). Part of the PVP adsorbs on the NP surface, whereas the remaining part freely dissolves in the suspension to create a second protective shell. This method provides stability to Ag and Au hydrosols, and simple variations of the PVP–metal ratio yield structures with very different shapes and sizes [113–115]. Many other polymers have been recently employed for efficient catalysis: polyurea [116], polyacrylic acid [117], and polysiloxane [118]. Classic surfactants such as sodium dodecylsulfate (SDS) are also employed as NP stabilizers for catalysis [119].

The disadvantage of using PVP is the separation of catalytic particles from the product and the unused reactants at the end of reaction [119, 120]. To solve this problem, Mu *et al.* employed PVP-stabilized Pt, Pd, and Rh NPs that were immobilized in an ionic liquid (IL)–1-*n*-butyl-3-methylimidazolium hexafluorophosphate [121, 122]. These NPs were synthesized by reducing the corresponding metal halide in refluxing ethanol, which yields a narrow size distribution that depends on the metal–PVP ratio. They exhibited reasonable catalytic activity and stability in hydrogenation of olefins under mild conditions. The hydrogenation products were easily isolated from the IL phase by decantation. The catalyst was recycled several times without loss of activity.

A very important concept that was pioneered in the 1970s involves two different metals, such as Au and Pd, in the same NP [123]. This idea has been developed by Toshima's group, who used PVP to stabilize core–shell bimetallic Au–Pd NPs, that is, NPs in which the core is Au and the shell is Pd [124]. After coreduction, the structure is controlled by the order of reduction potentials of both ions and the coordination abilities of both atoms to PVP. The location of Au in the core and Pd on the shell was demonstrated by EXAFS; the results indicated that these heterobimetallic Au-cored Pd NPs are more active in catalysis than simple PVP-stabilized Pd NPs.

3.2.2 Dendrimer-Encapsulated MNPs Dendrimers, which were proposed by Tomalia in 1985, are tree-like polymers that have a structure in which branching is repeated in an orderly manner from the core outward [125]. Dendrimers can be synthesized with molecular weights of over 10 000 when they have a high generation number (typically more than four generations) and comprise single-molecular-weight materials via a convergent synthetic route, which is important for their use as functional materials. An interesting characteristic of dendrimers is their “shell effect” [126]. In a high-generation (more branching) dendrimer, the molecular chain density of the outer layer significantly increases; therefore, mass transfer between the inside of the dendrimer and the outside of the dendrimer is restricted. With backbones that are sufficiently rigid to retain the entire morphology, the dendrimer can retain a “dense-shell” configuration with a sufficient inner nanospace, which may be suitable for certain interior chemical conversions.

To produce metal particles in the internal space of a dendrimer, a precursor metal salt is formed and chemically reduced. Complex formation between a dendrimer and a metal salt is utilized to incorporate the metal salt into the dendrimer. The first dendrimer – poly(propyleneimine) (PPI) – was synthesized in 1978 [127]. Since then, many new classes of dendrimers have been reported. The synthesis of NPs primarily involves polyamidoamine-type (PAMAM) dendrimers due to a large number of nitrogen atoms in the molecular chain. Crooks *et al.* prepared MNPs with sizes that ranged from 1 to 4 nm by conducting a chemical reduction after introducing metal ions into a PAMAM dendrimer via a complex formation [128, 129]. To convert the precursor metal salt to NPs, reduction using a reducing agent, such as NaBH_4 , is generally performed. Because the molecular weight distribution of dendrimers is very narrow, the statistical distribution of the assembled metal precursors would be minimized compared with the case of ordinary macromolecular ligands. The most recent literature reported fine size-controlled NPs with only a $\pm 10\%$ standard deviation over a 1.5–3.0 nm region [130, 131].

3.2.3 Ligand-Stabilized MNPs The introduction of ligands as NP stabilizers is of special interest because it enables the creation of an asymmetric environment. The first example of enantioselective catalysis by NPs was reported in 1994 by Nasar *et al.* [132]. They demonstrated that Rh NPs catalyzed hydrogenations of disubstituted aromatic rings that were induced by the chiral amine R-dioctylcyclohexyl-1-ethylamine as the ligand. Pd NPs stabilized with special ligands, such as polyoxometalates [133] and cyclodextrins [134], were also active as catalysts in hydrogenation of unsaturated substrates and in the Suzuki, Heck, and Stille reactions. For example, perthiolated β -cyclodextrin-Pd NPs catalyzed the coupling of iodo and bromoarenes and iodoferrocene with phenyl boronic acid in $\text{MeCN}/\text{H}_2\text{O}$.

Thiol chemistry was extensively employed for attaching different functionalities as ligands and for synthesizing NPs [135, 136]. Recently, Ananikov *et al.* reported the synthesis of Pd NP using alkynethiol as a stabilizing ligand [137]. Note that the range of metals for which thiol NPs can be prepared is limited by the stability of the metal–sulfur bond. Schiffrin and coworkers proposed a new route to Au and Pt NPs via metal–carbon bonds [138]. The synthesis is based on the reduction of diazonium salt derivative of a long-chain alkyl benzene that acts as a phase-transfer reagent and a stabilizing ligand. Another simple mode of stabilization involves the addition of silanes, such as tert-butyldimethylsilane, to PdCl_2 or $\text{Pd}(\text{OAc})_2$. The formed NPs can catalyze the selective cross-coupling of the silane with phenyl and vinyl thioethers to yield the corresponding thiosilanes and silthianes [139].

3.2.4 MNPs in Ionic Liquids ILs, in particular imidazolium-based ILs, have proven to be suitable media for the generation and stabilization of soluble MNP. The IL forms a protective layer, which is probably composed of imidazolium aggregates that are immediately located adjacent to the NP surface, which provides both steric and electronic protection against aggregation and/or agglomeration. These stable transition MNPs, which are immobilized in the ILs, have proven to be efficient green catalysts for several reactions in multiphase conditions and novel materials for chemical sensors. For example, very fine and stable noble MNPs (Ir^0 and Ru^0 , 2.0–2.5 nm in diameter) can be synthesized in 1-*n*-butyl-3-methylimidazolium hexafluorophosphate ILs by chemical reduction [140, 141]. The colloidal system MNP/IL stabilizer is extraordinarily stable and no ligands are required; extraordinarily high turnover numbers (TONs) are achieved with this system in catalytic hydrogenation.

Although imidazolium ILs are considered to be suitable stabilizers for NPs, agglomeration causes loss of activity in some cases. Adding other materials to ILs can combine different types of stabilizing effects, which produce more stable NPs. For example, stable metal Pd NPs with diameters of 2–5 nm were obtained from the hydrogen reduction of $[\text{Pd}(\text{OAc})_2]$ in $[\text{BMI}][\text{PF}_6]$, followed by addition of phenanthroline. The phenanthroline binds to the metal surface, which is akin to the interaction that is observed with classical giant Pd clusters [142, 143], and provides extra stabilization to NPs without impairing its catalytic activity for hydrogenation reactions in multiphase conditions. Using the same approach, stable bipyridine $[\text{Rh}(\text{O})]_n$ NPs with diameters of approximately 2 nm in $[\text{BMI}][\text{PF}_6]$ were prepared and employed as arene hydrogenation catalysts [144, 145].

Transition MNPs have also been synthesized in several functionalized ILs via chemical reduction of metal precursors. Different groups, such as thiols, amines, carboxylic acids, and ethers, can be attached on the cationic and/or anionic component of IL, to provide additional stabilization of the NPs due to its coordination on the metal surface. For example, Pd NPs that are immobilized in both *N*-butylpyridinium and nitrile-functionalized ILs demonstrated suitable catalytic activity for Suzuki, Heck, and Stille coupling reactions; however, recycling and reuse are simpler in the nitrile-functionalized IL [146].

3.3 Template-Based Synthesis Methods

In previous decades, template-based methods have proved to be efficient synthetic techniques for preparing nanosized metal nanoclusters [147]. In these techniques, polymers [148], polyelectrolytes [149], proteins [150], dendrimers [151], and DNA [152] have been employed as templates. These various types of templates can provide different configurations and spaces to synthesize metal nanoclusters with the desired morphology and tunable core size. In contrast with other synthetic methods, template-based techniques provide predetermined environments for cluster formation, which is favorable for producing nanoclusters with well-controlled size and shape. After Crooks and coworkers [153] and subsequently Balogh *et al.* [154] prepared copper nanoclusters using a PAMAM starburst dendrimer as the template, template-based techniques have attracted considerable attention in the synthesis of Au, Ag, and other transition metal nanoclusters.

Noble metal nanoclusters that are synthesized with traditional wet chemical reduction methods are usually larger than 2 nm. Template-based methods have been successfully employed to synthesize Pt clusters on subnanometer scale. Yamamoto *et al.* synthesized dispersed Pt_{12} (0.9 ± 0.1 nm), Pt_{28} (1.0 ± 0.1 nm), and Pt_{60} (1.2 ± 0.1 nm) clusters using a spherical macromolecular template (phenylazomethine dendrimer) [155]. The cluster size can be precisely controlled via stepwise complexation of platinum (IV) chloride (PtCl_4) with the dendrimer.

Thus, template-based methods exhibit several crucial advantages for the preparation of fluorescent subnanometer-sized metal clusters, such as simplicity, precise cluster size control, high stability of clusters against aggregation, and potential biocompatibility. Because no stabilizing ligands exist around the nanoclusters, the clusters in the templates can provide nonblocked active surfaces when they are employed as catalysts.

3.4 Unprotected Metal Colloids

Some results for the preparation of nanoscopic metal colloids in organic media without traditional protective agents have been reported; the products can be referred to as “unprotected” metal colloids. “Unprotected” metal colloids do not indicate that the MNPs are truly

bare. They are stabilized by means of solvents or simple anions that are adsorbed on them or by both. Curtis and coworkers prepared an “unprotected” copper colloid in methanol by the reduction of copper(II) salts with hydrazine hydrate [156]. The copper colloidal particles have a mean diameter of 13.3 nm. Wang *et al.* reported an effective preparation method for stable “unprotected” Pt, Ru, and Rh metal nanoclusters with small particle sizes and narrow size distributions in organic solvents [157]. The resultant “unprotected” Pt nanocluster in ethylene glycol (EG) can be easily separated from the solvent as a precipitate that is “soluble” in many types of organic solvents. These metal nanoclusters have a valuable advantage: many polymers or organic ligands can easily modify the nanoclusters to form various protected metal nanoclusters with the same metal core.

3.5 Preparation of Supported Metal Nanoparticles

Supported NP catalysts are extensively recognized as an important class of industrial catalysts that are closely related with versatile key technologies in petrochemical industries, conversion of automobile exhausts, chemical sensors, and manufacturing of fine and specialty chemicals. There are numerous criteria for practical supported metal catalysts, including specific catalyst–support interactions, resistance to agglomeration, site isolation, excellent accessibility of substrate molecules, mechanical robustness, and low synthetic cost.

The approaches for the preparation of supported MNPs can be generally divided into chemical, physical, and physicochemical routes, including impregnation, coprecipitation, precipitation–deposition, ion exchange, microemulsions, chemical vapor deposition, sonochemistry, microwave irradiation, supercritical fluids, pulsed laser ablation, electrochemical reduction, flame spray pyrolysis, and solid grinding. The general routes and main techniques that are employed in the preparation of supported MNPs are summarized in Table 1. Because the chemical method is extensively applied in practical applications, the most common chemical approaches for the preparation of supported MNPs are discussed with an emphasis on the colloid supported on oxides, carbonaceous materials, and polymers.

3.5.1 Conventional Methods The traditional chemical synthesis methods that are employed in industrial catalysis include impregnation, coprecipitation, and deposition–precipitation. Some novel greener routes have been recently developed, including precipitation from reverse-micelle emulsions, chemical vapor deposition, and electrochemical reduction.

Wet Impregnation Wet impregnation, generally known as impregnation, is a preparation technique in which a solution of metal precursor(s) is properly mixed with the support, which includes dry impregnation (pore volume impregnation) and wet impregnation according to the volume of solution. In dry impregnation, the volume of precursor solution is equal to the pore volume of the support. In wet impregnation, the support is impregnated into a volume that exceeds the pore volume of the support. Both the solubility of metal precursors and the pore volume of the support determine the loading that is available during each time of impregnation in dry impregnation. Therefore, successive impregnation steps are needed to prepare catalysts of higher metal loading. If bimetallic or multimetallic active sites are needed, the metals can be impregnated into the support in one pot or in successive steps. After impregnation, the catalyst will be dried, calcined, and reduced to obtain the active catalysts. The structure and property of the as-prepared catalyst are

TABLE 1 Techniques that are Generally Employed for the Preparation of Supported Metal Nanoparticles

Preparation routes	Impregnation Coprecipitation Precipitation–deposition Ion exchange Microemulsions Chemical vapor deposition Sonochemistry Microwave irradiation Supercritical fluids Plasma Pulsed laser ablation Electrochemical reduction Flame spray pyrolysis Solid grinding
Reduction approaches	NaBH ₄ , H ₂ , formaldehyde, and hydrazine hydrate
NPs stabilizers	Polymers (PVP, polyacrylamide, and polyaniline), ligand, dendrimer, and ionic liquid
Stabilizers removal methods	Oxidation, high-temperature treatment, and low-temperature solvent extraction
Supports	Oxides Carbon materials Functional organic polymers

influenced by the metal precursor, support, and metal loading, as well as the condition of the impregnation, drying, calcination, and reducing processes. The majority of the industrial supported metal catalysts are produced in this manner.

Coprecipitation Coprecipitation involves the simultaneous precipitation of metal precursor and supporting material at constant pH or via an increase in pH. The supporting materials generally consist of metal oxides or silicon precursors. The particle size and the property of the as-prepared catalysts are usually affected by the precipitation reagent and the operation conditions. MNP catalysts that are prepared by coprecipitation have been employed in an extensive range of reactions, such as oxidation and hydrogenation reactions.

Deposition–Precipitation Deposition–precipitation is the precipitation of metal hydroxide to the surface of support by adjusting the pH of the metal precursor solution. After deposition, solid-supported metal hydroxide is washed, dried, calcined, and sometimes treated with H₂ at elevated temperatures to obtain the active catalyst. This method is extensively used in the preparation of supported Au NPs. Unfortunately, the waste of Au is inevitable because Au precursors cannot be completely precipitated to the support in its best activity.

These chemical methods are very simple and easy to scale up for industrial production. However, these methods frequently provide a NP of broad size distribution, and the control of particle size hinders the fulfillment of a particular application. Particle agglomeration is a common phenomenon, which reduces the availability of active sites. An excess amount of reductant (e.g., NaBH₄, H₂, formaldehyde, and hydrazine hydrate) is used to ensure the complete formation of MNP, which hinders the removal of the reagent after the reaction.

However, recent studies have indicated that some modifications to the impregnation method can provide MNPs of small size with narrow size distributions.

3.5.2 Deposition of Preformed Metal Nanoparticles onto Supports Metal nanoclusters are very promising building blocks in preparation of heterogeneous catalysts with a controllable structure, which can be synthesized in a solvent and deposited on a support without distinct aggregation.

The preparation of supported MNPs via the deposition of preformed MNPs onto supports is shown in Figure 6. As previously mentioned, the synthesis of MNPs with well-defined properties involves colloidal sols and the stabilization by surfactants, ligands, polymers, dendrimers, and ILs, which ensure that the MNPs do not aggregate. This precise control of particle size can be achieved during metal colloid preparation by tuning the conditions that affect particle size and shape, including the selection of a reducing agent (hydrazine hydrate, ascorbic acid, hydrazine hydrate, formaldehyde, NaBH_4 , H_2 , alcohol, and polyol), stabilizer (polymer or surfactant), and solvent (water or alcohol). Initial particle size is controlled by the initial concentration, reaction temperature, concentration of stabilizer, and metal particle agglomeration and sintering was prevented by the addition of a stabilizer (protective agent). The proper selection of the reagents and a suitable synthesis procedure can create reproducible protocols for producing stabilized NPs with specific structures. The stabilized reduced MNPs are typically deposited onto a solid surface to enable the MNPs to have utility in a selected reaction.

The deposition of preformed MNPs on the functional support is highly advantageous. The particle size of the NPs that are synthesized by the colloidal sols is less affected by the support than the case in which other methods such as impregnation are employed. Intensive research is currently devoted to this methodology for the findings of MNPs with well-defined size, shape, composition, and surface chemistry. Metal nanoclusters, which are dispersed across the surface of an oxide or other support, can be much more active and

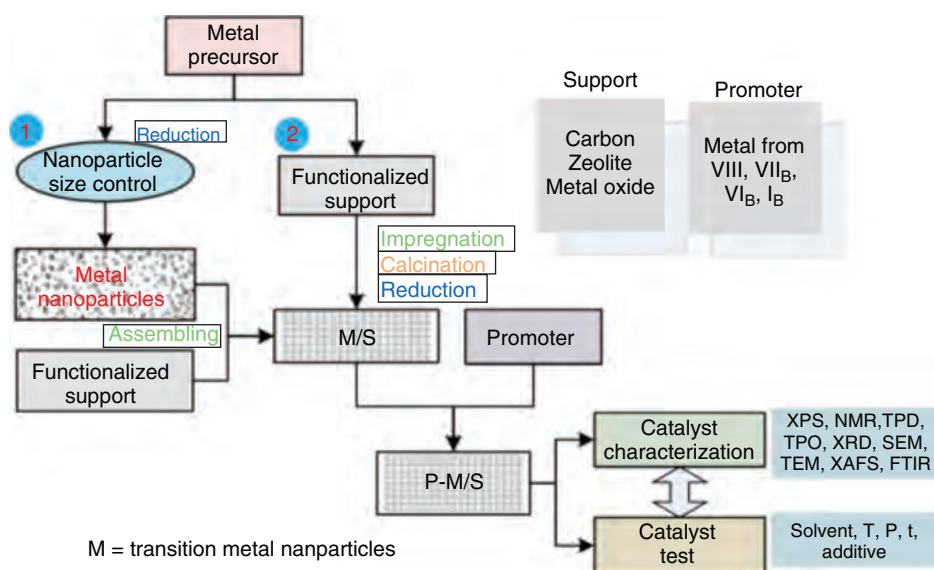


Figure 6 Fabrication of the supported catalysts.

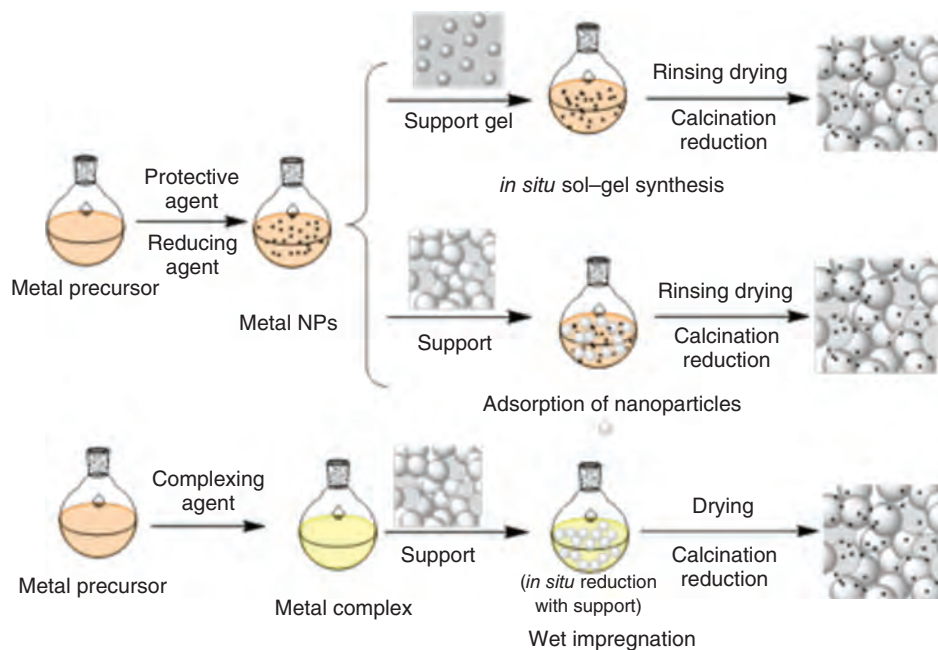


Figure 7 Catalyst preparation routes.

selective as catalysts than larger metal particles. The schematic representation of the steps in the preparation of the catalysts is shown in Figure 7.

3.5.3 Nature of Solid Supports The use of supports with defined pore sizes and characteristics for MNPs enables the dispersion and stabilization of active sites, which inhibits the growth of MNPs and the reduction of particle aggregation. The support can also generate specific adsorption sites in some reactions. Among the extensive range of solid supports that are employed for the deposition of MNPs, metal oxides, carbonaceous materials, and polymers are the three major families of extensively reported solid supports. Zeolites also served a crucial role in the preparation of a bifunctional catalyst and as a support for shape-selective catalysis.

Oxide Supports The number of reports concerning MNPs supported on metal oxides, that is, SiO_2 , Al_2O_3 , TiO_2 , ZrO_2 , CeO_2 , MgO , and ZnO , has increased. Generally, metal oxides are highly thermal stable and the feasibility of well-developed porous structures and high surface areas can fulfill the requirements for most applications. They can also be easily prepared and functionalized. For example, the introduction of another metal may change the acidity and basicity of a metal oxide. The surface structure and properties can also be altered by the preparation procedure and thermal treatment. Depending on the chemical reactivity of the support, metal oxides can be subdivided into inert supports (e.g., SiO_2) and reactive (e.g., TiO_2) metal oxides. Among the metal oxides, Al_2O_3 , TiO_2 , ZrO_2 , and CeO_2 are the most commonly employed supports. Superparamagnetic oxides (e.g., Fe_3O_4 and Co_3O_4) have recently emerged as new materials for the immobilization of MNPs with easy separation capabilities.

The catalytic reactions that were examined with these supported MNPs are hydrogenation reactions of unsaturated bonds, Heck and other C–C coupling reactions, and oxidation of CO and alcohols using molecular oxygen. The heterogenization of stabilized NPs on a solid support permits the reaction to benefit from the classic advantages of heterogeneous catalysis, that is, stability to high temperatures and easy removal from the reaction medium and the bottom-up approach of NP synthesis.

Carbonaceous Supports Carbonaceous materials offer numerous advantages as supports to ensure that the groups on the surface can be easily modified via different approaches, such as ozonolysis, doping with heteroatoms, acid or basic treatment, and thermal treatment.

Charcoal is a classic support for noble metals, such as Pd, Ru, Rh, and Ir. Activated carbons (ACs) that are suitable as support materials in catalytic processes need to be prepared and modified to obtain adequate surface area, porosity, and pore size distribution. Purification by acid treatment and elution processes is required to remove ash, extractable material, and contaminants. These supports require pretreatment and conditioning for the preparation of a suitable surface chemistry to optimize precious metal/support interactions during impregnation and dispersibility in the reaction media. Despite the conventional use of microporous carbons as supports for MNPs, recent advances in the preparation of a range of carbonaceous materials as flexible supports have been achieved. Budarin *et al.* have recently reported the preparation of an extensive range of supported MNPs [158] on a novel family of mesoporous carbonaceous materials known as Starbon [159], which was prepared from controlled carbonization (in a nitrogen atmosphere) of mesoporous starch.

Recent advances in nanofiber, nanotube, and graphene have enabled the preparation of carbon-based catalysts with MNPs dispersed at defined porosities. Their intrinsic properties include high surface areas, unique physical properties and morphologies, high electrical conductivity, and inherent size and hollow geometry, which render them extremely attractive as supports for heterogeneous catalysts.

Polymers for Metal Nanoparticles Polymers are another group of extensively employed supports for MNPs. They have been extensively employed due to their availability, enhanced stabilization properties of MNPs, and resistance to particle sintering/agglomeration. Recently, the use of novel engineered polymers, such as polyorganophosphazenes with an inorganic backbone [160], polyvinylpyridine, fibers, and dendrimers [161] as supports, has increased. Alternative supports including biopolymers and biomass-related polymers have also been recently employed for the preparation of supported MNPs [162]. Biopolymers are attractive candidates for the use as supports for catalytic applications. They offer several advantages compared with traditional supports, including low toxicity and cost, as well as high biocompatibility, availability, and abundance. Substantial research has been devoted to the preparation of different MNPs on various biopolymers, including the study of mesoporous starch, which afforded highly dispersed Pd MNPs with a narrow particle size distribution and natural porous materials (Figure 8).

3.6 Conclusions

Recent advances in the design and preparation of nanocatalysts have proven that a variety of MNPs can currently be synthesized via different preparation routes and supports with tailored size and MNP distribution to overcome the limitations of traditional synthetic methodologies. These materials will have a significant impact in many areas, including increasing

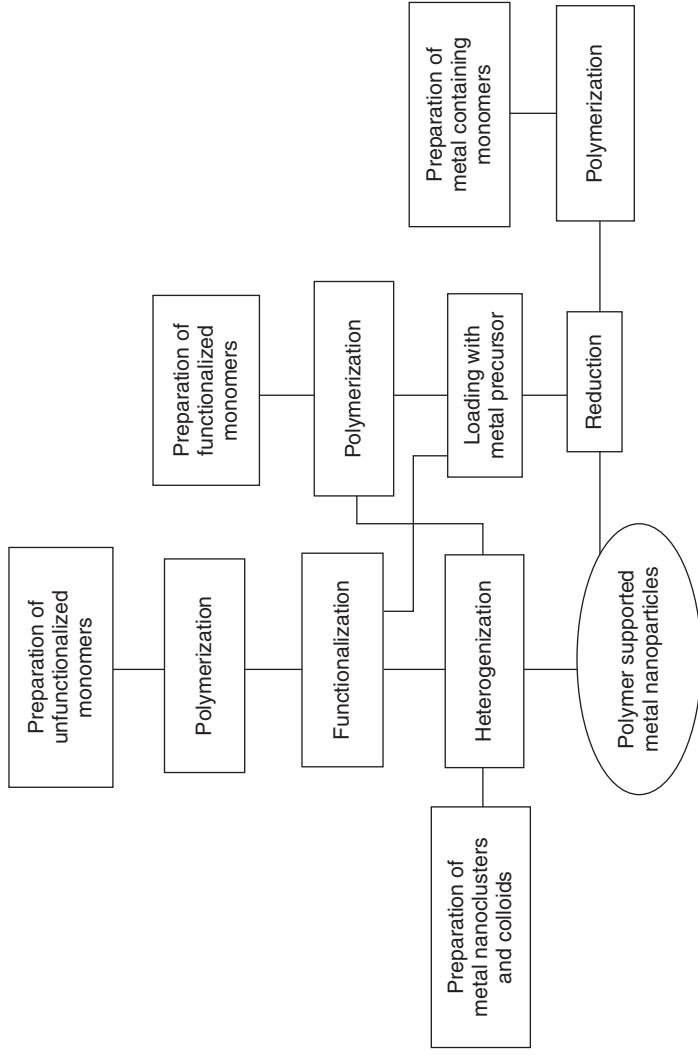


Figure 8 Routes for the preparation of metal nanoparticles supported on functional polymers.

applications in industrial catalytic processes. We must not forget that the preparation of MNPs and supported MNPs must be approached in a sustainable manner with the aim of reducing waste and the use of toxic compounds, promoting room temperature aqueous solution protocols, and improving manufacturing safety, as well as decreasing production costs. The preparation of these nanomaterials must be assessed from as many different points of view as possible (e.g., transport, waste, food chain biomagnification, and potential toxicity).

4 NANOCATALYSTS FOR ORGANIC TRANSFORMATIONS

4.1 Transformations to Form New C–C and C–Heteroatom Bonds

The formation of C–C and C–heteroatom bonds is of fundamental importance in organic chemistry and other related areas. Transition metal-catalyzed cross-coupling reactions have become one of the most powerful methods in modern pharmaceutical, agrochemical, and fine-chemical industries for the formation of new C–C and C–heteroatom bond. Many well-known cross-coupling reactions are dependent on the reactants involved, such as Suzuki, Heck, Negishi, Sonogashira, Stille, and Buchwald–Hartwig reactions. These reactions are typically homogeneously catalyzed in organic media; however, some reactions are catalyzed in water by transition metal complexes with different ligands. Because the chemistry arena has shifted toward the greener way of synthesis, nanocatalysis is a promising alternative to the homogeneous catalysis. Nanostructured catalysts are attractive candidates as heterogeneous catalysts for various organic transformations [163–165].

The potential use of nanocatalysts has attracted significant attention since the last decade. Cao and coworkers prepared Pd NPs using cucurbit[*n*]uril (CB[*n*], *n* = 4–10) as both protecting agents and supports. By changing the reducing agents and the ratio of feedstock, well-defined CB[*n*]-Pd NPs (*n* = 5–8) with various shapes have been obtained. The results of morphological analysis demonstrate that CB[6] serves a key role in guiding the formation of Pd nanostructures and is responsible for the high catalytic activity in Suzuki and Heck reactions. CB[6] serves as stabilizer for preventing the Pd nanostructures from agglomeration via electrostatic interaction between CB[6] and metal nanostructures. These relatively weak electrostatic interactions can maintain the active sites exposed on the surface of nanocatalyst, which demonstrates high catalytic activity. In mild conditions (40–80 °C), aryl bromides with both electron-withdrawing and electron-donating groups at the para-position can couple with arylboronic acids to afford the corresponding products in high yields. Even sterically hindered *o*-MeOC₆H₄Br is able to react with phenylboronic acid to afford the product in 94.5% yield. CB[6]-Pd NPs also show reasonable catalytic activity toward deactivated aryl chlorides, and a maximum yield of 92.9% biphenyl is obtained. The inductively coupled plasma (ICP) results of the filtrate indicate that the amount of Pd that leaches into the reaction system is negligible and the concentration of Pd in the filtrate is very low (0.12 ppm). The filtrates yield no coupling products after the removal of catalysts from the reaction systems, whereas high yield is obtained even after five cycles using iodobenzene and phenylboronic acid as substrates. These results suggest that the catalytic process may occur on the surface of MNPs [166].

Heterogeneous palladium nanocatalyst that is supported on metformin-grafted single-walled carbon nanotubes (SWCNTs) (SWCNT-Met/Pd(II)) has been prepared and applied to Suzuki coupling. The results showed that the new catalyst retained the reactivity characteristic of a homogeneous catalyst while simultaneously facilitating separation and reuse. The yields of the products ranged from 80% to 95% [167]. Pd NPs supported on

zirconium oxide (Pd/ZrO_2) were also demonstrated to be a very efficient catalyst in Heck, Ullmann, and Suzuki reactions of aryl halides in water. Tetra(alkyl)-ammonium hydroxide was employed as both base and PTC (phase-transfer catalyst) agent. High activity and turnover numbers ($\text{TONs} > 3 \times 10^3$) have been achieved for the Heck reaction of iodobenzene and styrene within 7 h, and the catalyst can be easily recovered and reused many times. The studies also revealed that the palladium that leaches into the solution during the reaction is negligible, and therefore, the catalysis is heterogeneous in nature [168].

To investigate whether the proposed catalyst implies a homogeneous or heterogeneous mechanism, a hot filtration test was conducted. The hot filtration test entails filtering a portion of the reaction solution to remove the catalyst once the reaction is initiated and before the reactants are consumed. After filtration, the reaction proceeds in both portions, and the conversion in both samples is determined. Typically, the conversion of the unfiltered portion that contains the suspended catalyst proceeds to completion while the filtered (catalyst free) portion continues to provide a final conversion that should provide information about a possible homogeneous pathway.

The elemental analysis of the filtered portion by inductively coupled plasma-optical emission spectrometry (ICP-OES) also provides useful information about the Pd leaching process from the support. The test can produce an inaccurate conclusion if rapid redeposition of soluble species occurs. Consequently, the distinction between heterogeneous and homogeneous catalyses cannot be solely based on the hot filtration test. If an induction period is observed, the immobilized species is not the active catalytic species due to activation of the catalyst.

Philippot and coworkers reported a comparative study of Pd complexes and Pd NPs as catalysts in C–C coupling reactions [169]. The most important feature of this study is dependent on the differences that were observed in the output of C–C coupling reactions depending on the colloidal or molecular nature of the employed catalyst. Thus, molecular systems perform typical Suzuki–Miyaura cross-coupling with dehalogenation of the substrate in different proportions. Conversely, Pd NPs catalyze either Suzuki or C–C homocoupling reactions depending on the halo-derivative. Pd NPs catalyze the quantitative dehalogenation of 4-iodotoluene. The differences observed in the chemoselectivity of these two catalytic systems support the notion that reactions with Pd NPs stabilized with the hybrid pyrazole ligands occur on the surface of the colloids.

Over the course of the past decade, cross-coupling reactions of aryl (pseudo) halides with amines or thiophenols have emerged as highly effective C(aryl)–N or C–S bond forming methods for the construction of aryl amine or diaryl sulfide derivatives [165]. The immobilization of Pd on the magnetite surface afforded Fe–Pd nanocatalyst. C–N bond formation was achieved in moderate to excellent yields, and the catalyst can be separated and recycled as many as five cycles by magnetic decantation without a significant loss in yield [170].

Tobisu and Chatani recently reported catalytic C(aryl)–N bond cleavage reactions of electronically neutral and structurally simple aryl amine derivatives via nickel-catalyzed reduction and borylation of *N*-aryl amides. Several experiments of adding mercury to the reaction were conducted to investigate the nature of the novel nickel catalyst. When the nickel-catalyzed reductive cleavage reaction was conducted with HB(pin) complexes (hydroborane reagent) in the presence of an excess of mercury, the reaction was completely suppressed, whereas the addition of an excess of mercury to the borylation reaction that involves diboron proceeded, albeit to a lesser extent. Although these data do not provide a precise mechanism of this C–N bond cleavage reaction regarding whether the catalysis is homogeneous or heterogeneous, it is likely that the reactions described in this study were

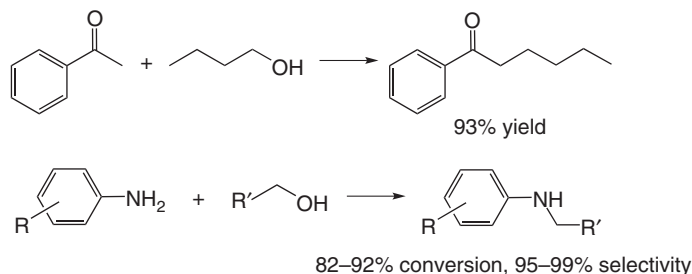
mediated by soluble or nanosized (~ 10 nm) nickel species rather than larger sized nickel aggregates [171].

Compared with the conventional organic halides, less toxic and more available alcohols have been explored as the alkylating reagents. For example, this green alternative has been employed for the direct α -alkylation of ketones, and H_2O was produced as the sole by-product. A very simple and convenient Pd/C catalytic system for the direct α -alkylation of ketones with primary alcohols in pure water has been reported (Scheme 1). TEM analyses revealed that some Pd particles aggregated after the reaction but considerable amounts of Pd particles dispersed well in the supports. In recycling experiments, the aqueous phase was analyzed by atomic absorption spectroscopy (AAS) after centrifugation. The concentration of Pd in water was detected to be <1 ppm (below the detection limit). Combined with TEM analyses, the leaching and redeposition of some Pd particles possibly occurred during the reaction [172].

A magnetically recoverable, efficient, and selective copper-based nanocatalyst has been synthesized via covalent grafting of 2-acetylthiophene on a silica-coated magnetic nanosupport followed by metallation with copper acetate. The obtained organic-inorganic hybrid nanomaterial was active in transformation of various aromatic amines to industrially important alkylated amines using alcohol as the alkylating reagent in aerobic conditions. Activated alcohol and normal aliphatic alcohol, such as 1-butanol, 2-butanol, and methanol, can be applied to alkylate various aniline derivatives with electron-donating and electron-withdrawing substituents. The heterogeneous nature of the catalyst enables easy magnetic recovery and regeneration. The catalyst can be reused 10-fold with no significant detrimental effect on the chemical yield [173].

4.2 Hydrogenation and Oxidation

4.2.1 Hydrogenation Hydrogenation of organic substrates is important for the synthesis of various fine chemicals. The application of heterogenized metal-based catalysts in selective catalytic hydrogenation processes remains challenging. Pd NPs with a mean size of 2.5 ± 0.6 nm was prepared by direct decomposition of $[\text{Pd}_2(\text{dba})_3]$ on the terpyridine-modified magnetic support. In the hydrogenation of β -myrcene, this nanocatalyst is highly selective for the formation of monohydrogenated compounds. When compared with a similar nanocatalyst that consists of Pd NPs supported on an amino-modified magnetic support or on carbon, the activity and selectivity of the nanocatalyst are significantly increased [174]. Other examples, such as the precise hydrogenative cleavage of the C–O–C bonds in cellobiose over ruthenium NPs, have been reported by Liu *et al.* [175].



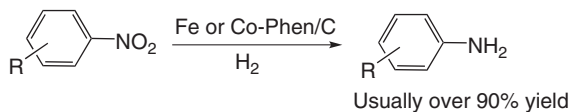
Scheme 1 The formation of C–C and C–N bonds using alcohol as the alkylating reagents.

Structurally stable and readily available WO_3 crystallite is efficient in the acceleration of the hydrolysis of cellulose to sugar intermediates and the selective cleavage of the C–C bonds in these sugars. The size of WO_3 crystallites and the type of support have an important role in this transformation. Combined with the hydrogenation step on Ru/C, controllable synthesis of EG, propylene glycol, and sorbitol from cellulose can be achieved.

Anilines are important feedstock for the synthesis of various chemicals, such as dyes, pigments, pharmaceuticals, and agrochemicals. The chemoselective catalytic reduction of nitro compounds represents the most important and prevalent process for the manufacture of functionalized anilines. Consequently, the development of selective catalysts for the reduction of nitro compounds in the presence of other reducible groups is a major challenge (Scheme 2). By immobilization and pyrolysis of the corresponding cobalt and iron–phenanthroline complexes on Vulcan XC72R carbon powder, Beller and coworkers prepared highly selective catalysts for the hydrogenation of nitroarenes to anilines. Applying these catalysts, a series of structurally diverse and functionalized nitroarenes have been reduced to anilines with unprecedented chemoselectivity tolerating halide, olefin, aldehyde, ketone, ester, amide, and nitrile functionalities. The iron oxide particles of the active catalyst are surrounded by a shell of three to five nitrogen-doped graphene layers. The majority of oxide particles have a size range between 20 and 80 nm but occur with smaller particles in the size range 2–5 nm. XPS analyses revealed that the FeN_x centers are formed during the catalyst preparation. The comparison of the characterization and catalytic results suggests that these particular FeN_x centers are formed at a pyrolysis temperature of approximately 800°C , which govern the unique catalytic activity. The size of the iron oxide particles seems to have a minor role as long as their growth does not reduce the exposed catalytically active surface [176, 177].

4.2.2 Oxidation The selective oxidation of alcohols to aldehydes and ketones represents one of the most essential transformations in organic synthesis. Conventional technology for the transformation of alcohols to aldehydes or ketones is oxidation using stoichiometric quantities of inorganic oxidants, which is highly toxic and environmentally polluting due to the production of a large amount of waste solutions that contain heavy metals.

Recently, soluble MNPs have been reported to be applicable to the aerobic oxidation of alcohols in water [178, 179]. Bases such as KOH or K_2CO_3 are frequently required for the oxidation of primary aliphatic alcohols (e.g., 1-octanol) in water. The use of bases is not green and causes problems such as corrosion and waste base treatment. Liu and coworkers reported soluble Pt NPs that exhibit excellent activities in the absence of any bases for aqueous-phase aerobic oxidation of nonactivated alcohols with high recyclability in mild conditions. Primary and secondary alcohols were oxidized to the corresponding carboxylic acids and ketones, respectively. Pt-GLY (prepared by reducing H_2PtCl_6 with glycol to stabilize the reduced Pt clusters with poly(*N*-vinyl-2-pyrrolidone)) was capable of catalyzing the aerobic oxidation of various nonactivated alcohols. Under this condition, oxidation of alicyclic alcohols gave ketones in reasonable yields of 78.4–97.1%. Oxidation of a secondary



Scheme 2 Chemoselective reduction of nitro compounds using cobalt and iron catalysts.

aliphatic alcohol, that is, 2-octanol, afforded a 94.2% of 2-octanone. Note that Pt-GLY was highly active for the oxidation of primary aliphatic alcohols – the most inactive alcohols – in the absence of any bases.

This catalyst can be readily recycled after simple extraction by diethyl ether. The yields remained constant during the five successive cycles and no Pt deposits were observed, which reflects high stability and reusability of the catalyst. This finding is consistent with the characterization results for this catalyst. The TEM and XPS characterizations reveal the formation of metallic Pt nanoclusters with a mean diameter of 1.5 nm and a narrow size distribution and no variation in the mean diameters of Pt NPs and the metallic state of Pt, respectively, after five successive runs. The extracted diethyl ether layers after each run were also analyzed by ICP; leaching of Pt was not detectable.

Detailed studies on the effect of Pt NP size, the catalytic activities of other MNPs, including noble metals Ru, Rh, Ir, and Pd, as well as Au and Ag, and the mechanistic examinations suggested the unique properties of Pt NPs [180]. The superiority of the soluble NPs may be closely related to their controllable sizes and unique nature, which are freely rotational and three dimensional compared with the traditional supported metal clusters that are restricted by support surfaces.

Spherical Pt NPs with different mean diameters (1.5–4.9 nm) and narrow size distributions exhibit different activity. The activity that was normalized by total Pt atoms in the aerobic oxidation of 1-butanol gradually increased from 4.1 to 8.3 h⁻¹ with a decrease in the particle size from 4.9 to 2.1 nm and substantially increased to 24.5 h⁻¹ for a particle size of 1.5 nm. The activity that was normalized by exposed surface Pt atoms (estimated using the mean diameters of the Pt particles and assuming that the particles are spherical), that is, TOF, was also much higher at 1.5 nm than the TOFs at other sizes. This effect has been generally ascribed to the existence of more coordinately unsaturated sites on smaller particles and the changes in their electronic properties. Au was only active for the oxidation of aliphatic alcohols in the presence of strong bases, which was presumably required for H abstraction from the alcoholic OH groups. Conversely, the activity of the Pt catalyst remained unchanged in the presence of K₂CO₃. This difference between the Au catalyst and the Pt catalyst reflects their intrinsic difference in activating the alcoholic OH groups to form alcoholate intermediates.

The oxidative reactivity of different primary and secondary aliphatic alcohols on the Pt catalyst (1.5 nm) was systematically examined. The TOFs for 1-propanol and 1-butanol were lower than the TOFs for 2-propanol and 2-butanol, whereas 1-hexanol and 1-octanol converted more rapidly than 2-hexanol and 2-octanol because these alcohols were individually employed as reactants in identical conditions. This difference in reactivity was more distinct based on the TOF ratios of the primary alcohols to the secondary alcohols, which increased from 0.88 to 2.84 with an increase in carbon number of the alcohols from three (i.e., propanols) to eight (i.e., octanols). The reactivity of the primary and secondary alcohols is dependent on their chain length and steric hindrance: the primary alcohols with longer carbon chains tend to react more preferentially over the corresponding secondary alcohols. These steric effects of the alcohols are consistent with the alcohol oxidation mechanism, which generally involves alcoholate intermediates that are derived from dissociative chemisorption of the alcohol molecules on the catalyst surfaces, and their subsequent conversion to carbonyl products in the presence of O₂.

To probe the kinetic relevance of the elementary steps, which involve the formation of alcoholate and abstraction of hydride from the alcoholates, the oxidation of 1-butanols, which are fully deuterated (1-C₄D₉OD) and only deuterated at the hydroxyl group

(1-C₄H₉OD), was examined. The TOFs and kinetic isotope effects (KIEs, denoted as $k_{\text{H}}/k_{\text{D}}$) were measured at 40 °C on the Pt catalyst (1.5 nm) with similar conversions of ~5%. These conditions were selected to maintain the reactions in the kinetic region. Undeuterated 1-butanol (1-C₄H₉OH) and 1-C₄H₉OD showed similar TOFs with a KIE of 0.94. Conversely, a significantly smaller TOF was obtained with 1-C₄D₉OD relative to 1-C₄H₉OH, and the maximum corresponding KIE was 2.50. These measured KIE values suggest that the dissociative chemisorption to form the alcoholate intermediates is quasi-equilibrated and the hydride abstraction from the alcoholates is kinetically relevant step during the oxidation of 1-butanol on Pt.

The involvement of radical intermediates was suggested by the inhibiting effect of a radical scavenger on TOFs in aerobic oxidation of 1-butanol on Pt. After addition of a slight amount of radical scavenger (i.e., 1-butanol : hydroquinone = 10 : 1), the TOF significantly decreased from 37.1 to 18.9 h⁻¹, which became negligible (3.3 h⁻¹) in the presence of an equivalent amount of the scavenger. This marked scavenger effect indicates that the kinetically relevant hydride abstraction from the alcoholates forms radical-type intermediates that are involved in the oxidation mechanism of 1-butanol.

5-Hydroxymethylfurfural (HMF) is an important biomass-based platform chemical, and its selective aerobic oxidation to 2,5-diformylfuran (DFF) remains a formidable challenge. AC-supported Ru clusters (Ru/C₂) efficiently catalyzed HMF oxidation to DFF with a high yield of ~96% at 383 K and 2.0 MPa O₂ in toluene. Ru/C exhibited activities and DFF selectivities that were superior to the activities of Ru clusters with similar sizes (about 2 nm) on oxide supports, including Al₂O₃, ZSM-5, TiO₂, ZrO₂, CeO₂, MgO, and MgAlO_x, as a consequence of their different surface acidity, basicity, and reducibility, which tend to facilitate degradation and polymerization of HMF and DFF [181, 182].

The presence of O₂ may cause over oxidation and explosion or flammability of organic solvents or alcohol reactants. The safety problem becomes critical for the practical large-scale transformation of alcohols to carbonyl compounds. Thus, the dehydrogenation of alcohols in the absence of an oxidant is a fascinating route. The dehydrogenation of alcohols in the presence of a hydrogen acceptor, such as alkenes or ketones, can proceed over supported Pd and Cu catalysts; however, this route consumes the hydrogen acceptor and produces organic by-products and is not atom economical. With respect to atom economy, the dehydrogenation of alcohols in an inert atmosphere is the most desirable route to produce carbonyl compounds and H₂.

Hensen and coworkers prepared Au nanocatalysts with particle sizes that varied between 1.7 and 15 nm by varying the support and gold-loading procedure. A strong influence of the size of gold particle on nonoxidative dehydrogenation of ethanol is noted: Au NPs of approximately 6 nm exhibit higher activity than the activity of smaller or larger particles. This optimal catalytic activity is attributed to the existence of surface steps with a suitable geometry for the removal of β-H atoms from adsorbed ethoxide. These stepped sites are expected to be present with maximum density for intermediate particle size [183].

Wang and coworkers also reported that Au NPs supported on hydrotalcite (HT), which possesses both acidity and basicity, efficiently catalyze the oxidant and acceptor-free dehydrogenation of alcohols to aldehydes or ketones and H₂. Pd/HT can also catalyze the oxidant-free dehydrogenation of alcohols but Au/HT showed higher activity and selectivity. The nature of the support and the size of Au particles served key roles in determining the catalytic behaviors in Au-catalyzed dehydrogenation reactions. The selectivity is primarily determined by acid–base property of the support, whereas the size of Au NPs controls the activity. The support may influence chemical state of the active phase via

interaction between the active phase and support. The TOF for benzyl alcohol conversion increases with a decrease in the mean particle size of Au. Particularly, TOF substantially increases when the Au particle size decreases from approximately 4 nm. The Au atoms on the coordinatively unsaturated surface are more active for the activation of C–H bond (β -H abstraction) in alcohol molecules, which is believed to be the rate-determining step [180].

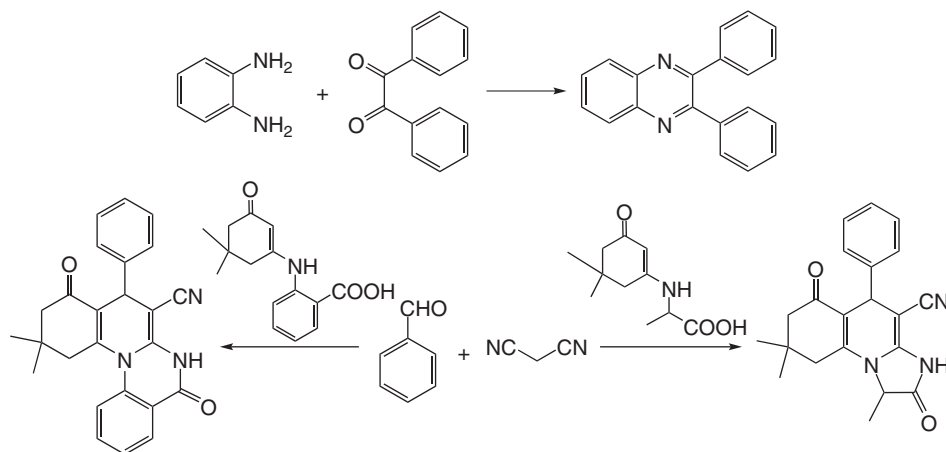
The size effect can provide deep insights into the true active sites that work for the conversion of reactants and formation of different products. These insights into the effect of Pd or Au NP size will undoubtedly be helpful for rational design of highly efficient catalysts not only for alcohol dehydrogenation but also for other reactions.

4.3 Transformations to Generate Heterocyclic Motif and Others

Heterocyclic motif is an important scaffold that has both industrial and pharmaceutical applications [184]. These motifs can be prepared using a variety of reaction conditions, such as expensive catalysts, toxic solvents, harsh reaction conditions (e.g., base and high temperatures), and multistep reaction (Scheme 3). Considering the green synthesis, nanocatalyst constitutes an important role in formation of heterocyclic ring and other important functionalization over the ring. Nanocatalyst can also be applied to the synthesis of various heterocycles, which are very difficult to prepare by conventional methods.

Quinoxaline is an important chemical entity that has interesting biological properties. The synthesis of quinoxalines was performed by oxidative coupling of 1,2-diamines and 1,2-dicarbonyl compounds using Au NPs supported on ceria (Au/CeO₂) or hydrotalcite (Au/HT) as catalysts. The use of NPs created mild reaction conditions, such as base-free reactions, using mild temperatures and air as an oxidant. The catalyst can be reused with only a little loss in activity.

The mixture of aldehyde, malononitrile, and enaminones was heated to 50 °C for 30–45 min in the presence of solid base catalysts, bulk CuO, and CuO NPs to synthesize quinoline derivatives, such as imidazo[1,2-*a*]quinoline and quinolino[1,2-*a*]quinazoline. All catalysts underwent reactions for a long time with moderate to poor yields, with the exception of CuO NPs.



Scheme 3 Examples of the synthesis of heterocycles.

The use of nanocatalyst can also be applied to the synthesis of various heterocycles, which are very difficult to prepare by conventional methods. The use of green nanocatalyst for synthesis of various heterocycles has advantages, such as short reaction time, high yield, inexpensive chemical usage, easy work-up procedure, and very specific reactions. In the majority of reactions, the spent catalyst can be easily separated from the reaction mixture and reused without noticeable change in its catalytic activity.

4.4 Conclusions

Researchers have made significant advances in the synthesis of well-defined nanostructured materials in recent years. Among these advances are novel approaches that have permitted rational design and synthesis of highly active and selective nanostructured catalysts by controlling the structure and composition of active NPs and manipulating the interaction between catalytically active NP species and their supports. The ease of isolation and separation of heterogeneous catalysts from the desired organic product and the recovery and the reuse of these NPs enhance their attractiveness as green and sustainable catalysts.

Selected examples show case principles of NP design, such as the enhancement of reactivity, selectivity, and/or recyclability of nanostructured catalysts via control of structure and composition of catalytically active NPs and/or nature of the support. Although the previous decade has brought many advances, challenges in the area of nanocatalysis, such as loss of catalytic activity during operation due to sintering, leaching of soluble species from nanocatalysts in harsh reaction conditions, loss of control over well-defined morphologies during the scale-up synthesis of nanocomposites, and limited examples of enantioselective nanocatalytic systems, need to be addressed. The future of nanocatalyst research is dependent on judicious design and development of nanocomposite catalysts that are stable and resistant to sintering and leaching but are highly active and enantioselective for the desired catalytic organic transformations, even after multiple runs. Successful applications of these multifunctional nanocatalysts, especially in tandem, domino, or cascade reactions, provide a versatile platform for the development of green and sustainable processes [185].

5 NANOCATALYSTS FOR NEW ENERGY APPLICATIONS

To demonstrate the impact of recent achievements in nanoscience in the field of energy-related processes, we present four specific examples, namely, the FT process, methane conversion, biomass conversion, and photocatalysis.

5.1 Fischer–Tropsch Synthesis (FTS)

5.1.1 Overview of FTS Fischer–Tropsch synthesis (FTS) is an exothermic catalytic process that transforms a mixed gas of CO and H₂ (syngas) into a wide spectrum of HCs. It has been one of the most important chemical processes in chemical industry. As syngas can be obtained from coal, natural gas, and biomass, the establishment of syngas conversion routes might help us develop an alternative carbon-neutral industry to replace the current petroleum-based economy.

The search for suitable catalysts for FTS reactions can be dated back to the 1920s when the FTS process was invented [186]. Varieties of transition metals have been employed for the syngas conversion, and it is confirmed that Fe-, Co-, and Ru-containing catalysts are the most efficient to catalyze the transformation of syngas to desired liquid HCs.

Usually, saturated HCs are preferably formed on Ru and Co catalysts, while more olefins are produced on Fe-based catalysts. However, because of the relatively high price of Ru, the much cheaper Fe and Co have attracted more attention from a practical point of view. Indeed, the catalysts used in commercial plants are all based on Co and/or Fe. Many reviews have been published from different perspectives [187, 188].

The reaction mechanism for FT synthesis is quite complicated, and many reviews have made efforts to describe it [189–191]. It is now generally accepted that FT synthesis proceeds through a surface-catalyzed polymerization mechanism where CH_x monomers are formed by hydrogenation of CO. Recent DFT calculations over model Ru or Co surfaces suggest that both direct CO dissociation and hydrogen-assisted CO dissociation via HCO intermediates may occur, depending on the type of surface or site (i.e., terrace or step sites) [192, 193]. Adsorbed O can be efficiently removed by H to form water, whereas adsorbed C can recombine with H to yield various CH_x intermediates ($x=0-3$). Then, chain growth through C–C coupling starts, in competition with chain termination through hydrogenation, hydrogen abstraction, or insertion of nondissociatively adsorbed CO to produce alkanes, alkenes, or alcohols, respectively [194]. The mechanism for the C–C coupling is still an open question, and many potential reactive monomers, such as adsorbed CH_2 [195], CH [196], C [197], and $\text{CH}^{\delta+}$, have been proposed. Both experimental and theoretical studies may play important roles in elucidating the coupling mechanism.

Selectivity control is one of the most important and difficult challenges for FT synthesis. As a result of the polymerization mechanism, the products of FT synthesis generally follow a statistical HC distribution, which is known as the Anderson–Schulz–Flory (ASF) distribution (Figure 9) [198]. Therefore, the distribution of product is determined by the chain-growth probability (α) value. Such a statistical distribution is nonselective for a desired range of HCs. For example, the maximum selectivities to $\text{C}_5\text{--C}_{11}$ (gasoline range) and $\text{C}_{12}\text{--C}_{20}$ (diesel range) HCs are approximately 45% and 30%, respectively.

Recent progress on the design/fabrication of nanostructured metal catalysts with altered product selectivity or increased reaction activity for the conversion of syngas is one of the most important topics in heterogeneous catalysis research. Apparently, those nanostructured materials not only provide a platform for improving the selectivity of product but also offer new insights on the FTS reaction mechanism. In this section, we will focus on the influences of catalyst factors, especially the chemical state of the

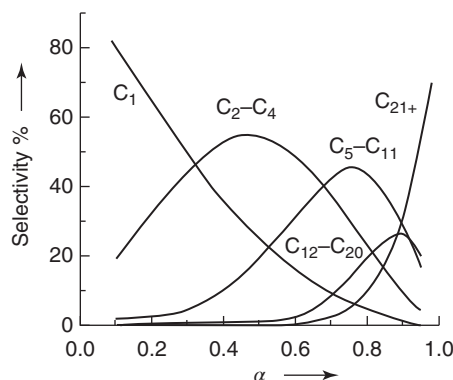


Figure 9 Product distribution in FTS as a function of the chain-growth probability.

active components and the nature of the supports and promoters on FTS activity and selectivity.

5.1.2 Key Factors of FTS Nanostructured Catalysts

Size Effect A variety of transition metals have been applied in the conversion of syngas. In general, FTS catalysts include unsupported Fe, Co, and Ru metal catalysts or those supported on oxides or other supports. The metals play crucial functions in the CO dissociation and subsequent important reaction steps such as C–C coupling. In other words, it is their intrinsic electronic structures that determine the activity toward CO activation and the product distribution.

It is widely accepted that reactions containing the decomposition or formation of C–C bonds are structure-sensitive reactions, while reactions containing decomposition or formation of only C–H bonding are structure-insensitive reactions. Therefore, the FTS reaction is recognized as a structure-sensitive reaction. de Jong and coworkers have developed an excellent Fe-based catalyst for the Fischer–Tropsch to olefins (FTO) process [199] and investigated the Fe NP size effect in this system [200]. Carbon nanofiber (CNF) was used as an inert support. The apparent TOF corresponding to initial activity of the unpromoted Fe/CNF catalysts decreased by six to eight times when the average size of iron increased from 2 to 7 nm, although the selectivity for methane and lower olefins was almost constant. In contrast to the behavior observed for the unpromoted catalysts, the product selectivity of Na, S-promoted Fe/CNF samples exhibited a clear effect of iron particle size. The lower olefin selectivity increased, while the CH₄ selectivity showed a decreasing trend when the iron size increased from 2 to 7 nm. It is suggested that the sites at the corners and edges play different roles than sites on terraces in activity and selectivity. The former is associated with size, while the latter is independent of size. These results provide a rigorous and novel elucidation of the size effect and make some important suggestions for the design of FTO catalysts.

Chemical State of Active Component Insights into the chemical state of the active sites and phases are crucial for design of highly active and selective FT catalysts. It is generally accepted that the metallic Ru⁰ and Co⁰ NPs are the active phase in FT synthesis [201]. Unlike Ru and Co catalysts, Fe catalysts usually undergo reconstruction under FT reaction conditions, and long reduction periods are often required to reach the steady states. Many studies indicate that iron carbides are the active phase, but the nature of the active and selective carbides is still unclear. Schulz and coworkers studied the construction of a Fe–Al–Cu/K₂O catalyst in H₂/CO and concluded that the FT activity was related to the formation of iron carbide (Fe₅C₂), while the metallic iron was less active [202]. Recently, De Smit *et al.* reported an *in situ* characterization of a K- and Cu-promoted Fe catalyst supported on SiO₂ using scanning transmission X-ray microscopy (STXM) combined with a nanoreactor [203]. They detected Fe₂O₃ as the sole iron phase in fresh catalyst, and this hematite phase was transformed to Fe₃O₄ and Fe₂SiO₄ (a Fe^{II} silicate) after H₂ reduction. After reaction in syngas (0.1 MPa) at 523 K, the Fe₃O₄ was further converted to Fe⁰ and Fe₂SiO₄, and iron carbides (Fe_xC_y) were also formed after the reaction. It should be noted that the Fe-based catalysts are usually sensitive to the pretreatment conditions, which may be due to the formation of different structures of iron and/or iron carbides.

Co-based materials represent an important catalyst for FTS. However, traditional Co-based catalysts usually operate at a temperature > 473 K to obtain acceptable activity and selectivity, especially for those working under liquid-phase or slurry-phase

reaction conditions, so it is desirable to develop a new catalytic system that could allow working at a relatively low reaction temperature. Ma *et al.* presented a one-step hydrogenation-reduction route for the synthesis of Pt–Co NPs, which were found to be excellent catalysts for aqueous-phase FTS at 433 K. Coupled with atomic-resolution scanning transmission electron microscopy (STEM) and theoretical calculations, the outstanding activity is rationalized by formation of Co overlayer structures on Pt NPs or Pt–Co alloy NPs. The improved energetics and kinetics from change of the TSs imposed by the lattice mismatch between the two metals can be used as the basis for rational design of bimetallic catalysts with low-temperature activities [204].

Nature of Catalyst Support The choice of a catalyst support with a proper interaction with the active metal (or metal precursor) is crucial because the balance between the reducibility and the dispersion determines the FT catalytic performance. Oxides, particularly SiO_2 , Al_2O_3 , and TiO_2 , are probably the most extensively investigated supports for Co catalysts, and the specific activity of CO hydrogenation decreases in the order of $\text{Co/TiO}_2 > \text{Co/SiO}_2 > \text{Co/Al}_2\text{O}_3 > \text{Co/C} > \text{Co/MgO}$. CNFs or carbon nanotubes (CNTs) with high external surface areas are another type of promising support for FT synthesis. The key parameters influencing the product selectivity of CNF- or CNT-supported catalysts are the size of MNPs, the location of active metals, and the pretreatment of CNFs or CNTs [205–207]. Bao and coworkers performed an interesting study to elucidate the confinement effect of CNTs on the structural and catalytic properties of Fe catalysts [205]. They developed techniques to selectively prepare Fe NPs with similar sizes (4–8 nm) but with different locations, inside and outside the CNTs (denoted as Fe-in-CNT and Fe-out-CNT, respectively). Through *in situ* XRD studies under near-reaction conditions (543 K, 0.1–0.95 MPa), the transformation of metallic Fe and Fe_3O_4 to iron carbides (Fe_xC_y , most likely Fe_5C_2 and Fe_2C) and FeO was observed. The relative ratio of integral XRD peaks of $\text{Fe}_x\text{C}_y/\text{FeO}$ suggests that the formation of Fe_xC_y was facilitated inside the CNTs. The C_{5+} selectivity was also enhanced by confining the Fe-in-CNTs. The Fe-in-CNT was also very stable, and the size of Fe particle was not significantly changed even after 200 h of reaction. In contrast, the size of Fe particle for Fe-out-CNT grew significantly during the reaction.

Zeolites have also attracted much attention for FT synthesis. In addition to the shape-selective feature of zeolites, their acidity has resulted in the development of a series of bifunctional or modified FT catalysts that can produce isoparaffins or aromatics in the gasoline range. The combination of an H-form zeolite (typically H-ZSM-5) with an Fe catalyst to form a hybrid catalyst working at temperatures higher than 573 K can provide C_6 – C_{12} aromatics with high selectivity [208]. The development of core–shell-type catalysts containing a FT-catalyst core, such as Co/SiO_2 or $\text{Co/Al}_2\text{O}_3$, and a zeolite shell further enhances the bifunctional process, producing more concentrated C_4 – C_{10} isoparaffins [209]. Further modification of the bifunctional catalysts may lead to commercialization of this novel FT process with tailored product selectivity in the near future.

Nature of the Promoter Promoters are essential for modifying the selectivity to target products, especially in the case of Co and Fe catalysts. Noble metals such as Ru and Re can enhance the reducibility and/or dispersion of the Co species and thereby increase the C_{5+} selectivity of Co catalysts [187, 210]. Transition metal oxides, particularly ZrO_2 and MnO_x , may decrease the selectivity of CH_4 and increase that of C_{5+} HCs by decreasing the hydrogenation ability and/or increasing the CO dissociation, probably via regulating the electronic state of the Co species [211]. For Fe catalysts, alkali metal ions are typically

required for decreasing the CH_4 selectivity and increasing the probability of chain growth. The alkali metal ion is expected to function as an electronic promoter to affect the electronic character of Fe and can modify the activity and selectivity by enhancing the chemisorption of CO and inhibiting that of H_2 [212]. Recent studies indicate that most promoters cannot affect the intrinsic activity (TOF) of the Fe site but are capable of enhancing the reduction and carburization of Fe species or facilitating the dispersion of active iron carbide species. To achieve the goals of decreasing the selectivities to CH_4 and CO_2 and of promoting the C_{5+} or light olefin formation, we have to combine different modifiers with different functions in one catalyst. Thus, the interactions among the different modifiers should also be considered for rational design of an efficient Fe-based catalyst. Such information as the synergistic effect between different promoters is still lacking.

5.1.3 Summary and Outlook FTS has received renewed interest because of its important position in the transformation of nonpetroleum feedstocks to environmentally benign fuels and valuable chemicals. However, very wide product distributions are generally obtained over conventional FT catalysts. Selectivity control remains one of the most important and difficult challenges in the research area of FTS. The development of efficient catalysts with controlled selectivity or tuned product distribution is a highly desirable goal.

Several important issues need to be addressed in the development and study of nanostructured FTS catalysts. (i) It is necessary to design new synthetic approaches that are simpler and can be conducted under relatively mild conditions to gain production cost advantage compared to traditional FTS catalysts. (ii) Another important aspect is to explore novel FTS nanostructured catalysts such as the bimetallic catalysts. The combination of their different characteristics could lead to enhanced catalytic activities and versatile product distributions compared to the individual components on the bimetallic catalysts or multimetallic catalysts. (iii) It is important to use combined approaches, such as theoretical modeling and *in situ* techniques, to disclose the FTS reaction mechanism and the nature of catalyst active phase. The theoretical descriptions of the FTS reaction provide information that cannot be generally obtained through practical experiments, but the gap between the modeling and experiments needs to be bridged to shed light on the FTS process under working conditions. On the basis of these considerations, we could expect that insights into the atomic-scale processes can guide the design of nanostructured catalyst for the FTS reaction to develop more energy-efficient and environmentally benign catalysis.

5.2 CH_4 Conversion

The current status of this research field is discussed with an emphasis on the activation of C–H bond and future challenges.

5.2.1 Direct Oxidative Methane Coupling The direct conversion of CH_4 is potentially more economical and environmentally friendly but is challenging because CH_4 exhibits high C–H bond strength (434 kJ mol^{-1}), negligible electron affinity, large ionization energy, and low polarizability [66]. In the pioneering work of Keller and Bhasin in the early 1980s, CH_4 was activated with the assistance of oxygen using reducible oxides [213]. This finding initiated a worldwide research surge to explore the high-temperature ($>1073 \text{ K}$) oxidative coupling of methane (OCM) to C_2 HCs. Hundreds of catalytic materials have once been synthesized and tested, principally during the 1990s, as well as in recent years [214–216].

Lunsford [217], using matrix isolation, demonstrated that on Li/MgO, one of the most studied catalysts for OMC, the main role of the catalyst was to produce methyl radicals ($\text{CH}_3\cdot$), which recombined to yield C_2H_6 . This led to a unselective reaction pathway of free radical in which ethane was further dehydrogenated to form C_2H_4 and oxidized to form carbon oxides that limited the C_2 yield. Such a pathway was generic for most oxide catalysts and their mixtures, which under reaction conditions often resulted in complex multiple phases. Given the above mechanistic information, current strategies, therefore, concentrate upon the synergetic effects among (i) strongly basic oxides, for example, MgO and La_2O_3 , which provide the catalyst with intrinsic ability to cleave the C–H bond, (ii) dopants that are incorporated into the host oxide at low concentrations, for example, Ce, Na, Li, Mn, and W, which assist in the activation of dioxygen or reoxidation of reduced metal oxide, and (iii) promoters that assist the catalyst in terms of stability and/or lifetime (e.g., Al_2O_3 or halogen anions).

Following the seminal studies of Lunsford, a wide variety of alkali, alkaline earth, rare earth, and transition metal oxides have been studied in recent decades, predominantly for their intrinsic ability to homolytically cleave the methane C–H bond [218]. Among host metal oxides, nonreducible metal oxides account for the majority of recent catalysis research. It was recently stated by Baiker *et al.* that rare earth oxides, mainly M/ La_2O_3 or Sm_2O_3 (M = Ca, Sr, Ba, etc.), appear to be the most active materials in this group of catalysts [219]. This was exemplified in a pioneering study by Deboy and Hicks using Sr-doped La_2O_3 , which resulted in a C_2 yield of almost 20% at a C_2 selectivity of 69% [220, 221].

Unfortunately, the presence of O_2 irreversibly leads to the overoxidation of methane, resulting in a large amount of thermodynamically stable end products CO_2 and H_2O . Thus, the efficiency of carbon utilization in OCM remains relatively low. Slow progress in discovering new catalysts to circumvent this problem has hindered further development, and no economically viable process has been put into practice so far.

5.2.2 Nonoxidative Methane Dehydroaromatization (MDA) Nonoxidative methane dehydroaromatization (MDA) provides a simple, straightforward, and economical pathway from methane to aromatic HCs without intermediate steps. Intensive efforts have been devoted to the development of suitable catalysts, such as Zn/HZSM-5 [222], Fe/HZSM-5 [223], and Ga/HZSM-5 [224], and encouraging progress has been made, especially in bifunctional catalysts based on Mo/zeolites, such as Mo/MCM-22 [225], Mo/HMCM-49 [226], and Mo/HZSM-5 [227–229], which catalyze the conversion of CH_4 to aromatics (benzene and naphthalene) nonoxidatively, thereby avoiding formation of CO_2 . In this process, CH_4 is activated on the metal sites to form CH_x species, which dimerize to C_2H_y . Subsequent oligomerization on the acidic sites located inside the zeolite pores yields benzene and naphthalene, as well as copious amounts of coke [230–232]. The commercial prospects for this process are further hampered by the instability of zeolites at very high reaction temperatures.

To achieve direct conversion of CH_4 efficiently, the challenges lie in cleaving the first C–H bond while suppressing further catalytic dehydrogenation and avoiding both generation of CO_2 and deposition of coke. Bao recently reported that these conditions can be met using lattice-confined single iron sites embedded in a silica matrix [233]. These sites activate CH_4 in the absence of oxidants, generating methyl radicals, which desorb from the catalyst surface and then undergo a series of gas-phase reactions to yield ethylene, benzene, and naphthalene as the only products (with ethylene dominating at short space times for a

selectivity of ~52.7% at 1293 K). A methane conversion as high as 48.1% is achieved at 1363 K, whereas the total HC selectivity exceeds 99%, representing an atom-economical transformation process of methane. The lattice-confined single iron sites deliver stable performance, with no deactivation observed during a 60-h test.

5.2.3 Partial Oxidation of Methane The partial oxidation of methane is an area of great interest and may yield commodity or bulk chemicals such as methanol, formaldehyde, or formic acid, or methanol precursors such as methyl bisulfate. Of these potential processes, the oxidation of methane to methanol is the most attractive one, at least on paper. Given its popularity and potential to revolutionize the chemical industry, a number of approaches have been investigated to partially oxidize methane, and these may broadly be classified into two main categories, partial oxidation at both high (>250 °C) and low temperatures.

A large number of studies have focused on the partial oxidation of methane at high temperature (600–800 °C) and low pressures (≈ 1 atm), typically over metal oxide catalysts [234–236]. However, it should be noted that under such reaction conditions, a number of competing consecutive reactions are prevalent, including methyl radical coupling and deeper oxidation, which reduce the yield of useful oxygenates and result in rather poor reproducibility. More crucially, significant methanol selectivity has only been observed at extremely low (<1%) levels of methane conversion.

Recent work has instead been focused on the oxidation of methane at lower reaction temperatures in an attempt to avoid the overoxidation of methanol to formaldehyde and CO_x . However, the major challenge with a low-temperature pathway is the necessity of designing an exceptionally active catalytic system. To aid this, low-temperature approaches typically require more reactive oxygen-donor species to successfully oxidize methane. One of the most efficient low-temperature approaches involves the electrophilic activation of methane over high-valent (soft) electrophiles, for example, Pt^{II} , Pd^{II} , $\text{Au}^{\text{I/III}}$, Tl^{III} , or Hg^{II} , typically performed in highly acidic reaction media (H_2SO_4 , CF_3COOH , or H_2SeO_4) [237, 238]. Another area of improvement concerns the oxidant. In this instance, a Fe- and Cu-containing MFI-type zeolite was used to selectively oxidize methane to methanol with H_2O_2 via methyl hydroperoxide [239]. Outstanding levels of methanol selectivity (>90% at 10% conversion) and higher catalytic rates were observed ($>14\,000\text{ h}^{-1}$). The key to this incredibly efficient and selective catalytic system is the formation of a unique diferric active site containing one ferryl ($\text{Fe}^{\text{IV}}=\text{O}$) and one Fe–hydroperoxy (Fe–OOH) component.

In spite of the significant breakthroughs achieved toward the low-temperature-selective oxidation of methane, it is clear that some of the greatest challenges remain, such as the low overall yields of methanol, the isolation of dilute quantities of methanol from a solvent and improvement of the catalytic rates. However, perhaps the most significant limitation is the economics of catalytic system. Indeed, the low value increase between methane and methanol makes it imperative that the catalytic system, and particularly the oxidant, be as cheap as possible.

5.3 High-Value-Added Chemicals from Biomass

The development of new technologies for producing energy and chemicals from sustainable resources has rendered biomass conversion an important research area. Biomass has been proposed as an ideal alternative to petroleum for the production of fuels and chemicals. Starch (as well as sugars), triglycerides, and lignocellulose are the general classes

of feedstocks derived from biomass used for the production of renewable biofuels and chemicals. Among them, lignocellulose biomass is the most abundant and is an inexpensive nonedible biomass that can be an excellent source of fuels and chemicals without affecting food supplies.

The development of processes to convert lignocellulosic biomass to fuels and value-added chemicals, however, remains a great challenge. The complex chemical composition of lignocellulosic biomass makes it difficult to yield target fuels and chemicals in a high yield and quality. Lignocellulose is composed of lignin (15–20%), hemicellulose (25–35%), and cellulose (40–50%). Lignin is a class of complex, cross-linked, three-dimensional biopolymers with phenyl-propane units with relatively hydrophobic and aromatic properties. Cellulose is a polymer of glucose units linked by β -glycosidic bonds, while hemicelluloses contain many different sugar monomers. Although biomass is the most abundant plant material resource, its exploitation has been limited by its composite nature and rigid structure. Most technical approaches to convert lignocellulosic material to chemicals and fuels have been focused on an effective pretreatment to liberate cellulose from the lignin composite and break down its rigid structure. Once isolated, cellulose can be hydrolyzed into glucose monomers under harsher conditions, at elevated temperature and using acid as a catalyst.

In addition to the complexity of biological sources, the inert chemical structure and the compositional ratio of carbon, hydrogen, and oxygen in lignocellulosic biomass pose additional difficulties to its chemocatalytic conversion to valuable fuels and commodity chemicals. Celluloses are highly oxygenated compounds, and their conversion into liquid HC fuels requires oxygen removal reactions (e.g., dehydration, hydrogenolysis, hydrogenation, and decarbonylation/decarboxylation), in some cases in combination with the adjustment of molecular weight via C–C coupling reactions (e.g., aldol condensation, ketonization, and oligomerization) of reactive intermediates. In this context, the development of a new family of highly active and selective catalyst systems is an essential prerequisite for the chemoselectively catalytic conversion of lignocellulosic biomass to the desired products. As such, we focus on recent advances in different catalytic processes for the conversion of lignocellulosic biomass, in particular cellulose, into potential fuels and commodity chemicals.

5.3.1 Hydrolytic Hydrogenation of Cellulose Cellulose conversion into polyols, among the various primary conversion routes explored to date [240], is evolving as a very viable option in terms of energy efficiency and atom economy. The biomass-derived polyols, such as sorbitol and glycerol, are being considered as new bioplatfrom molecules [241–244] that can be efficiently converted into H_2 , synthesis gas, alkanes, liquid fuels, and oxygenates. The direct conversion of cellulose involves hydrolysis, hydrogenation, and hydrogenolysis, and the product distribution can be tuned *via* selective cleavage of C–C and C–O bonds at specific positions using different catalysts.

Cellulose, a linear polymer of D-glucose with β -1,4-glycosidic bonds, can be readily hydrolyzed by mineral acids into glucose, which is then hydrogenated to form sorbitol and other polyols [245]. However, this process is not green and suffers from the common problems associated with the use of liquid acids, for example, corrosion and acid recovery or disposal. In attempts to solve these problems, Fukuoka and Dhepe recently showed that solid acids can replace liquid acids for conversion of cellulose into sorbitol and mannitol, but at relatively low yields [246]. In parallel with this work, Liu reported a one-step approach to convert cellulose into polyols by hydrogenation on soluble Ru clusters in ILs [247], but it encounters difficulties associated with the separation of Ru clusters

and polyol products from the ILs. These problems render the two processes unfeasible for industrial practice. For these reasons, it is apparent that the hydrolysis of cellulose by liquid acids is currently the best method, provided that the existing acid problems can be circumvented.

It is known that liquid water at elevated temperatures (above 473 K) can generate H^+ ions capable of performing acid-catalyzed reactions. The hydrolysis of cellulose catalyzed by *in situ*-generated reversible protons produced by high-temperature liquid water was first combined with hydrogenation for the production of sugar alcohols in Liu's research [248]. Ru/C was chosen as the hydrogenation catalyst for its superior glucose hydrogenation activity. After 30 min, the yield of hexitol was 39.3% at a conversion of 85.5% under conditions of 518 K, 6 MPa H_2 . In their study, small amounts of low-carbon glycols such as propylene glycol and EG were produced because glucose is more active than the corresponding hexitols.

Zhang and coworkers performed the hydrogenation of cellulose under the catalysis of tungsten carbide to replace the high-priced noble metal catalysts used previously [249, 250]. Tungsten carbide was found to give a higher yield of EG than platinum and ruthenium catalysts under reaction conditions of 518 K, 6 MPa H_2 , and 30 min. Furthermore, the yield of EG increased significantly from 27% to 61% with the promotion of a small amount of nickel. When using a 3D mesoporous carbon scaffold to support tungsten carbide NPs, the selectivity toward EG could be improved further to 72.9% [251].

Zhang also developed a series of transition metal-W bimetallic catalysts capable of EG formation from cellulose in one step [252]. Among the catalysts they employed, Ni5-W15/SBA-15 catalysts give a yield of EG as high as 75% at 518 K, 6.0 MPa H_2 . In their subsequent studies [253], they found that the homogeneous tungsten bronze species functioned as a uniquely active species for the C–C scission of glucose during the formation of glycolaldehyde, which was further hydrogenated to EG catalyzed by a metal active site. Tungsten trioxide promoted ruthenium catalysts were also proven to show high activity in the hydrogenolysis of cellulose to yield glycols by Liu [175, 254], where WO_3 was found to promote the hydrolysis of cellulose as well as the efficient C–C bond cleavage of the sugar.

To explore a catalyst that can effectively convert cellulose at low cost, Mu and coworkers evaluated Ni-based catalysts supported on various supports (Al_2O_3 , kieselguhr, TiO_2 , SiO_2 , ZnO, ZrO_2 , and MgO in previous investigations) [255]. It was found that a 20% Ni/ZnO catalyst can convert the cellulose completely and give a 70.4% yield of total 1,2-alkanediols. The main drawback of this catalyst lies in its poor hydrothermal stability. They also prepared a series of Ni–Cu/ZnO bimetallic catalysts that have been successfully applied to the hydrogenolysis of cellulose and real biomass substrates (including cornstalk and corncob) for the purpose of producing 1,2-alkanediols as the major products [256]. $2Ni_3Cu_5ZnO$ catalyst displayed the best 1,2-alkanediol selectivity (72.5%), with 74% cellulose conversion at 518 K, 4 MPa H_2 .

5.3.2 Conversion of Biomass via Platform Molecules The selection of the platform molecules was initially performed by the US Department of Energy (DOE) [257] in 2004 and revisited recently by Bozell and Petersen [258], including sugars (glucose and xylose), polyols (sorbitol, xylitol, and glycerol), furans (furfural and HMF), and acids (succinic, levulinic, and lactic acids). They were selected considering several indicators such as the availability of commercial technologies for their production and their potential to be simultaneously transformed into fuels and chemicals in facilities called biorefineries.

5-Hydroxymethyl furfural (5-HMF), a Versatile Platform Chemical The development of efficient methods for HMF production from carbohydrates has been ongoing for almost a century. On the basis of the solvent system used, synthesis of HMF from carbohydrates can roughly be divided into three types of processes: traditional single-phase systems, biphasic systems, and IL-based systems.

It was shown earlier that the dehydration of aqueous solutions of fructose in the presence of liquid or solid acid catalysts resulted in modest yields of 5-HMF because of the formation of levulinic acid, formic acid, and humins. The use of organic molecules such as methyl isobutyl ketone (MIBK), acting as an extracting solvent, increases the yield of 5-HMF. Thus, a 74% yield was obtained in batch mode in a mixture of water and MIBK in the presence of dealuminated mordenites at 165 °C [259]. Binder and Raines reported a 92% yield of 5-HMF when fructose was dehydrated with an H₂SO₄ catalyst in a *N,N*-dimethylacetamide (DMA) solution with an additive of LiBr or KI [260].

Cheap and abundantly available glucose is the desired starting material for the production of HMF, although yields are typically low for this feedstock. In 2007, Zhang and coworkers made an important advance in the synthesis of HMF from glucose [261]. Using a system of 10 mol% of CrCl₂ in an IL (1-ethyl-3-methylimidazolium chloride, [EMIM]Cl), they were able to obtain a 70% yield of HMF at 95% conversion. Pidko and coworkers combined X-ray absorption spectroscopy (XAS), DFT, and kinetic experiments to confirm the role of Cr in the isomerization of glucose to fructose [262], in which the ring opening of glucose is catalyzed by a mononuclear Cr complex and the actual isomerization to fructose proceeds through a binuclear Cr complex.

The use of ILs combined with catalysts to obtain much higher 5-HMF yields comes not only from glucose but also from cheaper carbohydrates such as sucrose, inulin, starch, cellulose, and even lignocellulosic materials [263, 264]. However, furfural and HMF are not attractive fuel components because of their melting point and stability. They can be used as starting materials to produce a variety of high-value-added furan derivatives, as well as to produce liquid alkanes and fuel additives. Plentiful work has already been carried out on the conversion of HMF into fuels and chemicals.

One of the most attractive furan derivatives as an alternative to gasoline blending is 2,5-dimethylfuran (DMF). The most general method to obtain DMF is the reduction of both formyl and hydroxyl groups of HMF using supported metal catalysts in an organic solvent such as butanol. 2,5-DMF was obtained with a 71% yield by vapor phase hydrogenolysis of 10 wt% 5-HMF in 1-butanol solution in a flow reactor loaded with a Cu–Ru/C catalyst [265]. A 95% yield of 2,5-DMF was obtained by heating a solution of 5-HMF in refluxing tetrahydrofuran in the presence of formic acid, H₂SO₄, and Pd/C catalyst [266].

The efficient hydrogenation of HMF into 2,5-bis-hydroxymethylfuran (BHMF) was performed using a Cu/SiO₂ catalyst [267], obtaining as high as 97% BHMF yield. In the presence of acidic ZSM-5 zeolite, the synthesized BHMF further reacted with methanol, leading to a 70% yield of corresponding 2,5-bis-methoxymethylfuran (BMMF). The target product BMMF is an excellent cetane number improver for diesel, as proven by its cetane number of 80, high flash point (90 °C), and low cold filter plugging point (<−37 °C).

To upgrade furan platform molecules into liquid alkanes with higher numbers of carbons able to be used in gasoline, diesel, and jet engines, different strategies for C–C coupling have been proposed. Dumesic *et al.* [268] proposed a process for obtaining diesel fuels of high quality from the Aldol condensation of HMF or furfural with acetone, followed by hydrogenation and deep dehydrodeoxygenation. The condensation of HMF with acetone was carried out in a biphasic reactor where furan

dissolved in THF is contacted with aqueous NaOH solution at room temperature. The single condensation product (4-(5-(hydroxymethyl)furan-2-yl)but-3-en-2-one), a C₉ intermediate, can additionally react with a second molecule of HMF to produce a C₁₅ oxygenated fuel precursor. Finally, the hydrogenated Aldol compounds are subjected to a hydrogenation/dehydration/ring-opening process in the presence of bifunctional catalysts such as Pd/Al₂O₃ (at 373–413 K and 25–52 bar of H₂) and Pt/NbPO₅ (at 528–568 K and 60 bar of H₂), producing a mixture of linear C₉ and C₁₅ alkanes in 73% yield. Very recently, Xia and coworkers reported a direct and efficient approach for the production of liquid alkanes from biomass-derived Aldol adducts (furfural-acetone (FA), 5-hydroxymethylfurfural-acetone (HMFA), di-furfural-acetone (DFA), and di-5-hydroxymethylfurfural-acetone (DHMFA)) over a multifunctional Pd/NbOPO₄ catalyst under mild conditions [269]. Octane is obtained in very high yield (94%) from the direct conversion of FA, and the catalyst can be used for 256 h without deactivation at 170 °C and 2 MPa, which is the best performance reported so far.

The hydrogenolysis of C–O bonds in furan and its derivatives has been studied more and more in recent years. One typical example is the hydrogenolysis over Rh or Ir catalysts modified with ReO_x, which we discovered recently [270]. The systems selectively dissociate the C–O bond neighboring another –CH₂OH group in the substrate, enabling the conversion of tetrahydrofurfuryl alcohol to 1,5-pentanediol in high yield. Yao *et al.* reported an one-step conversion of HMF over Ni–Co–Al mixed oxide catalysts derived from corresponding HT-like compounds [271]. 1,2,6-Hexanetriol was obtained in 64.5% yield under mild reaction conditions.

Levulinic Acid/ γ -Valerolactone Platform Levulinic acid (4-oxopentanoic acid) can be considered one of the most important compounds on the selected list of platform molecules derived from biomass due to its reactive nature along with the fact that it can be produced from lignocellulose wastes at low cost. The biorefinery process was developed at the industrial scale for the production of levulinic acid from cellulose and hemicellulose present in agricultural or forest residues. The raw material was hydrolyzed and dehydrated by acidic treatments in a first reactor, yielding 5-HMF, which was recovered and converted in a second reactor to levulinic acid with a 60% yield with respect to the monomers contained in the starting cellulosic materials [272].

γ -Valerolactone (GVL) has been identified as a renewable platform molecule with potential impact as a feedstock in the production of both energy and fine chemicals. GVL is obtained by hydrogenation of levulinic acid. The reduction of levulinic acid to GVL using external H₂ has been typically performed using a metal catalyst, such as Ru, Pd, Pt, Ni, Rh, Ir, or Au, on different supports. Among them, Ru catalysts have shown high performance to reduce levulinic acid or its esters to GVL. Manzer showed that GVL was obtained with a 97% yield by the hydrogenation of levulinic acid at 150 °C over a 5 wt% Ru/C catalyst [273]. Pt/TiO₂ or Pt/ZrO₂ catalysts afforded a continuous hydrogenation of levulinic acid with marginal deactivation over 100 h, yielding 95% GVL [274]. Deng has demonstrated that an inexpensive, recyclable RuCl₃/PPh₃/pyridine catalyst system can be used to convert a 1 : 1 aqueous mixture of levulinic acid and formic acid into GVL in high yields [275].

GVL retains 97% of energy content of glucose and performs comparably to ethanol when used as a blending agent (10% v/v) in conventional gasoline [276]. GVL suffers, however, from several limitations for widespread use in transportation sector, such as high water solubility, blending limits for use in conventional combustion engines, and lower energy density compared to petroleum-derived fuels. Although these limitations can be at least

partially alleviated by reduction of GVL with hydrogen to methyltetrahydrofuran [277], which can be blended up to 70% in gasoline, the limitations would be completely eliminated by converting GVL to liquid alkenes (or alkanes) with molecular weights targeted for direct use as gasoline, jet, and/or diesel fuels.

Bond *et al.* reported a strategy by which aqueous solutions of GVL, produced from biomass-derived carbohydrates, can be converted to liquid alkenes with a range of molecular weight appropriate for transportation fuels by an integrated catalytic system that does not require an external source of hydrogen [278]. The GVL feed undergoes decarboxylation at elevated pressures (e.g., 36 bar) over a silica/alumina catalyst to produce a gas stream composed of equimolar amounts of butene and carbon dioxide. This stream is fed directly to an oligomerization reactor containing an acid catalyst (e.g., HZSM-5 and Amberlyst-70) that couples butene monomers to form condensable alkenes with molecular weights that can be targeted for gasoline and/or jet fuel applications.

Polyol Platform for Liquid Hydrocarbon Fuels The aqueous-phase reforming (APR) of alcohols and polyols (glycerol, EG, glucose, and sorbitol) using platinum-based catalysts, first introduced by Dumesic and coworkers [242, 279], is an interesting approach for the production of renewable hydrogen that can be used directly as energy, in hydrogen fuel cells or as an external source of hydrogen for biomass-upgrading processes. However, through the adequate selection of metal, support, and reaction conditions, the selectivity of the APR process can be tuned toward the production of light alkanes [280]. For instance, the aqueous-phase reforming of methanol and EG over Pt-black or Pt supported on TiO_2 , Al_2O_3 , or ZrO_2 favors the C–C bond cleavage selectively producing hydrogen [281], while other metals such as Rh, Ru, and Ni favor the C–O cleavage, rather than C–C, leading to the production of alkanes. Another strategy for the removal of the oxygenated groups of polyols, such as sorbitol, is through the dehydration of hydroxyl groups followed by hydrogenation of the resulting unsaturated compounds. The process, denoted as aqueous-phase dehydration–hydrogenation (APDH), can be performed over bifunctional catalysts bearing acidic and metal sites such as $\text{Pt/SiO}_2\text{–Al}_2\text{O}_3$ [243, 282] or Pt supported on niobium-based solid acids at 520 K and near 50 bar [283]. The dehydration of hydroxyl groups takes place on the acid sites, producing unsaturated species such as alkenes or carbonyl compounds and even heterocyclic ring structures, which are subsequently hydrogenated to alkanes. However, this strategy is limited to the production of alkanes with the number of carbon atoms same as the starting feedstock. An alternative approach that allows obtaining higher alkanes was developed by Kunkes *et al.* [284], consisting of a two-step cascade process that combines removal of oxygen and a C–C coupling reaction. First, sugars and polyols are partially deoxygenated (up to 80%) by C–O hydrogenolysis over a Pt–Re (10 wt%)/C catalyst at approximately 573 K. A mixture of different monofunctional organic compounds in C4–C6 range that contains acids, alcohols, ketones, and heterocycles and separates spontaneously from the aqueous phase is obtained. An important point is that hydrogen required for deoxygenation is internally supplied by the aqueous-phase reforming of a part of the feed on a multifunctional Pt–Re/C catalyst. In a subsequent step, this mixture of monofunctional compounds is upgraded to higher HCs through different C–C coupling reactions such as Aldol and ketonization processes. However, a limitation of the process is high cost of the catalyst.

5.3.3 Concluding Remarks and Prospects In conclusion, nanocatalysts show great potential for the production of biofuel and biochemicals. To improve the reaction efficiency

to make it competitive with the current oil refining, a number of challenges need to be addressed: (i) the design of more active and selective nanosized catalysts with high hydrothermal stability for tailoring the reactions to target fuels and chemicals and (ii) the development of more versatile catalytic systems, based on nanosized catalysts and green solvents, able to process a range of biomass, especially raw lignocellulosic feedstocks.

5.4 Nanomaterials for Photocatalytic Applications

Photocatalysis, in which solar photons are used to drive redox reactions to produce chemicals, is a sustainable, nonhazardous, and economically viable route to utilize abundant, clean, and safe solar light energy. Enormous efforts have been devoted to heterogeneous photocatalysis after the pioneering discovery of ultraviolet (UV)-light-induced photoelectrochemical water splitting on TiO_2 surfaces in 1972 [285].

Many semiconductor materials were developed as active photocatalysts. Photocatalysts are usually photostable and chemical inert solid semiconductors that are able to absorb visible/UV light. The semiconductors such as TiO_2 , ZnO , CeO_2 , WO_3 , Fe_2O_3 , GaN , CdS , and ZnS could act as photoactive materials for redox/charge-transfer processes due to their electronic structures, which are characterized by a filled VB and an empty conduction band [286]. Among them, TiO_2 -based materials have shown great potential as ideal and powerful photocatalysts due to its unique physical and chemical characteristics with high thermal and chemical stability, nontoxicity, and high reactivity. So far, TiO_2 -based photocatalysts have been widely used in applications of the removal of organic compounds from environment, dissociation of water, solar energy conversion, and disinfection. The photocatalytic performance can be improved by adjusting the optical, electronic, structural, morphological, and surface properties as well as its size and crystallinity.

5.4.1 Properties of TiO_2 Nanomaterials

Structure of TiO_2 TiO_2 has three crystalline polymorphs in nature: rutile, anatase, and brookite, as shown in Figure 10. The three phases can be described in terms of TiO_6 octahedral chains. They differ by the distortion of each octahedron and the assembly pattern of resulting octahedral chains. Anatase TiO_2 has a structure of edge-sharing TiO_6 octahedra,

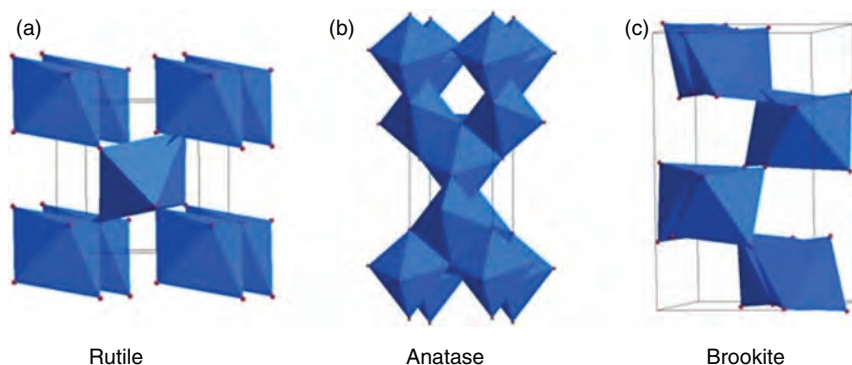


Figure 10 Schematic unit cell structures of three TiO_2 polymorphs: (a) rutile, (b) anatase, (c) brookite.

while the rutile and brookite frameworks have both corner and edge-sharing configurations. The different characteristics of Ti–O bonds play an important role in structural and electronic features of different phases. Brookite TiO_2 is a more exotic titania polymorph with a layered structure. The crystal structures of TiO_2 nanomaterials depend largely on the preparation method, especially the temperature. Nano- TiO_2 anatase is usually prepared by a low-temperature synthesis method. Nano- TiO_2 rutile is more easily obtained from high-temperature calcination. Brookite phases are less common and are mainly obtained from solution-based methods at low temperature. Different phases have significantly different properties and performance. Rutile is the most stable phase in bulk form, while anatase and brookite are common in fine-grained natural and synthetic samples. The anatase and brookite will be transformed into rutile upon heating under high temperature. This relationship of phase stability also exists in TiO_2 nanomaterial formations. The surface enthalpies of the three polymorphs are sufficiently different that crossover in thermodynamic stability can occur under conditions that preclude coarsening, with anatase or brookite stable at small particle sizes. As reported by Diebold *et al.* [287], when heating temperature ranges from 325 to 750 °C, anatase is the most stable phase between 11 and 35 nm, while the sizes of rutile are all above 35 nm. The different phase stability is strongly controlled by physical environment and the interaction between TiO_2 and H_2O [288].

Optical and Electronic Properties of TiO_2 Nanomaterials The electronic and optical properties are closely related to the small size of the nanomaterials, due to size effects. The changes of shape and lattice parameter of nanocrystals from their bulk counterparts are also greatly influenced by the nanoscale effects. Generally, TiO_2 has a band gap energy in 3.0–3.4 eV range, which depends on the crystal phases, particle size, and morphology. The band gap energy of nanomaterials increases with the decreasing size. The shifting of the valence and conduction bands and their alignment with certain redox potentials could be optimized to facilitate the corresponding redox reactions occurring on the TiO_2 NP surfaces.

The electronic band structure of TiO_2 is very important for its applications in photocatalysis. In general, in a photocatalysis process, electron–hole pairs are created inside TiO_2 upon absorbing photons with energy larger than the band gap. The photogenerated charges then separate and transfer outside to react with chemicals adsorbed on the TiO_2 surfaces. The photocatalytic efficiency is controlled by light absorption, charge transport, the number of surface reaction sites, and the redox reaction rates. The range of light absorption wavelength can be adjusted by engineering the electronic band structure of TiO_2 .

5.4.2 Modification of TiO_2 Nanomaterials TiO_2 has attracted much research attention in recent decades owing to its promising applications in environmental remediation and solar energy conversion. However, its large band gap of 3.2 eV, which can only be activated by UV light irradiation, and low quantum efficiency limit its practical application. Various modifications of TiO_2 were used to make it sensitive to visible light and also inhibit the recombination of photogenerated charge carriers, which limits its overall photocatalytic efficiency.

Metal Doping of TiO_2 One of the main approaches to develop visible light photocatalysts is to dope foreign atoms into UV-active catalysts to extend their optical absorption to visible light. Various TiO_2 -based materials have been developed on the basis of this strategy [289–291]. So far, many metal ions, including transitional metal, rare earth metal, and noble metal ions, have been used to modify the optical and photocatalytic properties

of TiO_2 . Some metal ions such as V^{5+} , Cr^{3+} , and Fe^{3+} have been reported to extend the photoactive region of TiO_2 to visible light [292, 293]. Choi *et al.* performed a systematic study on the photocatalytic activity of TiO_2 NPs doped with 21 transition metal elements on oxidation of CHCl_3 and reduction of CCl_4 [294, 295]. It was reported that the photocatalytic performance was closely related to the electron configuration of dopant ion, while closed electron shells in the dopant ions had no effect on the activity. The results showed that Fe^{3+} , Mo^{5+} , Ru^{3+} , Os^{3+} , Re^{5+} , V^{4+} , and Rh^{3+} doping of TiO_2 significantly increased the photocatalytic activity, while Co^{3+} and Al^{3+} doping decreased the photoreactivity. The presence of metal-ion dopants in TiO_2 matrix significantly influenced the charge carrier recombination rates and interfacial electron-transfer rates.

Nonmetal Doping of TiO_2 Doping with nonmetal ions is also an effective way to modify the photocatalytic properties of TiO_2 . It has been proven that doping of anionic elements as nitrogen, carbon, and sulfur into TiO_2 could result in a shift in the onset of the absorption of TiO_2 to visible light, thus increasing its overall photocatalytic efficiency. Asahi *et al.* reviewed the chemical synthesis, physical properties, and applications of N-doped TiO_2 NPs, with a special emphasis on titania-based NPs [296]. N-doped TiO_2 powder can be prepared either by oxidation of titanium nitride (TiN) powder in an O_2 gas flow or by nitrication of TiO_2 powder in an ammonia gas flow. N-doped TiO_2 NPs can also be prepared by employing the direct amination of nanosized titania particles [297]. Doping nitrogen into TiO_2 on nanometer scale can lead to higher nitrogen concentrations than that in thin films and micrometer-scale TiO_2 powders, resulting in enhanced catalytic activity. The amount of N doped into TiO_2 can be controlled when using an NH_3 flow by changing the annealing temperature in the range of 550–600 °C [298]. Chen *et al.* found that postirradiation annealing is a simple method for improving both activity and stability of N-doped TiO_2 catalyst for photocatalytic oxidation (PCO) of ethylene under visible light. The annealing effectively minimizes surface defects, facilitates the adsorption of oxygen molecules, and removes adsorbed NH_3 from the catalyst surface, which contributes to the enhanced photocatalytic performance of N-doped TiO_2 [299].

Doping with other nonmetals including C [300], F [301], S [302], and B [303] also cause significant improvement of the visible light photocatalytic activity. The origin of the improvement is very intricate. The nonmetal dopant is located either at a substitutional site in the TiO_2 lattice or at an interstitial one that may bind to lattice atoms, which would provide different states in the band gap of TiO_2 . For example, Sakthivel and Kisch reported the preparation of C-doped TiO_2 NPs by hydrolysis of TiCl_4 with tetrabutylammonium hydroxide, showing an efficient photocatalytic degradation of 4-chlorophenol and azo dye Remazol Red under visible light irradiation [304].

TiO_2 -Based Nanoheterostructures Semiconductor nanostructures have also been widely used for light harvesting [305] and light generation [306]. Coupling with different semiconductive materials with appropriate electronic band structures and band edges is another effective way to achieve charge separation in nanostructured semiconductors. It has been proven that the coupling of TiO_2 nanostructures to a semiconductor of wide band gap, such as SnO_2 [307], SrTiO_3 [308], or ZnO [309], to form a heterojunction could promote charge separation, improving the photocatalytic performance of TiO_2 -based photocatalysts. For example, Wang *et al.* prepared hierarchical $\text{SnO}_2/\text{TiO}_2$ nanomaterials by combining electrospinning technique with hydrothermal method [310]. By adjusting the preparation parameters, the SnO_2 nanostructures were uniformly distributed on TiO_2 nanofibers, and

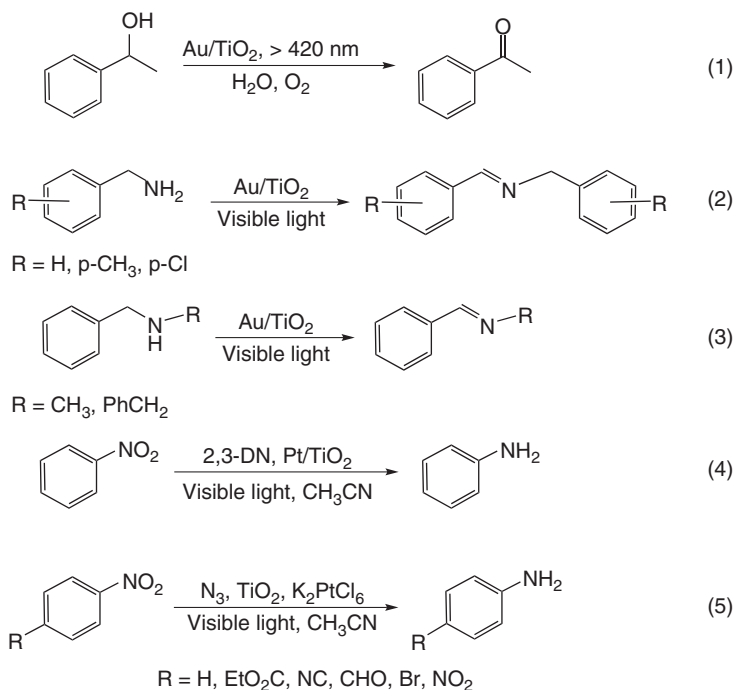
their morphology could be controlled. The resulting heterostructured $\text{SnO}_2/\text{TiO}_2$ nanomaterials show high photocatalytic activity. Cao *et al.* synthesized $\text{SrTiO}_3/\text{TiO}_2$ nanofibers by an *in situ* hydrothermal method using TiO_2 as both a template and reactant [311]. By simply adjusting the concentration of precursor $\text{Sr}(\text{OH})_2$ and reaction temperature, the morphology and density of SrTiO_3 nanostructures can be controlled to improve the photocatalytic properties of TiO_2 .

5.4.3 Photocatalytic Applications

Photocatalytic Hydrogen Production from Water Nanosized TiO_2 photocatalytic water-splitting technology offers a promising way for clean, low cost, and environmentally friendly production of hydrogen by solar energy [312]. Presently, the efficiency of energy conversion from solar to hydrogen by TiO_2 photocatalytic water splitting is still low, mainly due to the recombination of photogenerated electron/hole pairs, fast backward reaction, and inability to utilize visible light. To resolve the above problems and make solar photocatalytic hydrogen production feasible, continuous efforts have been made to enhance the visible light response and improve the photocatalytic activity. Many methods including the addition of electron donors, addition of carbonate salts, noble metal loading, metal-ion doping, anion doping, dye sensitization, composite semiconductors, and metal-ion implantation have been proved to be useful to enhance hydrogen production. It has been reported that metals including Pt, Au, Pd, Rh, Ni, Cu, and Ag are very effective for the enhancement of TiO_2 photocatalysis. The deposited metal on the surface of TiO_2 greatly reduces the possibility of electron–hole recombination, resulting in efficient separation and stronger photocatalytic reactions. Lee *et al.* found that a considerable amount of photocatalytic H_2 was produced from water over NiO/TiO_2 with CN^- as a hole scavenger [313]. Galinska and Walendziewski found that sacrificial reagents such as methanol, Na_2S , EDTA, and I and IO_3^- ions play an important role in hydrogen production via photocatalyzed water-splitting reaction with Pt/TiO_2 as a photocatalyst [314].

Photocatalytic Organic Synthesis Heterogeneous photocatalysis has been flourishing with recent collaborative efforts of chemists and material scientists, culminating in the development of environmentally friendly and energy sustainable strategies for selective redox organic synthesis. The specific selective redox organic transformations in which these catalysts are applicable include (i) the oxidation of alcohols, amines, alkene, and alkanes, (ii) hydroxylation of aromatic compounds with O_2 , and (iii) the reduction of nitrobenzenes to corresponding aminobenzenes or azo benzenes with sacrificial agents under O_2 -free conditions.

TiO_2 -supported Au, Ag, and Cu NPs are excellent heterogeneous catalysts for thermally induced redox conversions, which also facilitate the progress of the photocatalysis. For example, Au NPs loaded at the interface of anatase/rutile TiO_2 could serve as efficient photocatalysts for aerobic oxidation of alcohols to corresponding carbonyl compounds in toluene or water under visible light irradiation (Equation 1, Scheme 4). Au NPs alloyed with Cu on TiO_2 ($\text{Au-Cu}/\text{TiO}_2$) can enhance the oxidation activity of benzyl alcohols with O_2 under visible light or sunlight irradiation [315]. For $\text{Au-Cu}/\text{TiO}_2$, the oxidation and restoration of surface Cu^0 by surface plasmons of Au NPs lead to an improvement in electron transfer and promote the overall aerobic oxidation process. Parrino *et al.* reported that Au/TiO_2 (rutile) can function as a photocatalyst for selective oxidation of primary benzyl amines to imines under solvent-free conditions or in CH_3CN (Equation 2, Scheme 4). The



Scheme 4 Redox conversions catalyzed by TiO₂-supported metal nanoparticles.

aerobic oxidation of secondary benzyl amines to imines was also successful on Au/TiO₂ under visible light irradiation (Equation 3, Scheme 4) [316].

A visible-light-absorbing surface complex can also form when colorless organic molecule, 2,3-dihydroxynaphthalene (2,3-DN), is adsorbed on the surface of anatase TiO₂ via strong bonding with ortho-dihydroxyl on the aromatic ring (Equation 4, Scheme 4) [317]. When used in combination with a common reduction cocatalyst Pt NPs, the surface complex could photocatalyze the reduction of nitrobenzene to aminobenzene with triethanolamine (TEOA) when exposed to visible light irradiation ($\lambda > 420$ nm). The combination of a metal complex of organic dye with a TiO₂ photocatalyst could efficiently reduce nitrobenzenes to aminobenzenes with TEOA under visible light irradiation (Equation 5, Scheme 4).

5.4.4 Conclusions TiO₂ nanomaterials possess a large specific surface area and unique attributes in chemical, physical, optical, electronic, and photocatalytic fields, which could effectively degrade organic pollutants in water and air, selectively transform organic chemicals in organic synthesis, and produce hydrogen from water. TiO₂ nanomaterials play an important role in environmental protection and in search for renewable and clean energy technologies.

6 NANOCATALYSTS FOR ENVIRONMENTAL REMEDIATION

The sensitive detection and efficient removal of an increasing number of persistent and emerging environmental pollutants are major challenges in our industrialized world. These

challenges can be better resolved by utilizing the advantages of nanotechnology in addition to traditional methods. NPs, which have unique physical and chemical properties, are promising materials in our overall strategies to detect and remediate environmental pollutants. The large surface-to-volume ratio of NPs particularly favors sensitivity enhancement and miniaturization. Depending on their core materials, NPs can possess unique optical, electronic, and magnetic properties. These properties vary with their surrounding chemical environment, providing a foundation for pollutant sensing. To further enhance their sensitivity, NPs can also be decorated with a wide range of small organic molecules or polymers by surface modifications. Each of these unique features allows researchers to design novel detection or removal systems that offer significant advantages in terms of sensitivity, selectivity, reliability, and practicality. This section provides a review on the use of NPs in removal of environmental pollutants in recent years.

6.1 Catalytic Reduction of NO_x

Nitrogen oxides (NO_x) have become a major source of air pollution, which can result in photochemical smog, acid rain, and ozone depletion and exhibit strong respiratory toxicity, endangering human health. Stringent environmental legislation has been passed worldwide to reduce NO_x emitted from mobile and stationary resources, including vehicles and coal-fired power plants. The selective catalytic reduction (SCR) of NO_x using reductants such as NH₃, urea, or HCs in oxygen-rich exhausts is a highly efficient way to reduce NO_x emissions, although it remains one of the major challenges in the field of environmental catalysis.

6.1.1 SCR of NO_x with NH₃ The selective catalytic reduction of NO with NH₃ (NH₃-SCR) is an effective and economical method to remove NO according to the following reaction:



Currently, the most widely used catalyst system is V₂O₅–WO₃/TiO₂ or V₂O₅–MoO₃/TiO₂ in a relatively narrow temperature window of 350–400 °C [318, 319]. Vanadium-based NH₃-SCR catalysts have also been successfully used for the de-NO_x process from diesel engines since 2005. However, disadvantages remain for the vanadium-based catalysts, including the low N₂ selectivity in high temperature range because of N₂O formation and NH₃ overoxidation, the toxicity of vanadium pentoxide to environment, high conversion of SO₂ to SO₃ with increasing vanadium amount that results in catalyst deactivation, the easy sublimation of V₂O₅, and phase transformation of the TiO₂ support from anatase to rutile at high temperatures, all of which greatly restrict their further application, especially when stricter regulations are established for NO_x for diesel engines. Therefore, many researchers have focused mainly on the exploitation of vanadium-free NH₃-SCR catalysts with high de-NO_x efficiency, high N₂ selectivity, excellent hydrothermal stability, and insensitivity to coexisting poisoning components in the SCR atmosphere such as H₂O, SO₂, HCs, or alkali metals.

Currently, metal oxide catalysts are a type of well-studied vanadium-free catalyst for the NH₃-SCR process in heavy-duty diesel engines, some of which show great potential in practical use. Early in the 1980s, Kato *et al.* [320] used Fe₂O₃ as the active phase in a NH₃-SCR catalyst (i.e., Fe₂O₃–TiO₂ mixed oxide catalyst) with high SCR activity and N₂ selectivity at relatively high temperatures, and thereafter numerous types of Fe₂O₃-containing

catalysts have been developed by researchers, including $\text{Fe}_2\text{O}_3\text{-SiO}_2$ [321] and Fe_2O_3 supported on AC [322] or activated carbon fiber (ACF) [323]. Mou *et al.* creatively synthesized novel $\alpha\text{-Fe}_2\text{O}_3$ nanorods and $\gamma\text{-Fe}_2\text{O}_3$ nanorods by aqueous precipitation and calcination/refluxing methods [324], resulting in the same morphology but totally different exposed crystal facets. They concluded that the $\gamma\text{-Fe}_2\text{O}_3$ nanorods enclosed by reactive (110) and (100) facets, simultaneously exposing Fe^{3+} and O^{2-} sites, are highly active for the activation of NH_3 and NO. Fe-exchanged zeolite catalysts usually show good SCR activity in the high temperature range with remarkable H_2O and SO_2 durability, such as Fe-ZSM-5 by Ma and Grünert [325] and Fe-Ce-ZSM-5 by Carja *et al.* [326]. Brandenberger *et al.* recently systematically studied different Fe sites located in Fe-ZSM-5 catalysts and correlated them with measured NH_3 -SCR activity [327]. They concluded that below 300°C , only monomeric Fe species contribute to the SCR reaction, and this type of Fe species does not catalyze the unselective oxidation of NH_3 , which is beneficial to high N_2 selectivity.

In practical use, the low-temperature NH_3 -SCR activity of Fe-based zeolite catalysts still needs improvement to meet the diesel emission standards for cold-start and idle speed processes. The relevant methods include the addition of catalyst promoters such as Ce, Ga, and noble metal Pt, together with the tuning of reaction atmosphere, such as raising the NO_2 ratio in NO_x to facilitate the “fast SCR” reaction [328] and adding a small amount of NH_4NO_3 solution as an effective oxidant for NO, creating similar “fast SCR” reaction conditions. In addition, to enable practical utilization of catalysts, the deactivation effects of inorganic components (i.e., Ca, Mg, Zn, P, B, and Mo) contained in diesel exhaust on Fe-based zeolite catalysts are also worthy of investigation.

6.1.2 SCR of NO_x with Hydrocarbons (HC-SCR) Although NH_3 effectively reduces NO_x , some aspects, such as storage technologies, transportation/leakage, and corrosion, need further improvement. One possible technique circumventing these problems is selective catalytic reduction of NO_x using HCs, that is, fuel or derivatives from the fuel, HC-SCR. The distinctive advantage of HC-SCR is that the on-board fuel can be used as the reductant for NO_x conversion, thus reducing the cost involved in the development of infrastructure for delivering the reductant to the automotive engine exhaust system. Since the pioneering work of Iwamoto *et al.* [329] and Held *et al.* [330], many catalysts such as zeolitic oxide, base oxide/metal, and noble metal catalysts have been found to be effective for the HC-SCR in the presence of excess oxygen.

Among the catalysts proposed for HC-SCR technology, zeolite-based catalysts such as ZSM-5, Y, and Beta types have received attention for their applicability in the HC-SCR of NO_x as a result of their high activity within a wide temperature window [331–333]. Transition metals (e.g., Fe, Co, and Cu) embedded in a zeolite matrix show a higher catalytic activity and selectivity in de- NO_x than their parent zeolites [334–336]. In recent years, Cu-zeolite catalysts have been extensively studied for de- NO_x reaction because of their low cost, durability, and low-temperature activity [337–339]. There is evidence that isolated copper ions are the active sites for the HC-SCR, and small CuO crystallites can accelerate direct oxidation of HCs [340]. Moreover, the catalytic properties of active copper phase can be greatly influenced by the dispersion of copper species and the nature of support [341].

Up to now, alumina-supported silver ($\text{Ag/Al}_2\text{O}_3$) has been known to be one of the most effective catalysts for HC-SCR, even in the presence of water vapor and SO_2 [342, 343]. Improvement of the HC-SCR activity of $\text{Ag/Al}_2\text{O}_3$ catalysts has been shown to depend strongly on (i) the Ag loading and, in particular, the Ag surface density of catalysts, (ii) the

nature of reducing HC, with oxygenated and higher HCs providing better HC–SCR performances at lower temperatures, and (iii) the preparation method.

The most spectacular low-temperature promoting effect on HC–SCR reaction undoubtedly lies in addition of a limited quantity of H_2 , generally below 1%, to the reacting feeds. The so-called hydrogen effect has been confirmed for C_3H_8 –SCR and for HC–SCR using higher HCs [344]. There is an alternative solution to improve the SCR activity at low temperatures. Since the first discovery by Miyadera [345] that the catalytic performance of SCR reaction over Ag/Al_2O_3 was significantly improved by applying oxygenated HCs, such as ethanol, propanol, and acetone, the SCR of NO_x with these compounds has been widely studied, in particular for ethanol due to the incorporation of ethanol into diesel fuel [346–348]. These results indicate that oxygenated HCs could be alternatives for the SCR of NO_x with HCs contained in the exhaust or with oxygenates added prior to the catalysts on heavy-duty vehicles by carrying on-board external tanks.

6.2 Catalytic Oxidation of Formaldehyde

Formaldehyde is emitted from building and furnishing materials and consumer products and is known to cause irritation of eyes and respiratory tract, headaches, pneumonia, and even cancer. It is a dominant indoor air pollutant, especially in the developing countries, and significant efforts have gone into indoor HCHO purification to meet environmental regulations and human health needs.

For lowering the concentration of formaldehyde in indoor environments, different techniques have been developed. Among these techniques, surface treatment using reactive or diffusion-resistant coatings and fumigation with ammonia can be applied for the treatment of very high concentrations of formaldehyde. The reaction with ammonia, which yields hexamethylenetetramine, has been consequently used in prefabricated houses [349]. The design of intelligent housing construction and ventilation systems has also been proposed to reduce pollutant levels. PCO systems for the removal of formaldehyde have become popular recently [350]. Wall paints containing modified TiO_2 are frequently recommended, but their efficiency has not yet been proven. In addition, authors have demonstrated that under the influence of light, photocatalytic wall paints could produce undesired secondary products, which have toxicities as high as that of formaldehyde. Moreover, when the concentration of volatile organic compound (VOC) decreases below 1 ppm, the conversion rates decrease remarkably. The adsorption of HCHO on AC and other adsorbents (including potassium permanganate, aluminum oxide, microporous zeolitic materials, and some ceramic materials) is also proposed as an efficient method of emission control [351]. However, the effectiveness of sorbent is typically limited by low adsorption capacities, and competitive adsorption occurs when both water (present in ambient air) and formaldehyde molecules are present. As a consequence, adsorption of formaldehyde is reduced significantly when relative humidity increases.

The complete catalytic oxidation (CCO) of formaldehyde is an attractive alternative to other proposed processes because of its high effectiveness in achieving the total conversion of formaldehyde into harmless CO_2 and water at much lower temperatures than in thermal oxidation [352, 353]. Therefore, the development of new catalysts (preferably free of noble metals to achieve low cost) exhibiting high catalytic activity for complete oxidation of formaldehyde at low temperatures and strong resistance to water adsorption (and other inhibitors) is actually of high relevance. The objective of the following section is to highlight recent research on elimination of formaldehyde by catalytic oxidation. There are

two major classes of catalysts for complete oxidation of VOCs: supported noble metals and supported or unsupported transition metal oxides. In the following section, a general description of the CCO mechanism for both types of catalyst will be introduced.

6.2.1 Noble Metal-Based Catalysts The CCO of formaldehyde on supported noble metals was first reported by Imamura *et al.* [354]. The authors reported a study of the effect of noble metal nature on catalytic properties when supported over CeO_2 . The authors reported the following activity order for 90% formaldehyde conversion: $\text{Ru/CeO}_2 > \text{Pd/CeO}_2 > \text{Rh/CeO}_2 > \text{Pt/CeO}_2$. Ruthenium was the most active catalyst, and it completely oxidized formaldehyde at 200 °C to produce only CO_2 and water under the reaction conditions used. Mao and Vannice studied silver-based catalysts for the oxidation of formaldehyde [355]. Silver dispersed on both high-surface-area alumina and silica was investigated. These catalysts were active below 200 °C, but significant deactivation occurred.

The use of TiO_2 (anatase) as a support for noble metals was investigated recently. 1% Pt/TiO_2 was shown to be effective for HCHO oxidation at room temperature [356], achieving 100% conversion of $\delta = 100$ ppm HCHO to CO_2 and H_2O at a gas hourly space velocity (GHSV) of 50 000 h^{-1} . However, this type of catalyst is not as active as needed for practical applications and deactivates with time-on-stream catalyst. Recently, the same group reported a novel alkali metal-promoted Pt/TiO_2 catalyst for the ambient destruction of HCHO [357]. They show that the addition of alkali metal ions (such as Li^+ , Na^+ , and K^+) to Pt/TiO_2 catalyst stabilized an atomically dispersed Pt-O(OH)_x -alkali metal species on the catalyst surface and also opened a new low-temperature reaction pathway.

Huang *et al.* recently reported the fabrication of single-atom silver chains by thermal processing from supported silver NPs on hollandite-type manganese oxide nanorods [358]. The single-atom silver catalyst showed a high ability to activate both lattice and molecular oxygen species at low temperatures. Because of the high mobility of oxygen in catalyst, excellent activities for formaldehyde oxidation at low temperatures were measured, and complete conversion was achieved below 80 °C (silver loading: 10 wt%, $[\text{HCHO}] = 400$ ppm).

6.2.2 Transition Metal Oxide-Based Catalysts The development of less expensive but effective catalysts without noble metals for catalytic oxidation of formaldehyde at low temperatures is a real challenge. Foster and Masel were, to our knowledge, the first to report the CCO of formaldehyde to CO_2 and water over metal oxides [359]. A nickel oxide catalyst was selected because of its excellent properties in catalyzing oxidation of CO. It was highlighted that nickel oxide was an active phase for catalytic combustion of formaldehyde. However, the combustion process is complex.

Among different metal oxides, MnO_x was also studied by many research groups because of its low volatility and low toxicity. The catalytic oxidation of formaldehyde over manganese oxide was first reported by Sekine and Nishimura [360]. They developed a chipboard-like air-cleaning material consisting of AC particles and manganese oxides. The material allows the conversion of formaldehyde into CO_2 even at room temperature. The material reduced the indoor formaldehyde concentration from 0.21 to 0.04 ppm. The effect of the morphology of manganese oxide on catalytic performance was further studied by He *et al.* [361]. The combination of MnO_x with other oxides generally results in an increased catalytic performance at low temperatures. Recent studies revealed that when MnO_2 was placed in the proximity of La_2O_3 or CeO_2 , the oxygen mobility in the MnO_x structure was strongly affected [362]. In Mn–Ce mixed oxide, CeO_2 provided oxygen to

manganese sites at low temperatures. Thus, CeO_2 increases the activity of MnO_x during the oxidation process at low temperatures.

6.2.3 Outlook Despite the considerable progresses in obtaining active catalysts for catalytic oxidation of formaldehyde, there are still many challenges for the development of an efficient process. As already noted, typical formaldehyde concentrations used in academic studies are at the ppm level. However, these values are far from those encountered in indoor environments (ppb level). Future studies will have to focus on the formaldehyde remediation at low concentration levels. Under these constraining conditions, original technological approaches have to be proposed. Hybrid systems combining selective formaldehyde adsorption followed by its selective destruction through catalytic oxidation can be an attractive alternative to solve the problem of formaldehyde concentrations at indoor levels.

6.3 Catalytic Degradation of Organic Pollutants

Industrial plants generate increasing amounts of wastewater, which often causes severe environmental problems. The wastewater produced in many industrial processes often contains organic compounds that are toxic and not amenable to direct biological treatment. There are a huge number of different types of organic pollutants, including organic dyes, phenols, biphenyls, pesticides, fertilizers, HCs, plasticizers, detergents, oils, greases, pharmaceuticals, proteins, and carbohydrates. Each type of pollutant has many varieties. Organic pollutants in wastewater, being highly toxic and difficult to degrade, have become one of the most serious global environmental issues today. Organic pollutants, once released into the aquatic ecosystem, can cause various environmental problems, such as clogging sewage treatment plants, adversely affecting aquatic biota, and increasing biochemical oxygen. Therefore, an effective and economical technique needs to be developed to reduce the concentration of organic pollutants before releasing the wastewater into aquatic environment. Currently, industrially available wastewater treatment technologies such as adsorption and coagulation merely concentrate or separate these pollutants from water, but do not completely “eliminate” or “destroy” them into biodegradable or less toxic organic compounds and inorganic CO_2 , H_2O , NO_3^- , PO_4^{3-} , and halide ions. Other water treatment methods, such as chemical and membrane technologies, usually involve high operating costs, and sometimes generate other secondary toxic pollutants.

Among the various physical, chemical, and biological technologies used in pollution control, the advanced oxidation processes (AOPs), including the Fenton reaction, photocatalysis, sonolysis, ozonolysis, and combinations of these, are increasingly adopted in the destruction of organic contaminants, due to their high efficiency, simplicity, good reproducibility, and easy handling. Heterogeneous photocatalysis possesses some advantages and has feasible applications in wastewater treatment, including (i) ambient operating temperature and pressure, (ii) complete mineralization of parents and their intermediate compounds without leaving secondary pollution, and (iii) low operating costs. This section highlights research progress in the application of photocatalysts in the environmental field.

6.3.1 Semiconductor Oxides for Catalytic Pollutant Degradation Photocatalysis on semiconductor catalysts (TiO_2 , ZnO , Fe_2O_3 , CdS , GaP , and ZnS) has demonstrated efficiency in degrading a wide range of organic pollutants into biodegradable or less

toxic organic compounds and inorganic CO_2 , H_2O , NO_3^- , PO_4^{3-} , and halide ions. Now, efforts have been made to improve the catalytic performance of nanostructures based on semiconductor oxides. The unique surface area and surface activity of NPs play essential roles in these catalytic reactions.

TiO₂ for Photodegradation of Pollutants Among the explored semiconductor photocatalysts, TiO_2 is the most popular, due to its durability, low cost, low toxicity, super-hydrophilicity, and remarkable chemical and photochemical stability. Titanium dioxide (TiO_2) NPs exhibit a high photocatalytic oxidation capacity to degrade organic pollutants in the presence of UV radiation. Lots of efforts have succeeded in finding ways to narrow the band gap of TiO_2 to use the abundant solar or visible light range for various chemical transformations and to stabilize anatase TiO_2 by doping TiO_2 with metal/nonmetal dopants [363–365]. For example, carbon-doped TiO_2 NPs showed an improved photocatalytic activity in visible light range, and methylene blue solution with a lower initial concentration was efficiently degraded by these nanomaterials [366]. Polymer conjugation is another common strategy to extend the photocatalytic response range of TiO_2 NPs to visible light. Methyl orange was degraded by TiO_2 NPs coated with poly(3-hexylthiophene), both under UV and visible light irradiation, with a higher efficiency than pure TiO_2 NPs [367]. Novel magnetically separable TiO_2 -guanidine-(Ni, Co) Fe_2O_4 nanocomposites (for easy recycling) have been prepared as useful catalysts to work under visible light and potentially sunlight. These nanomaterials have proven to be photocatalytically active in selective transformation of malic acid (renewable C_4 entity) to formic acid [368]. In addition, the magnetically separable TiO_2 -guanidine- NiFe_2O_4 exhibited a remarkable photodegradation activity, with complete removal and degradation of microcystins, which are the most common cyanobacterial toxins found in water (algal blooms), in particular, microcystin-LR (MC-LR) [369]. The proposed system is envisaged to pave the way to the development of more efficient and easily separable photocatalysts for visible light photodegradation of pollutants and toxins in water.

ZnO for Photodegradation of Pollutants ZnO NPs with different morphologies were synthesized, and their catalytic activities have also been investigated [370]. Because of the larger surface exposure of oxygen atoms, ZnO of flower-like particles showed higher efficacy in photocatalytic degradation of 4-chlorophenol in aqueous solution under UV irradiation compared with ZnO nanorods. One-dimensional flat ZnO nanotower arrays were also fabricated, and the improved adsorption and photocatalytic abilities on a model pollutant, eosin B, were demonstrated [371]. The photodegradation of methylene blue using manganese-doped ZnO NPs was more efficient than that using undoped ZnO in visible light [372].

Metal Loading-Enhanced Catalytic Activity of Semiconductor Oxides Several approaches to the preparation of semiconductor oxide-noble metal nanostructures have recently been reported. Au NP-loaded ZnO nanorods were prepared in aqueous solution by growing Au NPs onto ZnO nanorods [373]. Rhodamine B was completely degraded by these ZnO/Au nanocomposites within 15 min. Approximately 91% of 4-chlorophenol was removed from water after 300 min irradiation. The high degradation activity was attributed to the large surface areas of ZnO nanorods and the attached Au NPs. Another Au- TiO_2 photocatalyst was prepared by the deposition-precipitation method, and it showed a high photocatalytic activity on the degradation of an azo dye (acid red 88) [374].

However, the application of semiconductor photocatalysts for wastewater treatment faces a series of technical challenges. One typical drawback of photocatalysis is that the semiconductor photocatalysts that are normally used are not very photostable under the operating conditions. Usually, the illumination of these catalysts in aqueous media leads to their corrosion, which leads to the migration of metal ions into water, and finally complete dissolution of solid catalysts. For example, transition metal sulfides are highly unstable semiconductors of narrow band gap, and irradiation under light often leads to their dissolution. Other metal oxides, such as iron oxides with various stoichiometries, silver oxide, and copper oxides, are also susceptible to photocorrosion. In case of TiO_2 , the postseparation of TiO_2 catalyst is difficult after water treatment, which obstructs practicality in industrial processes. Second, the fine particle size of TiO_2 , together with its large surface area-to-volume ratio and high surface energy, leads to a strong tendency for catalyst agglomeration. Consequently, it is urgent to look for new photocatalysts with improved performances.

6.3.2 Application of Metal Organic Frameworks (MOFs) for Pollutant Removal and Degradation The exploitation of new catalysts has been attracting great attention in the related research communities. In the past two decades, a class of newly developed inorganic–organic hybrid porous materials, namely, metal–organic frameworks (MOFs), has generated rapid development due to their versatile applications such as in catalysis and separation. Recent research has shown that these materials acting as catalysts are quite effective in photocatalytic degradation of organic pollutants.

In the past decade, MOFs of d-block transition metal have attracted intense interest. Some MOFs constructed by transition metals, such as Zn(II) , Cu(I)/Cu(II) , Cd(II) , Co(II)/Co(III) , and Fe(II)/Fe(III) , were examined as photocatalysts to degrade organic pollutants under UV, visible or UV–vis light. MOF-5 was first proposed to behave as a photocatalyst. The charge-separation state, with electrons in conduction band and holes in VB, made MOF-5 behave as an efficient photocatalyst. Furthermore, MOF-5 displayed a reverse shape selectivity toward different organic compounds, in which large phenolic molecules (2,6-di-*tert*-butylphenol) that cannot diffuse freely into the microspores of MOF-5 degraded significantly faster than the small ones (phenol) that can access the interior of MOF-5, as found by Garcia and coworkers [375, 376].

Compared with transition metal ions, lanthanide ions usually exhibit a high coordination number and diverse connectivity, which could facilitate the formation of various and unpredicted structures of MOFs. Lanthanide-based MOFs are very promising because organic linker could act as an antenna-producing efficient photosensitization. Chen and coworkers reported the use of two uranyl-based MOFs, $\text{Ag(2,2'-bpy)(UO}_2\text{)(1,4-bdc)}_{1.5}$ and $\text{Ag}_2(\text{phen})_2\text{UO}_2(\text{btec})$, both of which are water-insoluble and active (compared to nano-sized TiO_2 (P-25)), in photocatalytic degradation of rhodamine B (RhB) [377]. More importantly, $\text{Ag(2,2'-bpy)(UO}_2\text{)(1,4-bdc)}_{1.5}$ showed a remarkable photodegradation activity for RhB when a xenon lamp (wavelength longer than 400 nm) was used as the irradiation source.

In all, we believe that the MOFs are promising for use in wastewater treatment, and to this end, they could serve as an ideal choice for light harvesting to achieve the photocatalytic degradation of organic pollutants. The further development of these new photocatalysts will require a better understanding of photochemical mechanisms in MOF materials and the crucial structural parameters controlling their photocatalytic activity.

6.4 Conclusions

NPs are playing an increasing role in detecting and removing persistent and emerging environmental pollutants due to their unique size and physicochemical properties. Removal and degradation of pollutant can be easily achieved by the high adsorptivity, magnetic property, and catalytic activity of NPs. However, the results summarized in this chapter are mostly obtained at the laboratory scale, and practical challenges need to be overcome to fully realize the potential of NP-based methods in real life. At the same time, potential secondary contamination needs to be considered and prevented. Therefore, the toxicological effects of both NPs and NP-pollutant adducts need to be assessed.

REFERENCES

1. Rao, C.N.R., Kulkarni, G.U., Thomas, P.J., and Edwards, P.P. (2002) Size-dependent chemistry: properties of nanocrystals. *Chem. Eur. J.*, **8**, 28–35.
2. Nirmal, M., Dabbousi, B.O., Bawendi, M.G. *et al.* (1996) Fluorescence intermittency in single cadmium selenide nanocrystals. *Nature*, **383**, 802–804.
3. Ino, S. and Ogawa, S. (1967) Multiply twinned particles at earlier stages of gold film formation on alkali-halide crystals. *J. Phys. Soc. Jpn.*, **22**, 1365–1374.
4. Montejano-Carrizales, J.M., Iñiguez, M.P., and Alonso, J.A. (1994) Evolution of the structural stability of large Cu, Ni, Pd, and Ag clusters with size: an analysis within the embedded atom method. *J. Cluster Sci.*, **5**, 287–302.
5. Garcia-Rodeja, J., Rey, C., and Galleo, L.J. (1994) Molecular-dynamics study of the structures, binding energies, and melting of clusters of fcc transition and noble metals using the voter and Chen version of the embedded-atom model. *Phys. Rev. B*, **49**, 8495–8498.
6. Coombes, C.J. (1972) The melting of small particles of lead and indium. *J. Phys. F.*, **2**, 441–448.
7. Castro, T., Reifengerger, R., Choi, E., and Andres, R.P. (1990) Size-dependent melting temperature of individual nanometer-sized metallic clusters. *Phys. Rev. B*, **42**, 8548–8556.
8. Beck, R.D., St. John, P., Homer, M.L., and Whetten, R.L. (1991) Impact-induced cleaving and melting of alkali-halide nanocrystals. *Science*, **253**, 879–883.
9. Alivisatos, A.P. (1996) Perspectives on the physical chemistry of semiconductor nanocrystals. *J. Phys. Chem.*, **100**, 13226–13239.
10. Berry, C.R. (1952) Electron diffraction from small crystals. *Phys. Rev.*, **88**, 596–599.
11. Goldstein, A.N., Echer, C.M., and Alivisatos, A.P. (1992) Melting in semiconductor nanocrystals. *Science*, **256**, 1425–1427.
12. Lamber, R., Wetjen, S., and Jaeger, N.I. (1995) Size dependence of the lattice parameter of small palladium particles. *Phys. Rev. B*, **51**, 10968–10971.
13. Lu, H.M. and Jiang, Q. (2004) Size-dependent surface energies of nanocrystals. *J. Phys. Chem. B*, **108**, 5617–5619.
14. Medasani, B., Park, Y.H., and Vasiliev, I. (2007) Theoretical study of the surface energy, stress, and lattice contraction of silver nanoparticles. *Phys. Rev. B*, **75**, 235436.
15. Nanda, K.K., Kruis, F.E., and Fissan, H. (2003) Higher surface energy of free nanoparticles. *Phys. Rev. Lett.*, **91**, 106102.
16. Philippot, K. and Serp, P. (2013) Concepts in nanocatalysis, in *Nanomaterials in Catalysis*, 1st edn, Wiley, Weinheim, pp. 1–54.
17. van Santen, R.A. (2009) Complementary structure sensitive and insensitive catalytic relationships. *Acc. Chem. Res.*, **42**, 57–66.

18. Somorjai, G., Tao, F., and Park, J. (2008) The nanoscience revolution: merging of colloid science, catalysis and nanoelectronics. *Top. Catal.*, **47**, 1–14.
19. Henry, C.R. (1998) Surface studies of supported model catalysts. *Surf. Sci. Rep.*, **31**, 231–233.
20. Valden, M., Lai, X., and Goodman, D.W. (1998) Onset of catalytic activity of gold clusters on titania with the appearance of nonmetallic properties. *Science*, **281**, 1647–1650.
21. Chen, M.S. and Goodman, D.W. (2004) The structure of catalytically active gold on titania. *Science*, **306**, 252–255.
22. Grass, M.E., Zhang, Y.W., Butcher, D.R. *et al.* (2008) A reactive oxide overlayer on rhodium nanoparticles during CO oxidation and its size dependence studied by in situ ambient-pressure X-ray photoelectron spectroscopy. *Angew. Chem. Int. Ed.*, **47**, 8893–8896.
23. Bezemer, G.L., Bitter, J.H., Kuipers, H.P.C.E. *et al.* (2006) Cobalt particle size effects in the Fischer–Tropsch reaction studied with carbon nanofiber supported catalysts. *J. Am. Chem. Soc.*, **128**, 3956–3964.
24. Barbier, A., Tuel, A., Arcon, I. *et al.* (2001) Characterization and catalytic behavior of Co/SiO₂ catalysts: influence of dispersion in the Fischer–Tropsch reaction. *J. Catal.*, **200**, 106–116.
25. Spencer, N.D., Schoonmaker, R.C., and Somorjai, G.A. (1982) Iron single crystals as ammonia synthesis catalysts: effect of surface structure on catalyst activity. *J. Catal.*, **74**, 129–135.
26. Narayanan, R. and El-Sayed, M.A. (2004) Changing catalytic activity during colloidal platinum nanocatalysis due to shape changes: electron-transfer reaction. *J. Am. Chem. Soc.*, **126**, 7194–7195.
27. Mavrikakis, M., Stoltze, P., and Norskov, J.K. (2000) Making gold less noble. *Catal. Lett.*, **64**, 101–106.
28. Ruggiero, C. and Hollins, P. (1997) Interaction of CO molecules with the Au(332) surface. *Surf. Sci.*, **377**, 583–586.
29. Xie, X., Li, Y., Liu, Z.Q. *et al.* (2009) Low-temperature oxidation of CO catalysed by Co₃O₄ nanorods. *Nature*, **458**, 746–749.
30. Narayanan, R. and El-Sayed, M.A. (2004) Shape-dependent catalytic activity of platinum nanoparticles in colloidal solution. *Nano Lett.*, **4**, 1343–1348.
31. Toda, T., Igarashi, H., Uchida, H., and Watanabe, M. (1999) Enhancement of the electroreduction of oxygen on Pt alloys with Fe, Ni, and Co. *J. Electrochem. Soc.*, **146**, 3750–3756.
32. Xu, Y., Ruban, A.V., and Mavrikakis, M. (2004) Adsorption and dissociation of O₂ on Pt–Co and Pt–Fe alloys. *J. Am. Chem. Soc.*, **126**, 4717–4725.
33. Jacob, T., Muller, R.P., and Goddard, W.A. (2003) Chemisorption of atomic oxygen on Pt(111) from DFT studies of Pt-clusters. *J. Phys. Chem. B*, **107**, 9465–9476.
34. Hyman, M.P. and Medlin, J.W. (2007) Effects of electronic structure modifications on the adsorption of oxygen reduction reaction intermediates on model Pt(111)-alloy surfaces. *J. Phys. Chem. C*, **111**, 17052–17060.
35. Stamenkovic, V.R., Fowler, B., Mun, B.S. *et al.* (2007) Improved oxygen reduction activity on Pt₃Ni(111) via increased surface site availability. *Science*, **315**, 493–497.
36. Burda, C., Chen, X., Narayanan, R., and El-Sayed, M.A. (2005) Chemistry and properties of nanocrystals of different shapes. *Chem. Rev.*, **105**, 1025–1102.
37. Alivisatos, A.P. (1996) Semiconductor clusters, nanocrystals, and quantum dots. *Science*, **271**, 933–937.
38. Nirmal, M. and Brus, L. (1999) Luminescence photophysics in semiconductor nanocrystals. *Acc. Chem. Res.*, **32**, 407–414.
39. Chen, M. and Goodman, D.W. (2006) Catalytically active gold: from nanoparticles to ultrathin films. *Acc. Chem. Res.*, **39**, 739–746.

40. Haruta, M., Yamada, N., Kobayashi, T., and Iijima, S. (1989) Gold catalysts prepared by coprecipitation for low-temperature oxidation of hydrogen and of carbon monoxide. *J. Catal.*, **115**, 301–309.
41. Lai, X., St. Clair, T.P., Valden, M., and Goodman, D.W. (1998) Scanning tunneling microscopy studies of metal clusters supported on $\text{TiO}_2(110)$: morphology and electronic structure. *Progress Sur. Sci.*, **59**, 25–52.
42. Ricci, D., Bongiorno, A., Pacchioni, G., and Landman, U. (2006) Bonding trends and dimensionality crossover of gold nanoclusters on metal-supported MgO thin films. *Phys. Rev. Lett.*, **97**, 036106.
43. Lopez, N., Janssens, T.V.W., Clausen, B.S. *et al.* (2004) On the origin of the catalytic activity of gold nanoparticles for low-temperature CO oxidation. *J. Catal.*, **223**, 232–235.
44. Liu, Z.P. and Alavi, P.H.A. (2002) Catalytic role of gold in gold-based catalysts: a density functional theory study on the CO oxidation on gold. *J. Am. Chem. Soc.*, **124**, 14770–14779.
45. Carrettin, S., Concepcion, P., Corma, A. *et al.* (2004) Nanocrystalline CeO_2 increases the activity of Au for CO oxidation by two orders of magnitude. *Angew. Chem. Int. Ed.*, **43**, 2538–2540.
46. Grunwaldt, J.D., Maciejewski, M., Becker, O.S. *et al.* (1999) Comparative study of Au/TiO_2 and Au/ZrO_2 catalysts for low-temperature CO oxidation. *J. Catal.*, **186**, 458–469.
47. Ertl, G. (2001) Heterogeneous catalysis on the atomic scale. *Chem. Record*, **1**, 33–45.
48. Comotti, M., Li, W.C., Spliethoff, B., and Schüth, F. (2006) Support effect in high activity gold catalysts for CO oxidation. *J. Am. Chem. Soc.*, **128**, 917–924.
49. Schubert, M.M., Hackenberg, S., van Veen, A.C. *et al.* (2001) CO oxidation over supported gold catalysts—“inert” and “active” support materials and their role for the oxygen supply during reaction. *J. Catal.*, **197**, 113–122.
50. Herzing, A.A., Kiely, C.J., Carley, A.F. *et al.* (2008) Identification of active gold nanoclusters on iron oxide supports for CO oxidation. *Science*, **321**, 1331–1335.
51. Valden, M., Pak, S., Lai, X., and Goodman, D.W. (1998) Structure sensitivity of CO oxidation over model Au/TiO_2 catalysts. *Catal. Lett.*, **56**, 7–10.
52. Remediakis, I.N., Lopez, N., and Norskov, J.K. (2005) CO oxidation on gold nanoparticles: theoretical studies. *Appl. Catal. A*, **291**, 13–20.
53. Lemire, C., Meyer, R., Shaikhutdinov, S.K., and Freund, H.J. (2004) CO adsorption on oxide supported gold: from small clusters to monolayer islands and three-dimensional nanoparticles. *Surf. Sci.*, **552**, 27–34.
54. Overbury, S.H., Schwatz, V., Mullins, D.R. *et al.* (2006) Evaluation of the Au size effect: CO oxidation catalyzed by Au/TiO_2 . *J. Catal.*, **241**, 56–65.
55. Janssens, T.V.W., Carlsson, A., Puig-Molina, A., and Clausen, B.S. (2006) Relation between nanoscale Au particle structure and activity for CO oxidation on supported gold catalysts. *J. Catal.*, **240**, 108–113.
56. Lopez, N. and Norskov, J.K. (2002) Catalytic CO oxidation by a gold nanoparticle: a density functional study. *J. Am. Chem. Soc.*, **124**, 11262–11263.
57. Wahlstrom, E., Lopez, N., Schaub, R. *et al.* (2003) Bonding of gold nanoclusters to oxygen vacancies on rutile $\text{TiO}_2(110)$. *Phys. Rev. Lett.*, **90**, 026101.
58. Min, B.K., Wallace, W.T., and Goodman, D.W. (2006) Support effects on the nucleation, growth, and morphology of gold nano-clusters. *Surf. Sci.*, **600**, L7–L11.
59. Min, B.K., Wallace, W.T., and Goodman, D.W. (2004) Synthesis of a sinter-resistant, mixed-oxide support for Au nanoclusters. *J. Phys. Chem. B*, **108**, 14609–14615.
60. Min, B.K., Wallace, W.T., Santra, A.K., and Goodman, D.W. (2004) Role of defects in the nucleation and growth of Au nanoclusters on SiO_2 thin films. *J. Phys. Chem. B*, **108**, 16339–16343.
61. Santra, A.K., Kolmakov, A., Yang, F., and Goodman, D.W. (2003) Growth of Au on $\text{TiO}_2(110)$ on a cluster-by-cluster basis. *Jpn. J. Appl. Phys.*, **42**, 4795–4797.

62. Haruta, M. (1997) Size- and support-dependency in the catalysis of gold. *Catal. Today*, **36**, 153–166.
63. Schubert, M.M., Kahlich, M.J., Gasteiger, H.A., and Behm, R.J. (1999) Correlation between CO surface coverage and selectivity/kinetics for the preferential CO oxidation over Pt/ γ -Al₂O₃ and Au/ α -Fe₂O₃: an in-situ DRIFTS study. *J. Power Sources*, **84**, 175–182.
64. Liu, H.C., Kozlov, A.I., Kozlova, A.P. *et al.* (1999) Active oxygen species and mechanism for low-temperature CO oxidation reaction on a TiO₂-supported Au catalyst prepared from Au(PPh₃)(NO₃) and as-precipitated titanium hydroxide. *J. Catal.*, **185**, 252–264.
65. Molina, L.M., Rasmussen, M.D., and Hammer, B. (2004) Adsorption of O₂ and oxidation of CO at Au nanoparticles supported by TiO₂(110). *J. Chem. Phys.*, **120**, 7673–7680.
66. Molina, L.M. and Hammer, B. (2005) Some recent theoretical advances in the understanding of the catalytic activity of Au. *Appl. Catal. A*, **291**, 21–31.
67. Remediakis, I.N., Lopez, N., and Norskov, J.K. (2005) CO oxidation on rutile-supported Au nanoparticles. *Angew. Chem. Int. Ed.*, **44**, 1824–1826.
68. Molina, L.M. and Hammer, B. (2003) Active role of oxide support during CO oxidation at Au/MgO. *Phys. Rev. Lett.*, **90**, 206102.
69. Liu, Z.P., Gong, X.Q., Kohanoff, J. *et al.* (2003) Catalytic role of metal oxides in gold-based catalysts: a first principles study of CO oxidation on TiO₂ supported Au. *Phys. Rev. Lett.*, **91**, 266102.
70. Liu, X., Liu, M.H., Luo, Y.C. *et al.* (2012) Strong metal-support interactions between gold nanoparticles and ZnO nanorods in CO oxidation. *J. Am. Chem. Soc.*, **134**, 10251–10258.
71. Chen, M. and Goodman, D.W. (2008) Catalytically active gold on ordered titania supports. *Chem. Soc. Rev.*, **37**, 1860–1870.
72. Fierro-Gonzalez, J.C. and Gates, B.C. (2008) Catalysis by gold dispersed on supports: the importance of cationic gold. *Chem. Soc. Rev.*, **37**, 2127–2134.
73. Fujitani, T. and Nakamura, I. (2011) Mechanism and active sites of the oxidation of CO over Au/TiO₂. *Angew. Chem. Int. Ed.*, **50**, 10144–10147.
74. Matthey, D., Wang, J.G., Wendt, S. *et al.* (2007) Enhanced bonding of gold nanoparticles on oxidized TiO₂(110). *Science*, **315**, 1692–1696.
75. Shang, C. and Liu, Z.P. (2011) Origin and activity of gold nanoparticles as aerobic oxidation catalysts in aqueous solution. *J. Am. Chem. Soc.*, **133**, 9938–9947.
76. Parker, S.C., Grant, A.W., Bondzie, V.A., and Campbell, C.T. (1999) A synchrotron study of the growth of vanadium oxide on Al₂O₃(0001). *Surf. Sci.*, **441**, 1–9.
77. Guzman, J. and Gates, B.C. (2004) Catalysis by supported gold: correlation between catalytic activity for CO oxidation and oxidation states of gold. *J. Am. Chem. Soc.*, **126**, 2672–2673.
78. Guzman, J. and Gates, B.C. (2003) Oxidation states of gold in MgO-supported complexes and clusters: characterization by X-ray absorption spectroscopy and temperature-programmed oxidation and reduction. *J. Phys. Chem. B*, **107**, 2242–2248.
79. Yoon, B., Hakkinen, H., Landman, U. *et al.* (2005) Charging effects on bonding and catalyzed oxidation of CO on Au₈ clusters on MgO. *Science*, **307**, 403–407.
80. Sanchez, A., Abbet, S., Heiz, U. *et al.* (1999) When gold is not noble: nanoscale gold catalysts. *J. Phys. Chem. A*, **103**, 9573–9578.
81. Goodman, D.W. (2005) “Catalytically active Au on titania:” yet another example of a strong metal support interaction (SMSI)? *Catal. Lett.*, **99**, 1–4.
82. Hughes, M.D., Xu, Y.J., Jenkins, P. *et al.* (2005) Tunable gold catalysts for selective hydrocarbon oxidation under mild conditions. *Nature*, **437**, 1132–1135.
83. Dapurkar, S.E., Shervani, Z., Yokoyama, T. *et al.* (2009) Supported gold nanoparticles catalysts for solvent-free selective oxidation of benzylic compounds into ketones at 1 atm O₂. *Catal. Lett.*, **130**, 42–47.

84. Kesavan, L., Tiruvalam, R., and Ab Rahim, M.H. *et al.* (2011) Solvent-free oxidation of primary carbon-hydrogen bonds in toluene using Au-Pd alloy nanoparticles. *Science*, **331**, 195–199.
85. Hayashi, T., Tanaka, K., and Haruta, M. (1998) Selective vapor-phase epoxidation of propylene over Au/TiO₂ catalysts in the presence of oxygen and hydrogen. *J. Catal.*, **178**, 566–575.
86. Abad, A., Almela, C., Corma, A., and Garcia, H. (2006) Unique gold chemoselectivity for the aerobic oxidation of allylic alcohols. *Chem. Commun.*, 3178–3180.
87. Jørgensen, B., Egholmchristiansen, S., Dahlthomsen, M., and Christensen, C. (2007) Aerobic oxidation of aqueous ethanol using heterogeneous gold catalysts: efficient routes to acetic acid and ethyl acetate. *J. Catal.*, **251**, 332–337.
88. Raptis, C., Garcia, H., and Stratakis, M. (2009) Selective isomerization of epoxides to allylic alcohols catalyzed by TiO₂-supported gold nanoparticles. *Angew. Chem. Int. Ed.*, **48**, 3133–3136.
89. Taylor, S.F.R., Sa, J., and Hardacre, C. (2011) Friedel–Crafts alkylation of aromatics with benzyl alcohol over gold-modified silica. *ChemCatChem*, **3**, 119–121.
90. Hashmi, A.S.K. and Hutchings, G.J. (2006) Gold catalysis. *Angew. Chem. Int. Ed.*, **45**, 7896–7936.
91. Bond, G.C., Sermon, P.A., Webb, G. *et al.* (1973) Hydrogenation over supported gold catalysts. *J. Chem. Soc. Chem. Commun.*, (13), 444–445.
92. Zhang, X., Shi, H., and Xu, B.-Q. (2005) Catalysis by gold: isolated surface Au³⁺ ions are active sites for selective hydrogenation of 1,3-butadiene over Au/ZrO₂[−] catalysts. *Angew. Chem. Int. Ed.*, **44**, 7132–7135.
93. Corma, A. and Serna, P. (2006) Chemoselective hydrogenation of nitro compounds with supported gold catalysts. *Science*, **313**, 332–334.
94. Gaffet, E., Tachikart, M., El Kedim, O., and Rahouadj, R. (1996) Nanostructural materials formation by mechanical alloying: morphologic analysis based on transmission and scanning electron microscopic observations. *Mater Charact*, **36**, 185–190.
95. Izotov, V.I., Filippov, G.A., and Edneral, A.F. (1998) Effect of chemical composition on the structure and properties of low-alloy steel after the low-temperature ‘normal’ transformation. *Fiz. Met. Metalloved.*, **85**, 111–121.
96. Pachón, L.D. and Rothenberg, G. (2008) Transition-metal nanoparticles: synthesis, stability and the leaching issue. *Appl. Organomet. Chem.*, **22**, 288–299.
97. Turkevich, J., Stevenson, P.C., and Hillier, J. (1951) A study of the nucleation and growth processes in the synthesis of colloidal gold. *Diss. Fara. Soc.*, **11**, 55–75.
98. Turkevich, J. and Kim, G. (1970) Palladium: preparation and catalytic properties of particles of uniform size. *Science*, **169**, 873–879.
99. Turkevich, J. (1985) Colloidal gold. part I. *Gold Bull.*, **18**, 86–91.
100. Leisner, T., Rosche, C., Wolf, S. *et al.* (1996) The catalytic role of small coinage-metal clusters in photography. *Surf. Rev. Lett.*, **3**, 1105–1108.
101. Brust, M., Walker, M., Bethell, D. *et al.* (1994) Synthesis of thiol-derivatised gold nanoparticles in a two-phase liquid–liquid system. *J. Chem. Soc. Chem. Commun.*, (7), 801–802.
102. Funston, A.M., Mulvaney, P., and Murray, R.W. (2009) Gold nanoparticles: past, present, and future. *Langmuir*, **25**, 13840–13851.
103. Goulet, P.J.G. and Lennox, R.B. (2010) New insights into Brust–Schiffrin metal nanoparticle synthesis. *J. Am. Chem. Soc.*, **132**, 9582–9584.
104. Tracy, J.B., Kalyuzhny, G., Crowe, M.C. *et al.* (2007) Poly(ethylene glycol) ligands for high-resolution nanoparticle mass spectrometry. *J. Am. Chem. Soc.*, **129**, 6706–6707.
105. Yang, Y.Y. and Chen, S.W. (2003) Surface manipulation of the electronic energy of subnanometer-sized gold clusters: an electrochemical and spectroscopic investigation. *Nano Lett.*, **3**, 75–79.

106. Song, Y., Harper, A.S., and Murray, R.W. (2005) Ligand heterogeneity on monolayer-protected gold clusters. *Langmuir*, **21**, 5492–5550.
107. Castro, E.G., Salvatierra, R.V., Schreiner, W.H. *et al.* (2010) Dodecanethiol-stabilized platinum nanoparticles obtained by a two-phase method: synthesis, characterization, mechanism of formation, and electrocatalytic properties. *Chem. Mater.*, **22**, 360–370.
108. Wu, Z.K., Lanni, E., Chen, W.Q. *et al.* (2009) High yield, large scale synthesis of thiolate-protected Ag₇ clusters. *J. Am. Chem. Soc.*, **131**, 16672–16674.
109. Ang, T.P., Wee, T.S.A., and Chin, W.S. (2004) Three-dimensional self-assembled monolayer (3D SAM) of n-alkanethiols on copper nanoclusters. *J. Phys. Chem. B*, **108**, 11001–11010.
110. Lu, Y.Z. and Chen, W. (2012) Sub-nanometre sized metal clusters: from synthetic challenges to the unique property discoveries. *Chem. Soc. Rev.*, **41**, 3594–3623.
111. Shang, L., Dörlich, R.M., Brandholt, S. *et al.* (2011) Facile preparation of water-soluble fluorescent gold nanoclusters for cellular imaging applications. *Nanoscale*, **3**, 2009–2014.
112. Negishi, Y., Murayama, H., and Tsukuda, T. (2002) Formation of Pd_n(SR)_m clusters (n<60) in the reactions of PdCl₂ and RSH (R=n-C₁₈H₃₇, n-C₁₂H₂₅). *Chem. Phys. Lett.*, **366**, 561–566.
113. Hoppe, M.L.C.E., Pardiñas-Blanco, I., and López-Quintela, M.A. (2006) One-step synthesis of gold and silver hydrosols using poly(N-vinyl-2-pyrrolidone) as a reducing agent. *Langmuir*, **22**, 7027–7034.
114. Washio, I., Xiong, Y., Yin, Y., and Xia, Y. (2006) Reduction by the end groups of poly(vinyl pyrrolidone): a new and versatile route to the kinetically controlled synthesis of Ag triangular nanoplates. *Adv. Mater.*, **18**, 1745–1749.
115. Andres, R.P., Bielefeld, J.-D., Henderson, J.-I. *et al.* (1996) Self-assembly of a two-dimensional superlattice of molecularly linked metal clusters. *Science*, **273**, 1690–1693.
116. Ley, S.V., Mitchell, C., Pears, D. *et al.* (2003) Recyclable polyurea-microencapsulated Pd(0) nanoparticles: an efficient catalyst for hydrogenolysis of epoxides. *Org. Lett.*, **5**, 4665–4668.
117. Demir, M.M., Gulgun, M.A., Menciloglu, Y.Z. *et al.* (2004) Palladium nanoparticles by electrospinning from poly(acrylonitrile-co-acrylic acid)–PdCl₂ solutions. Relations between preparation conditions, particle size, and catalytic activity. *Macromolecules*, **37**, 1787–1792.
118. Chauhan, B.P.S., Rathore, J.S., and Bando, T. (2004) “Polysiloxane-Pd” nanocomposites as recyclable chemoselective hydrogenation catalysts. *J. Am. Chem. Soc.*, **126**, 8493–8500.
119. Yang, C.C., Wan, C.C., and Wang, Y.Y. (2004) Synthesis of Ag/Pd nanoparticles via reactive micelles as templates and its application to electroless copper deposition. *J. Colloid Interface Sci.*, **279**, 433–439.
120. Widegren, J.A. and Finke, R.G. (2003) A review of soluble transition-metal nanoclusters as arene hydrogenation catalysts. *J. Mol. Catal. A*, **191**, 187–207.
121. Mu, X., Evans, D.G., and Kou, Y. (2004) A general method for preparation of PVP-stabilized noble metal nanoparticles in room temperature ionic liquids. *Catal. Lett.*, **97**, 151–154.
122. Mu, X., Meng, J., Li, Z., and Kou, Y. (2005) Rhodium nanoparticles stabilized by ionic copolymers in ionic liquids: long lifetime nanocluster catalysts for benzene hydrogenation. *J. Am. Chem. Soc.*, **127**, 9694–9695.
123. Sinfelt, J.H. (1977) Catalysis by alloys and bimetallic clusters. *Acc. Chem. Res.*, **10**, 15–20.
124. He, J.-H., Ichinose, I., Kunitake, T. *et al.* (2003) Facile fabrication of Ag–Pd bimetallic nanoparticles in ultrathin TiO₂-gel films: nanoparticle morphology and catalytic activity. *J. Am. Chem. Soc.*, **125**, 11034–11040.
125. Tomalia, D.A., Baker, H., Dewald, J. *et al.* (1985) A new class of polymers: starburst-dendritic macromolecules. *Polym. J.*, **17**, 117–132.
126. Hecht, S. and Fréchet, J.M. (2001) Dendritic encapsulation of function: applying nature’s site isolation principle from biomimetics to materials science. *Angew. Chem. Int. Ed.*, **40**, 74–91.

127. Buhleier, E., Wehner, W., and Vögtle, F. (1978) "Cascade"- and "nonskid-chain-like" syntheses of molecular cavity topologies. *Synthesis*, **1978**, 155–158.
128. Crooks, R.M., Zhao, M., Sun, L. *et al.* (2001) Dendrimer-encapsulated metal nanoparticles: synthesis, characterization, and applications to catalysis. *Acc. Chem. Res.*, **34**, 181–190.
129. Scott, R.W.J., Wilson, O.M., and Crooks, R.M. (2005) Synthesis, characterization, and applications of dendrimer-encapsulated nanoparticles. *J. Phys. Chem. B*, **109**, 692–704.
130. Myers, V.S., Weir, M.G., Carino, E.V. *et al.* (2011) Dendrimer-encapsulated nanoparticles: new synthetic and characterization methods and catalytic applications. *Chem. Sci.*, **2**, 1632–1646.
131. Anderson, R.M., Zhang, L., Loussaert, J.A. *et al.* (2013) An experimental and theoretical investigation of the inversion of Pd@Pt core@shell dendrimer-encapsulated nanoparticles. *ACS Nano*, **7**, 9345–9353.
132. Nasar, K., Fache, F., Lemaire, M. *et al.* (1994) Stereoselective reduction of disubstituted aromatics on colloidal rhodium. *J. Mol. Catal.*, **87**, 107–115.
133. Ozkar, S. and Finke, R.G. (2002) Nanocluster formation and stabilization fundamental studies: ranking commonly employed anionic stabilizers via the development, then application, of five comparative criteria. *J. Am. Chem. Soc.*, **124**, 5796–5810.
134. Strimbu, L., Liu, J., and Kaifer, A.E. (2003) Cyclodextrin-capped palladium nanoparticles as catalysts for the Suzuki reaction. *Langmuir*, **19**, 483–485.
135. Templeton, A.C., Wuelfing, W.P., and Whyman, R. (2000) Monolayer-protected cluster molecules. *Acc. Chem. Res.*, **33**, 27–36.
136. Daniel, M.-C. and Astruc, D. (2004) Gold nanoparticles: assembly, supramolecular chemistry, quantum-size-related properties, and applications toward biology, catalysis, and nanotechnology. *Chem. Rev.*, **104**, 293–346.
137. Ananikov, V.P., Orlov, N.V., Beletskaya, I.P. *et al.* (2007) New approach for size- and shape-controlled preparation of Pd nanoparticles with organic ligands synthesis and application in catalysis. *J. Am. Chem. Soc.*, **129**, 7252–7253.
138. Mirkhalaf, F., Paprotny, J., and Schiffrin, D.J. (2006) Synthesis of metal nanoparticles stabilized by metal–carbon bonds. *J. Am. Chem. Soc.*, **128**, 7400–7401.
139. Son, S.U., Jang, Y., Park, J. *et al.* (2004) Designed synthesis of atom-economical Pd/Ni bimetallic nanoparticle-based catalysts for sonogashira coupling reactions. *J. Am. Chem. Soc.*, **126**, 5026–5027.
140. Fonseca, G.S., Umpierre, A.P., Fichtner, P.F.P. *et al.* (2003) The use of imidazolium ionic liquids for the formation and stabilization of Ir⁰ and Rh⁰ nanoparticles: efficient catalysts for the hydrogenation of arenes. *Chem. Eur. J.*, **9**, 3263–3269.
141. Dupont, J. and Scholten, J.D. (2010) On the structural and surface properties of transition-metal nanoparticles in ionic liquids. *Chem. Soc. Rev.*, **39**, 1780–1804.
142. Schmid, G., Harms, M., Malm, J.O. *et al.* (1993) Ligand-stabilized giant palladium clusters: promising candidates in heterogeneous catalysis. *J. Am. Chem. Soc.*, **115**, 2046–2048.
143. Schmid, G. (1992) Large clusters and colloids. Metals in the embryonic state. *Chem. Rev.*, **92**, 1709–1727.
144. Leger, B., Denicourt-Nowicki, A., Olivier-Bourbigou, H., and Roucoux, A. (2008) Rhodium nanocatalysts stabilized by various bipyridine ligands in nonaqueous ionic liquids: influence of the bipyridine coordination modes in arene catalytic hydrogenation. *Inorg. Chem.*, **47**, 9090–9096.
145. Leger, B., Denicourt-Nowicki, A., Roucoux, A., and Olivier-Bourbigou, H. (2008) Synthesis of bipyridine-stabilized rhodium nanoparticles in non-aqueous ionic liquids: a new efficient approach for arene hydrogenation with nanocatalysts. *Adv. Synth. Catal.*, **350**, 153–159.
146. Zhao, D.B., Fei, Z.F., Geldbach, T.J. *et al.* (2004) Nitrile-functionalized pyridinium ionic liquids: synthesis, characterization, and their application in carbon–carbon coupling reactions. *J. Am. Chem. Soc.*, **126**, 15876–15882.

147. Bronstein, L.M. and Shifrina, Z.B. (2011) Dendrimers as encapsulating, stabilizing, or directing agents for inorganic nanoparticles. *Chem. Rev.*, **111**, 5301–5344.
148. Shen, Z., Duan, H.W., and Frey, H. (2007) Water-soluble fluorescent Ag nanoclusters obtained from multiarm star poly(acrylic acid) as “molecular hydrogel” templates. *Adv. Mater.*, **19**, 349–352.
149. Shang, L. and Dong, S.J. (2008) Facile preparation of water-soluble fluorescent silver nanoclusters using a polyelectrolyte template. *Chem. Commun.*, 1088–1090.
150. Xie, J.P., Zheng, Y.G., and Ying, J.Y. (2009) Protein-directed synthesis of highly fluorescent gold nanoclusters. *J. Am. Chem. Soc.*, **131**, 888–889.
151. Zheng, J., Petty, J.T., and Dickson, R.M. (2003) High quantum yield blue emission from water-soluble Au₈ nanodots. *J. Am. Chem. Soc.*, **125**, 7780–7781.
152. Richards, C.I., Choi, S., Hsiang, J.C. *et al.* (2008) Oligonucleotide-stabilized Ag nanocluster fluorophores. *J. Am. Chem. Soc.*, **130**, 5038–5039.
153. Zhao, M.Q., Sun, L., and Crooks, R.M. (1998) Preparation of Cu nanoclusters within dendrimer templates. *J. Am. Chem. Soc.*, **120**, 4877–4878.
154. Balogh, L. and Tomalia, D.A. (1998) Poly(amidoamine) dendrimer-templated nanocomposites: 1. Synthesis of zero-valent copper nanoclusters. *J. Am. Chem. Soc.*, **120**, 7355–7356.
155. Yamamoto, K., Imaoka, T., Chun, W.J. *et al.* (2009) Size-specific catalytic activity of platinum clusters enhances oxygen reduction reactions. *Nat. Chem.*, **1**, 397–402.
156. Curtis, A., Duff, D., Edwards, P. *et al.* (1988) Preparation and structural characterization of an unprotected copper sol. *Phys. Chem.*, **92**, 2270–2275.
157. Wang, Y., Ren, J.W., Deng, K. *et al.* (2000) Preparation of tractable platinum, rhodium, and ruthenium nanoclusters with small particle size in organic media. *Chem. Mater.*, **12**, 1622–1627.
158. Luque, R., Budarin, V., Clark, J.H., and Macquarrie, D.J. (2008) Glycerol transformations on polysaccharide derived mesoporous materials. *Appl. Catal. B*, **82**, 157–162.
159. Budarin, V., Clark, J.H., Hardy, J.J.E. *et al.* (2006) Starbons: new starch-derived mesoporous carbonaceous materials with tunable properties. *Angew. Chem. Int. Ed.*, **45**, 3782–3786.
160. Panziera, N., Pertici, P., Barazzone, L. *et al.* (2007) MVS-derived palladium nanoparticles deposited on polydimethylphosphazene as recyclable catalysts for Heck-type reactions: preparation, structural study, and catalytic activity. *J. Catal.*, **246**, 351–361.
161. Astruc, D., Lu, F., and Aranzaes, J.R. (2005) Nanoparticles as recyclable catalysts: the frontier between homogeneous and heterogeneous catalysis. *Angew. Chem. Int. Ed.*, **44**, 7852–7872.
162. Budarin, V., Clark, J.H., Luque, R. *et al.* (2008) Palladium nanoparticles on polysaccharide-derived mesoporous materials and their catalytic performance in C–C coupling reactions. *Green Chem.*, **10**, 382–387.
163. Magano, J. and Dunetz, J.R. (2011) Large-scale applications of transition metal-catalyzed couplings for the synthesis of pharmaceuticals. *Chem. Rev.*, **111**, 2177–2250.
164. Fihri, A., Bouhrara, M., Nekoueishahraki, B. *et al.* (2011) Nanocatalysts for Suzuki cross-coupling reactions. *Chem. Soc. Rev.*, **40**, 5181–5203.
165. Sambiagio, C., Marsden, S.P., John Blacker, A., and McGowan, P.C. (2014) Copper catalysed Ullmann type chemistry: from mechanistic aspects to modern development. *Chem. Soc. Rev.*, **43**, 3525–3550.
166. Cao, M., Wei, Y., Gao, S., and Cao, R. (2012) Synthesis of palladium nanocatalysts with cucurbit[n]uril as both a protecting agent and a support for Suzuki and Heck reactions. *Catal. Sci. Technol.*, **2**, 156–163.
167. Veisi, H., Khazaei, A., Safaei, M., and Kordestani, D. (2014) Synthesis of biguanide-functionalized single-walled carbon nanotubes (SWCNTs) hybrid materials to immobilized palladium as new recyclable heterogeneous nanocatalyst for Suzuki–Miyaura coupling. *J. Mol. Catal. A*, **382**, 106–113.

168. Monopoli, A., Nacci, A., Calò, V. *et al.* (2010) Palladium/zirconium oxide nanocomposite as a highly recyclable catalyst for C-C coupling reactions in water. *Molecules*, **15**, 4511–4525.
169. Peral, D., Gomez-Villarraga, F., Sala, X. *et al.* (2013) Palladium catalytic systems with hybrid pyrazole ligands in C–C coupling reactions. Nanoparticles versus molecular complexes. *Catal. Sci. Technol.*, **3**, 475–489.
170. Sá, S., Gawande, M.B., Velhinho, A. *et al.* (2014) Magnetically recyclable magnetite–palladium (nanocat-Fe–Pd) nanocatalyst for the Buchwald–Hartwig reaction. *Green Chem.*, **16**, 3494–3500.
171. Tobisu, M., Nakamura, K., and Chatani, N. (2014) Nickel-catalyzed reductive and borylative cleavage of aromatic carbon–nitrogen bonds in N-aryl amides and carbamates. *J. Am. Chem. Soc.*, **136**, 5587–5590.
172. Xu, G., Li, Q., Feng, J. *et al.* (2014) Direct α -alkylation of ketones with alcohols in water. *ChemSusChem*, **7**, 105–109.
173. Sharma, R.K., Monga, Y., Puri, A., and Gaba, G. (2013) Magnetite (Fe₃O₄) silica based organic–inorganic hybrid copper(II) nanocatalyst: a platform for aerobic N-alkylation of amines. *Green Chem.*, **15**, 2800–2809.
174. Guerrero, M., Costa, N.J.S., Vono, L.L.R. *et al.* (2013) Taking advantage of a terpyridine ligand for the deposition of Pd nanoparticles onto a magnetic material for selective hydrogenation reactions. *J. Mater. Chem. A*, **1**, 1441–1449.
175. Liu, Y., Luo, C., and Liu, H.C. (2012) Tungsten trioxide promoted selective conversion of cellulose into propylene glycol and ethylene glycol on a ruthenium catalyst. *Angew. Chem. Int. Ed.*, **51**, 3249–3253.
176. Jagadeesh, R.V., Surkus, A.E., Junge, H. *et al.* (2013) Nanoscale Fe₂O₃-based catalysts for selective hydrogenation of nitroarenes to anilines. *Science*, **342**, 1073–1076.
177. Westerhaus, F.A., Jagadeesh, R.V., Wienhofer, G. *et al.* (2013) Heterogenized cobalt oxide catalysts for nitroarene reduction by pyrolysis of molecularly defined complexes. *Nat. Chem.*, **5**, 537–543.
178. Wang, T., Xiao, C., Yan, L. *et al.* (2007) Aqueous-phase aerobic oxidation of alcohols by soluble Pt nanoclusters in the absence of base. *Chem. Commun.*, 4375–4377.
179. Wang, T., Shou, H., Kou, Y., and Liu, H. (2009) Base-free aqueous-phase oxidation of non-activated alcohols with molecular oxygen on soluble Pt nanoparticles. *Green Chem.*, **11**, 562–568.
180. Zhang, Q., Deng, W., and Wang, Y. (2011) Effect of size of catalytically active phases in the dehydrogenation of alcohols and the challenging selective oxidation of hydrocarbons. *Chem. Commun.*, **47**, 9275–9292.
181. Xie, J., Nie, J., and Liu, H. (2014) Aqueous phase selective aerobic oxidation of 5-hydroxymethylfurfural on Ru/C in the presence of base. *Chin. J. Catal.*, **35**, 937–944.
182. Nie, J., Xie, J., and Liu, H. (2013) Efficient aerobic oxidation of 5-hydroxymethylfurfural to 2,5-diformylfuran on supported Ru catalysts. *J. Catal.*, **301**, 83–91.
183. Guan, Y. and Hensen, E.J.M. (2009) Ethanol dehydrogenation by gold catalysts: the effect of the gold particle size and the presence of oxygen. *App. Catal. A*, **361**, 49–56.
184. Hemalatha, K., Madhumitha, G., Kajbafvala, A. *et al.* (2013) Function of nanocatalyst in chemistry of organic compounds revolution: an overview. *J. Nanomater.*, **2013**, Article ID 341015.
185. Chng, L.L., Erathodiyil, N., and Ying, J.Y. (2013) Nanostructured catalysts for organic transformations. *Acc. Chem. Res.*, **46**, 1825–1837.
186. Steynberg, A.P. (2004) Chapter 1-introduction to Fischer-Tropsch technology. *Stud. Surf. Sci. Catal.*, **152**, 1–63.
187. Khodakov, A.Y., Chu, W., and Fongarland, P. (2007) Advances in the development of novel cobalt Fischer-Tropsch catalysts for synthesis of long-chain hydrocarbons and clean fuels. *Chem. Rev.*, **107**, 1692–1744.

188. de Smit, E. and Weckhuysen, B.M. (2008) The renaissance of iron-based Fischer-Tropsch synthesis on the multifaceted catalyst deactivation behaviour. *Chem. Soc. Rev.*, **37**, 2758.
189. Iglesia, E. (1997) Design, synthesis, and use of cobalt-based Fischer-Tropsch synthesis catalysts. *Appl. Catal. A*, **161**, 59–78.
190. Rofer-DePoorter, C.K. (1981) A comprehensive mechanism for the Fischer-Tropsch synthesis. *Chem. Rev.*, **81**, 447–474.
191. Bell, A.T. (1981) Catalytic synthesis of hydrocarbons over group VIII metals. A discussion of the reaction mechanism. *Catal. Rev. Sci. Eng.*, **23**, 203–232.
192. Maitlis, P.M. and Zanotti, V. (2009) The role of electrophilic species in the Fischer–Tropsch reaction. *Chem. Commun.*, 1619–1634.
193. Inderwildi, O.R., Jenkins, S.J., and King, D.A. (2008) Fischer–Tropsch mechanism revisited: alternative pathways for the production of higher hydrocarbons from synthesis gas. *J. Phys. Chem. C*, **112**, 1305–1307.
194. Shetty, S., Jansen, A.P.J., and van Santen, R.A. (2009) Direct versus hydrogen-assisted CO dissociation. *J. Am. Chem. Soc.*, **131**, 12874–12875.
195. Brady, R.C. III and Pettit, R. (1980) Reactions of diazomethane on transition-metal surfaces and their relationship to the mechanism of the Fischer-Tropsch reaction. *J. Am. Chem. Soc.*, **102**, 6181–6182.
196. Ciobca, I.M., Kramer, G.J., Ge, Q. *et al.* (2002) Mechanisms for chain growth in Fischer–Tropsch synthesis over Ru(0001). *J. Catal.*, **212**, 136–144.
197. Liu, Z.P. and Hu, P. (2002) A new insight into Fischer–Tropsch synthesis. *J. Am. Chem. Soc.*, **124**, 11568–11569.
198. Friedel, R.A. and Anderson, R.B. (1950) Composition of synthetic liquid fuels. I. Product distribution and analysis of C5–C8 paraffin isomers from cobalt catalyst. *J. Am. Chem. Soc.*, **72**, 1212–1215.
199. Galvis, H.M.T., Bitter, J.H., Khare, C.B. *et al.* (2012) Supported iron nanoparticles as catalysts for sustainable production of lower olefins. *Science*, **335**, 835–838.
200. Galvis, H.M.T., Bitter, J.H., Davidian, T. *et al.* (2012) Iron particle size effects for direct production of lower olefins from synthesis gas. *J. Am. Chem. Soc.*, **134**, 16207–16215.
201. Chu, W., Chernavskii, P.A., Gengembre, L. *et al.* (2007) Cobalt species in promoted cobalt alumina-supported Fischer–Tropsch catalysts. *J. Catal.*, **252**, 215–230.
202. Riedel, T., Schulz, H., Schaub, G. *et al.* (2003) Fischer–Tropsch on iron with H₂/CO and H₂/CO₂ as synthesis gases: the episodes of formation of the Fischer–Tropsch regime and construction of the catalyst. *Top. Catal.*, **26**, 41–54.
203. de Smit, E., Swart, I., Creemer, J.F. *et al.* (2008) Nanoscale chemical imaging of a working catalyst by scanning transmission X-ray microscopy. *Nature*, **456**, 222–225.
204. Wang, H., Zhou, W., Liu, J. *et al.* (2013) Platinum-modulated cobalt nanocatalysts for low-temperature aqueous-phase Fischer–Tropsch synthesis. *J. Am. Chem. Soc.*, **135**, 4149–4158.
205. Chen, W., Fan, Z., Pan, X., and Bao, X. (2008) Effect of confinement in carbon nanotubes on the activity of Fischer–Tropsch iron catalyst. *J. Am. Chem. Soc.*, **130**, 9414–9419.
206. Bezemer, G.L., Falke, U., van Dillen, A.J., and de Jong, K.P. (2005) Cobalt on carbon nanofiber catalysts: auspicious system for study of manganese promotion in Fischer–Tropsch catalysis. *Chem. Commun.*, 731–733.
207. Bezemer, G.L., Radstake, P.B., Falke, U. *et al.* (2006) Investigation of promoter effects of manganese oxide on carbon nanofiber-supported cobalt catalysts for Fischer–Tropsch synthesis. *J. Catal.*, **237**, 152–161.
208. Botes, F.G. (2005) The effect of a higher operating temperature on the Fischer–Tropsch/HZSM-5 bifunctional process. *Appl. Catal. A*, **284**, 21–29.

209. Bao, J., He, J., Zhang, Y. *et al.* (2008) A core/shell catalyst produces a spatially confined effect and shape selectivity in a consecutive reaction. *Angew. Chem. Int. Ed.*, **47**, 353–362.
210. Zhang, H., Lancelot, C., Chu, W. *et al.* (2009) The nature of cobalt species in carbon nanotubes and their catalytic performance in Fischer–Tropsch reaction. *J. Mater. Chem.*, **19**, 9241–9249.
211. Lohitharn, N., Goodwin, J.G. Jr., and Lotero, E. (2008) Fe-based Fischer–Tropsch synthesis catalysts containing carbide-forming transition metal promoters. *J. Catal.*, **255**, 104–113.
212. Lohitharn, N. and Goodwin, J.G. (2008) Effect of K promotion of Fe and FeMn Fischer–Tropsch synthesis catalysts: analysis at the site level using SSITKA. *J. Catal.*, **260**, 7–16.
213. Keller, G.E. and Bhasin, M.M. (1982) Synthesis of ethylene via oxidative coupling of methane: I. Determination of active catalysts. *J. Catal.*, **73**, 9–19.
214. Arakawa, H., Aresta, M., Armor, J.N. *et al.* (2001) Catalysis research of relevance to carbon management: progress, challenges, and opportunities. *Chem. Rev.*, **101**, 953–996.
215. Takanabe, K. and Iglesia, E. (2008) Rate and selectivity enhancements mediated by OH radicals in the oxidative coupling of methane catalyzed by Mn/Na₂WO₄/SiO₂. *Angew. Chem. Int. Ed.*, **47**, 7689–7693.
216. Takanabe, K. and Iglesia, E. (2009) Mechanistic aspects and reaction pathways for oxidative coupling of methane on Mn/Na₂WO₄/SiO₂ catalysts. *J. Phys. Chem. C*, **113**, 10131–10145.
217. Lunsford, J.H. (1995) The catalytic oxidative coupling of methane. *Angew. Chem. Int. Ed.*, **34**, 970–980.
218. Baidya, T., van Vegten, N., Jiang, Y. *et al.* (2011) Oxidative coupling of methane over Ca- and alkali metal-doped ThO₂. *Appl. Catal. A*, **391**, 205–214.
219. Baidya, T., van Vegten, N., Verel, R. *et al.* (2011) SrO·Al₂O₃ mixed oxides: a promising class of catalysts for oxidative coupling of methane. *J. Catal.*, **281**, 241–253.
220. Deboy, J.M. and Hicks, R.F. (1988) Kinetics of the oxidative coupling of methane over 1 wt% SrLa₂O₃. *J. Catal.*, **113**, 517–524.
221. Deboy, J.M. and Hicks, R.F. (1988) Oxidative coupling of methane over alkaline earth promoted La₂O₃. *J. Chem. Soc. Chem. Commun.*, **188**, 982–984.
222. Wang, L., Tao, L., Xie, M. *et al.* (1993) Dehydrogenation and aromatization of methane under non-oxidizing conditions. *Catal. Lett.*, **21**, 35–41.
223. Weckhuysen, B.M., Wang, D., Rosynek, M.P., and Lunsford, J.H. (1998) Conversion of methane to benzene over transition metal Ion ZSM-5 zeolites: II. Catalyst characterization by X-ray photoelectron spectroscopy. *J. Catal.*, **175**, 347–351.
224. Wang, D., Lunsford, J.H., and Rosynek, M.P. (1997) Characterization of a Mo/ZSM-5 catalyst for the conversion of methane to benzene. *J. Catal.*, **169**, 347–358.
225. Chu, N., Wang, J., Zhang, Y. *et al.* (2010) Nestlike hollow hierarchical MCM-22 microspheres: synthesis and exceptional catalytic properties. *Chem. Mater.*, **22**, 2757–2763.
226. Wang, D.Y., Kan, Q.B., Xu, N. *et al.* (2004) Study on methane aromatization over MoO₃/HMCM-49 catalyst. *Catal. Today*, **93–95**, 75–80.
227. Xu, Y., Bao, X., and Lin, L. (2003) Direct conversion of methane under nonoxidative conditions. *J. Catal.*, **216**, 386–395.
228. Su, L., Liu, L., Zhuang, J. *et al.* (2003) Creating mesopores in ZSM-5 zeolite by alkali treatment: a new way to enhance the catalytic performance of methane dehydroaromatization on Mo/HZSM-5 catalysts. *Catal. Lett.*, **91**, 155–167.
229. Jiang, H., Wang, L., Cui, W., and Xu, Y. (1999) Study on the induction period of methane aromatization over Mo/HZSM-5: partial reduction of Mo species and formation of carbonaceous deposit. *Catal. Lett.*, **57**, 95–102.
230. Maet, D. (2002) Carbonaceous deposition on Mo/HMCM-22 catalysts for methane aromatization: a TP technique investigation. *J. Catal.*, **208**, 260–269.

231. Ohnishi, R., Liu, S.T., Dong, Q. *et al.* (1999) Catalytic dehydrocondensation of methane with CO and CO₂ toward benzene and naphthalene on Mo/HZSM-5 and Fe/Co-modified Mo/HZSM-5. *J. Catal.*, **182**, 92–103.
232. Ma, S., Guo, X., Zhao, L. *et al.* (2013) Recent progress in methane dehydroaromatization: from laboratory curiosities to promising technology. *J. Energy Chem.*, **22**, 1–20.
233. Guo, X.G., Fang, G.Z., Li, G. *et al.* (2014) Direct, nonoxidative conversion of methane to ethylene, aromatics, and hydrogen. *Science*, **344**, 616–619.
234. Lyons, J.E., Ellis, P.E., and Durante, V.A. (1991) Active iron oxo centers for the selective catalytic oxidation of alkanes. *Stud. Surf. Sci. Catal.*, **67**, 99–116.
235. Michalkiewicz, B. (2004) Partial oxidation of methane to formaldehyde and methanol using molecular oxygen over Fe-ZSM-5. *Appl. Catal. A*, **277**, 147–153.
236. Otsuka, K. and Wang, Y. (2001) Direct conversion of methane into oxygenates. *Appl. Catal. A*, **222**, 145–161.
237. Periana, R.A., Taube, D.J., Evitt, E.R. *et al.* (1993) A mercury-catalyzed, high-yield system for the oxidation of methane to methanol. *Science*, **259**, 340–343.
238. Hammond, C., Forde, M.M., Ab Rahim, M.H. *et al.* (2012) Direct catalytic conversion of methane to methanol in an aqueous medium by using copper-promoted Fe-ZSM-5. *Angew. Chem.*, **124**, 5129–5133.
239. Dewitt, J.G., Bentsen, J.G., Rosenzweig, A.C. *et al.* (1991) X-ray absorption, moessbauer, and EPR studies of the dinuclear iron center in the hydroxylase component of methane monooxygenase. *J. Am. Chem. Soc.*, **113**, 9219–9235.
240. Huber, G.W., Iborra, S., and Corma, A. (2006) Synthesis of transportation fuels from biomass: chemistry, catalysts, and engineering. *Chem. Rev.*, **106**, 4044–4098.
241. Ragauskas, A.J., Williams, C.K., Davison, B.H. *et al.* (2006) The path forward for biofuels and biomaterials. *Science*, **311**, 484–489.
242. Cortright, R.D., Davda, R.R., and Dumesic, J.A. (2002) Hydrogen from catalytic reforming of biomass-derived hydrocarbons in liquid water. *Nature*, **418**, 964–967.
243. Huber, G.W., Cortright, R.D., and Dumesic, J.A. (2004) Renewable alkanes by aqueous-phase reforming of biomass-derived oxygenates. *Angew. Chem. Int. Ed.*, **43**, 1549–1551.
244. Soares, R.R., Simonetti, D.A., and Dumesic, J.A. (2006) Glycerol as a source for fuels and chemicals by low-temperature catalytic processing. *Angew. Chem. Int. Ed.*, **45**, 3982–3985.
245. Sharkov, V.I. (1963) Production of polyhydric alcohols from wood polysaccharides. *Angew. Chem.*, **2**, 405–409.
246. Fukuoka, A. and Dhepe, P.L. (2006) Catalytic conversion of cellulose into sugar alcohols. *Angew. Chem. Int. Ed.*, **45**, 5161–5163.
247. Yan, N., Zhao, C., Luo, C. *et al.* (2006) One-step conversion of cellobiose to C6-alcohols using a ruthenium nanocluster catalyst. *J. Am. Chem. Soc.*, **128**, 8714–8715.
248. Luo, C., Wang, S., and Liu, H. (2007) Cellulose conversion into polyols catalyzed by reversibly formed acids and supported ruthenium clusters in hot water. *Angew. Chem. Int. Ed.*, **46**, 7636–7639.
249. Ji, N., Zhang, T., Zheng, M. *et al.* (2008) Direct catalytic conversion of cellulose into ethylene glycol using nickel-promoted tungsten carbide catalysts. *Angew. Chem. Int. Ed.*, **44**, 8638–8641.
250. Ji, N., Zhang, T., Zheng, M. *et al.* (2009) Catalytic conversion of cellulose into ethylene glycol over supported carbide catalysts. *Catal. Today*, **147**, 77–85.
251. Zhang, Y., Wang, A., and Zhang, T. (2010) A new 3D mesoporous carbon replicated from commercial silica as a catalyst support for direct conversion of cellulose into ethylene glycol. *Chem. Commun.*, 862–864.
252. Zheng, M.Y., Wang, A.Q., Ji, N. *et al.* (2010) Transition metal–tungsten bimetallic catalysts for the conversion of cellulose into ethylene glycol. *ChemSusChem*, **3**, 63–66.

253. Wang, A. and Zhang, T. (2013) One-pot conversion of cellulose to ethylene glycol with multi-functional tungsten-based catalysts. *Acc. Chem. Res.*, **46**, 1377–1386.
254. Deng, T.Y., Sun, J.Y., and Liu, H. (2010) Cellulose conversion to polyols on supported Ru catalysts in aqueous basic solution. *Sci. China. Chem.*, **53**, 1476–1480.
255. Wang, X.C., Meng, L.Q., Wu, F. *et al.* (2012) Efficient conversion of microcrystalline cellulose to 1,2-alkanediols over supported Ni catalysts. *Green Chem.*, **14**, 758–765.
256. Wang, X.C., Wu, F., Yao, S.X. *et al.* (2012) Ni–Cu/ZnO-catalyzed hydrogenolysis of cellulose for the production of 1,2-alkanediols in hot compressed water. *Chem. Lett.*, **41**, 476–478.
257. Werpy, T. and Petersen, G.R. (2004) Top value added chemicals from biomass. Volume I. Results of screening for potential candidates from sugars and synthesis gas, U.S.D. Energy.
258. Bozell, J.J. and Petersen, G.R. (2010) Technology development for the production of biobased products from biorefinery carbohydrates—the US department of energy’s “Top 10” revisited. *Green Chem.*, **12**, 539–554.
259. Moreau, C., Durand, R., Razigade, S. *et al.* (1996) Dehydration of fructose to 5-hydroxymethylfurfural over H-mordenites. *Appl. Catal. A*, **145**, 211–224.
260. Binder, J.B. and Raines, R.T. (2009) Simple chemical transformation of lignocellulosic biomass into furans for fuels and chemicals. *J. Am. Chem. Soc.*, **131**, 1979–1985.
261. Zhao, H., Holladay, J.E., Brown, H., and Zhang, Z.C. (2007) Metal chlorides in ionic liquid solvents convert sugars to 5-hydroxymethylfurfural. *Science*, **316**, 1597–1600.
262. Pidko, E.A., Degirmenci, V., van Santen, R.A., and Hensen, E.J.M. (2010) Glucose activation by transient Cr^{2+} dimers. *Angew. Chem. Int. Ed.*, **49**, 2530–2534.
263. Lansalot-Matras, C. and Moreau, C. (2003) Dehydration of fructose into 5-hydroxymethylfurfural in the presence of ionic liquids. *Catal. Commun.*, **4**, 517–520.
264. Hu, S., Zhang, Z., Song, J. *et al.* (2009) Efficient conversion of glucose into 5-hydroxymethylfurfural catalyzed by a common Lewis acid SnCl_4 in an ionic liquid. *Green Chem.*, **11**, 1746–1749.
265. Qi, X., Watanabe, M., Aida, T.M., and Smith, R.L. (2010) Fast transformation of glucose and di-/polysaccharides into 5-hydroxymethylfurfural by microwave heating in an ionic liquid/catalyst system. *ChemSusChem*, **3**, 1071–1077.
266. Ilgen, F., Ott, D., Kralisch, D. *et al.* (2009) Conversion of carbohydrates into 5-hydroxymethylfurfural in highly concentrated low melting mixtures. *Green Chem.*, **11**, 1948–1954.
267. Cao, Q., Liang, W.Y., Guan, J. *et al.* (2014) Catalytic synthesis of 2,5-bis-methoxymethylfuran: a promising cetane number improver for diesel. *App. Catal. A*, **481**, 49–53.
268. Roman-Leshkov, Y., Barrett, C.J., Liu, Z.Y., and Dumesic, J.A. (2007) Production of dimethylfuran for liquid fuels from biomass-derived carbohydrates. *Nature*, **447**, 982–985.
269. Xia, Q.N., Cuan, Q., Liu, X.H. *et al.* (2014) Pd/NbOPO₄ multifunctional catalyst for the direct production of liquid alkanes from aldol adducts of furans. *Angew. Chem. Int. Ed.*, **53**, 9755–9760.
270. Koso, S., Furikado, I., Shima, A. *et al.* (2009) Chemoselective hydrogenolysis of tetrahydrofurfuryl alcohol to 1,5-pentanediol. *Chem. Commun.*, 2035–2037.
271. Yao, S.X., Wang, X.C., Jiang, Y.J. *et al.* (2014) One-step conversion of biomass-derived 5-hydroxymethylfurfural to 1,2,6-hexanetriol over Ni–Co–Al mixed oxide catalysts under mild conditions. *ACS Sustainable Chem. Eng.*, **2**, 173–180.
272. Hayes, D.J., Fitzpatrick, S., Hayes, M.H.B., and Ross, J.R.H. (2006) The biofine process—production of levulinic acid, furfural, and formic acid from lignocellulosic feedstocks, in *Biorefineries: Industrial Processes and Products: Status Quo and Future Directions*, vol. 1, International Union of Pure and Applied Chemistry, Durham, pp. 139–164.

273. Manzer, L.E. (2004) Catalytic synthesis of α -methylene- γ -valerolactone: a biomass-derived acrylic monomer. *Appl. Catal. A*, **272**, 249–256.
274. Lange, J.P., Price, R., Ayoub, P.M. *et al.* (2010) Valeric biofuels: a platform of cellulosic transportation fuels. *Angew. Chem. Int. Ed.*, **49**, 4479–4483.
275. Deng, L., Li, J., Lai, D.M. *et al.* (2009) Catalytic conversion of biomass-derived carbohydrates into γ -valerolactone without using an external H_2 supply. *Angew. Chem. Int. Ed.*, **48**, 6529–6532.
276. Horváth, I.T., Mehdi, H., Fábos, V. *et al.* (2008) γ -Valerolactone—a sustainable liquid for energy and carbon-based chemicals. *Green Chem.*, **10**, 238–242.
277. Elliott, D.C. and Frye, J.G. (1999) Oxopentanoic acid, catalytic hydrogenation and ring opening and withdrawal a hydrogenated product. US Patent 5,883,266.
278. Bond, J.Q., Alonso, D.M., Wang, D. *et al.* (2010) Integrated catalytic conversion of γ -valerolactone to liquid alkenes for transportation fuels. *Science*, **327**, 1110–1114.
279. Davda, R.R., Shabaker, J.W., Huber, G.W. *et al.* (2005) A review of catalytic issues and process conditions for renewable hydrogen and alkanes by aqueous-phase reforming of oxygenated hydrocarbons over supported metal catalysts. *Appl. Catal. B*, **56**, 171–186.
280. Davda, R.R., Shabaker, J.W., Huber, G.W. *et al.* (2003) Aqueous-phase reforming of ethylene glycol on silica-supported metal catalysts. *Appl. Catal. B*, **43**, 13–26.
281. Shabaker, J.W., Davda, R.R., Huber, G.W. *et al.* (2003) Aqueous-phase reforming of methanol and ethylene glycol over alumina-supported platinum catalysts. *J. Catal.*, **215**, 344–352.
282. Huber, G.W., Chheda, J.N., Barrett, C.J., and Dumesic, J.A. (2005) Production of liquid alkanes by aqueous-phase processing of biomass-derived carbohydrates. *Science*, **308**, 1446–1450.
283. West, R.M., Tucker, M.H., Braden, D.J., and Dumesic, J.A. (2009) Production of alkanes from biomass derived carbohydrates on bi-functional catalysts employing niobium-based supports. *Catal. Commun.*, **10**, 1743–1746.
284. Kunkes, E.L., Simonetti, D.A., West, R.M. *et al.* (2008) Catalytic conversion of biomass to monofunctional hydrocarbons and targeted liquid-fuel classes. *Science*, **322**, 417–421.
285. Fujishima, A. and Honda, K. (1972) Electrochemical photolysis of water at a semiconductor electrode. *Nature*, **238**, 37–38.
286. Hoffmann, M.R., Martin, S.T., Choi, W., and Bahnemann, D.W. (1995) Environmental applications of semiconductor photocatalysis. *Chem. Rev.*, **95**, 69–96.
287. Diebold, U. (2003) The surface science of titanium dioxide. *Surf. Sci. Rep.*, **48**, 53–229.
288. Zhang, H.Z. and Banfield, J.F. (2000) Understanding polymorphic phase transformation behavior during growth of nanocrystalline aggregates: insights from TiO_2 . *J. Phys. Chem. B*, **104**, 3481–3487.
289. Egerton, T.A., Kosa, S.A.M., and Christensen, P.A. (2006) Photoelectrocatalytic disinfection of *E. coli* suspensions by iron doped TiO_2 . *Phys. Chem. Chem. Phys.*, **8**, 398–406.
290. Park, J.H., Kim, S., and Bard, A.J. (2006) Novel carbon-doped TiO_2 nanotube arrays with high aspect ratios for efficient solar water splitting. *Nano Lett.*, **6**, 24–28.
291. Wang, W.-N., An, W.-J., Ramalingam, B. *et al.* (2012) Size and structure matter: enhanced CO_2 photoreduction efficiency by size-resolved ultrafine Pt nanoparticles on TiO_2 single crystals. *J. Am. Chem. Soc.*, **134**, 11276–11281.
292. Borgarello, E., Kiwi, J., Gratzel, M. *et al.* (1982) Visible light induced water cleavage in colloidal solutions of chromium-doped titanium dioxide particles. *J. Am. Chem. Soc.*, **104**, 2996–3002.
293. Zhu, J.F., Chen, F., Zhang, J.L. *et al.* (2006) Fe^{3+} - TiO_2 photocatalysts prepared by combining sol–gel method with hydrothermal treatment and their characterization. *J. Photochem. Photobiol. A*, **180**, 196–204.

294. Choi, W., Termin, A., and Hoffmann, M.R. (1994) The role of metal ion dopants in quantum-sized TiO_2 : correlation between photoreactivity and charge carrier recombination dynamics. *J. Phys. Chem.*, **98**, 13669–13679.
295. Choi, W., Termin, A., and Hoffmann, M.R. (1994) Effects of metal-ion dopants on the photocatalytic reactivity of quantum-sized TiO_2 particles. *Angew. Chem.*, **33**, 1091–1092.
296. Asahi, R., Morikawa, T., Irie, H., and Ohwaki, T. (2014) Nitrogen-doped titanium dioxide as visible-light-sensitive photocatalyst: designs, developments, and prospects. *Chem. Rev.*, **114**, 9824–9852.
297. Diwald, O., Thompson, T.L., Goralski, E.G. *et al.* (2004) Photochemical activity of nitrogen-doped rutile TiO_2 (110) in visible light. *J. Phys. Chem. B*, **108**, 6004–6008.
298. Irie, H., Watanabe, Y., and Hashimoto, K. (2003) Nitrogen-concentration dependence on photocatalytic activity of $\text{TiO}_{2-x}\text{N}_x$ powders. *J. Phys. Chem. B*, **107**, 5483–5486.
299. Chen, X., Wang, X., Hou, Y. *et al.* (2008) The effect of postnitridation annealing on the surface property and photocatalytic performance of N-doped TiO_2 under visible light irradiation. *J. Catal.*, **255**, 59–67.
300. Sakthivel, S. and Kisch, H. (2003) Daylight photocatalysis by carbon-modified titanium dioxide. *Angew. Chem. Int. Ed.*, **42**, 4908–4911.
301. Huang, D.G., Liao, S.J., Liu, J.M. *et al.* (2006) Preparation of visible-light responsive N–F-codoped TiO_2 photocatalyst by a sol–gel-solvothermal method. *J. Photochem. Photobiol. A*, **184**, 282–288.
302. Umabayashi, T., Yamaki, T., Itoh, H., and Asai, K. (2002) Band gap narrowing of titanium dioxide by sulfur doping. *Appl. Phys. Lett.*, **81**, 454–456.
303. Di Valentin, C. and Pacchioni, G. (2013) Trends in non-metal doping of anatase TiO_2 : B, C, N and F. *Catal. Today*, **206**, 12–18.
304. Sakthivel, S. and Kisch, H. (2001) Visible-light photocatalysis in nitrogen-doped titanium oxides. *Science*, **293**, 269–271.
305. Zhou, Z.Y., Tian, N., Li, J.T. *et al.* (2011) Nanomaterials of high surface energy with exceptional properties in catalysis and energy storage. *Chem. Soc. Rev.*, **40**, 4167–4185.
306. Zhang, Z.F., Deng, Z.B., Liang, C.J. *et al.* (2003) Organic light-emitting diodes with a nanostructured TiO_2 layer at the interface between ITO and NPB layers. *Displays*, **24**, 231–234.
307. Pan, J., Huhne, S.M., Shen, H. *et al.* (2011) SnO_2 – TiO_2 core–shell nanowire structures: investigations on solid state reactivity and photocatalytic behavior. *J. Phys. Chem. C*, **115**, 17265–17269.
308. Bai, H.W., Juay, J., Liu, Z.Y. *et al.* (2012) Hierarchical $\text{SrTiO}_3/\text{TiO}_2$ nanofibers heterostructures with high efficiency in photocatalytic H_2 generation. *Appl. Catal. B*, **125**, 367–374.
309. Liu, R., Yang, W.D., Qiang, L.S., and Liu, H.Y. (2012) Conveniently fabricated heterojunction ZnO/TiO_2 electrodes using TiO_2 nanotube arrays for dye-sensitized solar cells. *J. Power Sources*, **220**, 153–159.
310. Wang, C.H., Shao, C.L., Zhang, X.T., and Liu, Y.C. (2009) SnO_2 nanostructures– TiO_2 nanofibers heterostructures: controlled fabrication and high photocatalytic properties. *Inorg. Chem.*, **48**, 7261–7268.
311. Cao, T.P., Li, Y.J., Wang, C.H. *et al.* (2011) A facile in situ hydrothermal method to $\text{SrTiO}_3/\text{TiO}_2$ nanofiber heterostructures with high photocatalytic activity. *Langmuir*, **27**, 2946–2952.
312. Ni, M., Leung, M.K.H., Leung, D.Y.C., and Sumathy, K. (2007) A review and recent developments in photocatalytic water-splitting using TiO_2 for hydrogen production. *Renew. Sust. Energy Rev.*, **11**, 401–425.
313. Lee, S.G., Lee, S., and Lee, H.I. (2001) Photocatalytic production of hydrogen from aqueous solution containing CN^- as a hole scavenger. *Appl. Catal. A*, **207**, 173–181.

314. Galinska, A. and Walendziewski, J. (2005) Photocatalytic water splitting over Pt–TiO₂ in the presence of sacrificial reagents. *Energy Fuels*, **19**, 1143–1147.
315. Kim, G. and Choi, W. (2010) Charge-transfer surface complex of EDTA–TiO₂ and its effect on photocatalysis under visible light. *Appl. Catal. B*, **100**, 77–83.
316. Parrino, F., Augugliaro, V., Camera-Roda, G. *et al.* (2012) *J. Catal.*, **295**, 254.
317. Park, Y., Singh, N.J., Kim, K.S. *et al.* (2009) Fullerol–titania charge-transfer-mediated photocatalysis working under visible light. *Chem. Eur. J.*, **15**, 10843–10850.
318. Busca, G., Lietti, L., Ramis, G., and Berti, F. (1998) Chemical and mechanistic aspects of the selective catalytic reduction of NO_x by ammonia over oxide catalysts: a review. *Appl. Catal. B*, **18**, 1–36.
319. Pârâvulescu, V.I., Grange, P., and Delmon, B. (1998) Catalytic removal of NO. *Catal. Today*, **46**, 233–316.
320. Kato, A., Matsuda, S., Nakajima, F. *et al.* (1981) Reduction of nitric oxide with ammonia on iron oxide–titanium oxide catalyst. *J. Phys. Chem.*, **85**, 1710–1713.
321. Fabrizioli, P., Bürgi, T., and Baiker, A. (2002) Environmental catalysis on iron oxide–silica aerogels: selective oxidation of NH₃ and reduction of NO by NH₃. *J. Catal.*, **206**, 143–154.
322. Teng, H., Hsu, L.-Y., and Lai, Y.-C. (2001) Catalytic reduction of NO with NH₃ over carbons impregnated with Cu and Fe. *Environ. Sci. Technol.*, **35**, 2369–2374.
323. Marbán, G. and Fuentès, A.B. (2002) Kinetics of the low-temperature selective catalytic reduction of NO with NH₃ over activated carbon fiber composite-supported iron oxides. *Catal. Lett.*, **84**, 13–19.
324. Mou, X., Zhang, B., Li, Y. *et al.* (2012) Rod-shaped Fe₂O₃ as an efficient catalyst for the selective reduction of nitrogen oxide by ammonia. *Angew. Chem. Int. Ed.*, **51**, 2989–2993.
325. Ma, A.Z. and Grünert, W. (1999) Selective catalytic reduction of NO by ammonia over Fe-ZSM-5 catalysts. *Chem. Commun.*, 71–72.
326. Carja, G., Delahay, G., Signorile, C., and Coq, B. (2004) Fe-Ce-ZSM-5 a new catalyst of outstanding properties in the selective catalytic reduction of NO with NH₃. *Chem. Commun.*, 1404–1405.
327. Brandenberger, S., Kröcher, O., Tissler, A., and Althoff, R. (2010) The determination of the activities of different iron species in Fe-ZSM-5 for SCR of NO by NH₃. *Appl. Catal. B*, **95**, 348–357.
328. Forzatti, P., Nova, I., and Tronconi, E. (2009) Enhanced NH₃ selective catalytic reduction for NO_x abatement. *Angew. Chem.*, **121**, 8516–8518.
329. Iwamoto, M., Yahiro, H., Yu-u, Y. *et al.* (1990) Selective reduction of NO by lower hydrocarbons in the presence of O₂ and SO₂ over copper ion-exchanged zeolites. *Shokubai (Catalyst)*, **32**, 430–438.
330. Held, W., König, A., Richter, T. *et al.* (1990) Catalytic NO_x reduction in net oxidizing exhaust gas, *SAE Technical Paper Series*, 900496.
331. Ruetten, F., Sánchez, M., Sierraalta, A. *et al.* (2005) Application of computational methods to catalytic systems. *J. Mol. Catal. A*, **228**, 211–225.
332. Schay, Z., Guczi, L., Beck, A. *et al.* (2002) DeNO_x reactions on Cu-zeolites decomposition of NO, N₂O and SCR of NO by C₃H₈ and CH₄ on Cu-ZSM-5 and Cu-AITS-1 catalysts. *Catal. Today*, **75**, 393–399.
333. Sun, Q. and Sachtler, W.M.H. (2003) Mn/MFI catalyzed reduction of NO_x with alkanes. *Appl. Catal. B*, **42**, 393–401.
334. Kubacka, A., Janas, J., Wloch, E., and Sulikowski, B. (2005) Selective catalytic reduction of nitric oxide over zeolite catalysts in the presence of hydrocarbons and the excess of oxygen. *Catal. Today*, **101**, 139–145.

335. Shen, Q., Li, L., Hao, Z., and Xu, Z. (2008) Highly active and stable bimetallic Ir/Fe-USY catalysts for direct and NO-assisted N₂O decomposition. *Appl. Catal. B*, **84**, 734–741.
336. Chen, H.Y., Wang, X., and Sachtler, W.M.H. (2000) Reduction of NO_x over various Fe/zeolite catalyst. *Appl. Catal. A*, **194/195**, 159–168.
337. Iwamoto, M. and Hamada, H. (1999) Removal of nitrogen monoxide from exhaust gases through novel catalytic processes. *Catal. Today*, **10**, 57–61.
338. Lombardo, E.A., Sill, G.A., d'Itri, J.L., and Hall, W.K. (1998) The possible role of nitromethane in the SCR of NO_x with CH₄ over M-ZSM5 (M=Co, H, Fe, Cu). *J. Catal.*, **173**, 440–449.
339. Desai, A.J., Kovalchuk, V.I., Lombardo, E.A., and d'Itri, J.L. (1999) CoZSM-5: why this catalyst selectively reduces NO_x with methane. *J. Catal.*, **184**, 396–405.
340. Carniti, P., Gervasini, A., Modica, V.H., and Ravasio, N. (2000) Catalytic selective reduction of NO with ethylene over a series of copper catalysts on amorphous silicas. *Appl. Catal. B*, **28**, 175–185.
341. Liu, Z., Amiridis, M.D., and Chen, Y. (2005) Characterization of CuO supported on tetragonal ZrO₂ catalysts for N₂O decomposition to N₂. *J. Phys. Chem. B*, **109**, 1251–1255.
342. Bethke, K.A. and Kung, H.H. (1997) Supported Ag catalysts for the lean reduction of NO with C₃H₆. *J. Catal.*, **172**, 93–102.
343. Kameoka, S., Ukisu, Y., and Miyadera, T. (2000) Selective catalytic reduction of NO_x with CH₃OH, C₂H₅OH and C₃H₆ in the presence of O₂ over Ag/Al₂O₃ catalyst: role of surface nitrate species. *Phys. Chem. Chem. Phys.*, **2**, 367–372.
344. Thomas, C. (2015) On an additional promoting role of hydrogen in the H₂-assisted C₃H₆-SCR of NO_x on Ag/Al₂O₃: a lowering of the temperature of formation–decomposition of the organo-NO_x intermediates? *Appl. Catal. B*, **73**, 454–462.
345. Miyadera, T. (1993) Alumina-supported silver catalysts for the selective reduction of nitric oxide with propene and oxygen-containing organic compounds. *Appl. Catal. B*, **2**, 199–205.
346. Chansai, S., Burch, R., Hardacre, C. *et al.* (2014) Investigating the promotional effect of methanol on the low temperature SCR reaction on Ag/Al₂O₃. *Appl. Catal. B*, **160–161**, 356–364.
347. Shimizu, K. and Tsuzuki, M. (2007) Effects of hydrogen and oxygenated hydrocarbons on the activity and SO₂-tolerance of Ag/Al₂O₃ for selective reduction of NO. *Appl. Catal. B*, **71**, 80–84.
348. He, H. and Yu, Y. (2005) Selective catalytic reduction of NO_x over Ag/Al₂O₃ catalyst: from reaction mechanism to diesel engine test. *Catal. Today*, **100**, 37–47.
349. Roffael, E. (1993) *Formaldehyde Release from Particleboard and Other Wood Based Panel*, Forest Research Institute, Malaysia, Kuala Lumpur.
350. Mo, J., Zhang, Y., Xu, Q. *et al.* (2009) Photocatalytic purification of volatile organic compounds in indoor air: a literature review. *Atmos. Environ.*, **43**, 2229–2246.
351. Rong, H., Ryu, Z., Zheng, J., and Zhang, Y. (2003) Influence of heat treatment of rayon-based activated carbon fibers on the adsorption of formaldehyde. *J. Colloid Interface Sci.*, **261**, 207–212.
352. Spivey, J.J. (1987) Complete catalytic oxidation of volatile organics. *Ind. Eng. Chem. Res.*, **26**, 2165–2180.
353. Scirè, S., Minicò, S., Crisafulli, C., and Galvagno, S. (2001) Catalytic combustion of volatile organic compounds over group IB metal catalysts on Fe₂O₃. *Catal. Commun.*, **2**, 229–232.
354. Imamura, S., Uematsu, Y., Utani, K., and Ito, T. (1991) Combustion of formaldehyde on ruthenium/cerium(IV) oxide catalyst. *Ind. Eng. Chem. Res.*, **30**, 18–21.
355. Mao, C.-F. and Vannice, M.A. (1995) Formaldehyde oxidation over Ag catalysts. *J. Catal.*, **154**, 230–244.
356. Zhang, C., He, H., and Tanaka, K. (2006) Catalytic performance and mechanism of a Pt/TiO₂ catalyst for the oxidation of formaldehyde at room temperature. *Appl. Catal. B*, **65**, 37–43.

357. Zhang, C., Liu, F., Zhai, Y. *et al.* (2012) Alkali-metal-promoted Pt/TiO₂ opens a more efficient pathway to formaldehyde oxidation at ambient temperatures. *Angew. Chem. Int. Ed.*, **51**, 9628–9632.
358. Huang, Z., Gu, X., Cao, Q. *et al.* (2012) Catalytically active single-atom sites fabricated from silver particles. *Angew. Chem. Int. Ed.*, **51**, 4198–4203.
359. Foster, J. and Masel, R. (1986) Formaldehyde oxidation on nickel oxide. *Ind. Eng. Chem. Process Des. Dev.*, **25**, 563–568.
360. Sekine, Y. and Nishimura, A. (2001) Removal of formaldehyde from indoor air by passive type air-cleaning materials. *Atmos. Environ.*, **35**, 2001–2007.
361. Chen, H., He, J., Zhang, C., and He, H. (2007) Self-assembly of novel mesoporous manganese oxide nanostructures and their application in oxidative decomposition of formaldehyde. *J. Phys. Chem. C*, **111**, 18033–18038.
362. Imamura, S., Shono, M., Okamoto, N. *et al.* (1996) Effect of cerium on the mobility of oxygen on manganese oxides. *Appl. Catal. A*, **142**, 279–286.
363. Baruwati, B. and Varma, R.S. (2011) Synthesis of N-doped nano TiO₂ using guanidine nitrate: an excellent visible light photocatalyst. *J. Nanosci. Nanotechnol.*, **11**, 2036–2041.
364. Virkutyte, J. and Varma, R.S. (2012) Synthesis and visible light photoactivity of anatase Ag and garlic loaded TiO₂ nanocrystalline catalyst. *RSC Adv.*, **2**, 2399–2407.
365. Virkutyte, J., Varma, R.S., and Jegatheesan, V. (eds), Integrated Environmental Technology Series, (2010) *Treatment of Micropollutants in Water and Waste Water*, IWA Publishing, London, New York.
366. Xiao, Q., Zhang, J., Xiao, C. *et al.* (2008) Solar photocatalytic degradation of methylene blue in carbon-doped TiO₂ nanoparticles suspension. *Sol. Energy*, **82**, 706–713.
367. Zhu, Y.F. and Dan, Y. (2010) Photocatalytic activity of poly(3-hexylthiophene)/titanium dioxide composites for degrading methyl orange. *Sol. Energy Mater. Sol. Cells*, **94**, 1658–1664.
368. Balu, A.M., Baruwati, B., Serrano, E. *et al.* (2011) Magnetically separable nanocomposites with photocatalytic activity under visible light for the selective transformation of biomass-derived platform molecules. *Green Chem.*, **13**, 2750–2758.
369. Pelaez, M., Baruwati, B., Varma, R.S. *et al.* (2013) Microcystin-LR removal from aqueous solutions using a magnetically separable N-doped TiO₂ nanocomposite under visible light irradiation. *Chem. Commun.*, **49**, 10118–10120.
370. Wang, Y., Li, X., Wang, N. *et al.* (2008) Controllable synthesis of ZnO nanoflowers and their morphology-dependent photocatalytic activities. *Sep. Purif. Technol.*, **62**, 727–732.
371. Deng, D., Martin, S.T., and Ramanathan, S. (2010) Synthesis and characterization of one-dimensional flat ZnO nanotower arrays as high-efficiency adsorbents for the photocatalytic remediation of water pollutants. *Nanoscale*, **2**, 2685–2691.
372. Ullah, R. and Dutta, J. (2008) Photocatalytic degradation of organic dyes with manganese-doped ZnO nanoparticles. *J. Hazard. Mater.*, **156**, 194–200.
373. Wang, Q., Geng, B.Y., and Wang, S.Z. (2009) ZnO/Au hybrid nanoarchitectures: wet-chemical synthesis and structurally enhanced photocatalytic performance. *Environ. Sci. Technol.*, **43**, 8968–8973.
374. Sathish Kumar, P.S., Sivakumar, R., Anandan, S. *et al.* (2008) Photocatalytic degradation of acid red 88 using Au–TiO₂ nanoparticles in aqueous solutions. *Water Res.*, **42**, 4878–4884.
375. Alvaro, M., Carbonell, E., Ferrer, B.F. *et al.* (2007) Semiconductor behavior of a metal-organic framework (MOF). *Chem. Eur. J.*, **13**, 5106–5112.
376. Llabrèi Xamena, F.X., Calza, P., Lamberti, C. *et al.* (2003) Enhancement of the ETS-10 titanosilicate activity in the shape-selective photocatalytic degradation of large aromatic molecules by controlled defect production. *J. Am. Chem. Soc.*, **125**, 2264–2271.
377. Yu, Z.T., Liao, Z.L., Jiang, Y.S. *et al.* (2005) Water-insoluble Ag–U–organic assemblies with photocatalytic activity. *Chem. Eur. J.*, **11**, 2642–2650.